Technical Physics Letters, Vol. 30, No. 2, 2004, pp. 102–105. Translated from Pis'ma v Zhurnal Tekhnicheskoĭ Fiziki, Vol. 30, No. 3, 2004, pp. 39–46.

Applicability of the Classical Analysis of Experiments with Split Hopkins Pressure Bar

S. L. Lopatnikov, B. A. Gama, K. Krauthouser, and G. Gillespie, Jr.

Center for Composite Materials, University of Delaware, Newark, Delaware 19716, USA

Received April 10, 2003

Abstract—It is shown that a classical approach to the treatment of data for the split Hopkinson pressure bar (SHPB) is applicable only to magnetically soft materials, the acoustic impedance of which is small as compared to that of the measuring bars. Unjustified application of the classical method to materials with high acoustic impedance (such as ceramics) or with a high viscosity may lead to unacceptably large errors. A physically consistent theory for the treatment of SHPB data is proposed. © *2004 MAIK "Nauka/Interperiodica".*

We propose a critical analysis of applicability of a classical method of the treatment of data obtained using the split Hopkinson pressure bar (SHPB) (Fig. 1). This method, widely used for more than five decades for obtaining rheological data in the rage of loading rates from 100 to 10^4 s^{-1}, has become a standard rheological technique [1–9] and is applied to probing a large variety of materials.

The classical analysis of SHPB data and formulation of the problem. The classical theory (see, e.g., [8]) is developed for a sample pressed between two identical elastic bars. The effective strain ε_s in the sample can be expressed via displacements of the sample–bar interfaces (Fig. 2) as follows:

$$\bar{\varepsilon}_s = (U_T(t) - U_I(t))/H. \tag{1}$$

By virtue of the continuity of displacements at the boundaries, the interfacial displacements can be expressed in terms of deformations in the incident $\varepsilon_I(t, 0)$, reflected $\varepsilon_R(t, 0)$, and transmitted $\varepsilon_T(t, H)$ waves (reduced to the sample–bar interfaces),

$$\frac{dU_I}{dt} = -c(\varepsilon_I(t, 0) - \varepsilon_R(t, 0)),$$
$$\frac{dU_T}{dt} = -c\varepsilon_T(t, H), \tag{2}$$

which yields

$$\frac{d\bar{\varepsilon}(t)}{dt} = \frac{c}{H}(\varepsilon_I(t, 0) - \varepsilon_R(t, 0) - \varepsilon_T(t, H)). \tag{3}$$

Here, c is the velocity of sound in the bar material, H is the sample thickness, U_I is the incident bar displacement, and U_T is the transmitter bar displacement.

On the other hand, forces acting upon the sample can be represented as

$$F_I = AE(\varepsilon_I(t, 0) + \varepsilon_R(t, 0)),$$
$$F_T = AE\varepsilon_T(t, H). \tag{4}$$

In the classical approach, these forces are in equilibrium,

$$F_I = F_T, \tag{5}$$

for which expressions (4) yield

$$\varepsilon_I(t, 0) + \varepsilon_R(t, 0) - \varepsilon_T(t, H) = 0. \tag{6}$$

Using this relation to exclude $\varepsilon_T(t, H)$ from Eq. (3), we obtain

$$\frac{d\bar{\varepsilon}(t)}{dt} = -\frac{2c}{H}\varepsilon_R(t, 0). \tag{7}$$

The effective stress in a sample is defined as

$$\bar{\sigma} = \frac{F_I + F_T}{2A_s}$$
$$= \frac{AE}{2A_s}(\varepsilon_I(t, 0) + \varepsilon_R(t, 0) + \varepsilon_T(t, H)) = \frac{AE}{A_s}\varepsilon_T(t, H), \tag{8}$$

where A and A_s are the cross-sectional areas of the bar and the sample, respectively, and E is the known elastic modulus of the bar material. Equations (7) and (8) express the effective stress and strain in the sample via acoustical quantities, which can be measured in the

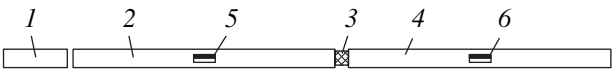

Fig. 1. Schematic diagram of the split Hopkinson pressure bar configuration: (*1*) striker; (*2*) incidence bar; (*3*) sample; (*4*) transmitter bar; (*5*, *6*) stress sensors.

1063-7850/04/3002-0102$26.00 © 2004 MAIK "Nauka/Interperiodica"

bars, and represent a mathematical model for the classical processing of SHPB data.

Despite apparently plausible reasoning, Eqs. (7) and (8) contain both mathematical and physical defects. In order to elucidate the nature of the problem, let us assume that equality (5) is approximate and there is a small deviation from equilibrium,

$$\Delta F = F_T - F_I. \tag{9}$$

Repeating the above considerations with allowance for the small (but finite) deviation from the equilibrium, we obtain

$$\bar{\sigma} = \frac{F_I + F_T}{2A_s} = \frac{AE}{A_s}\left(\varepsilon_T(t, H) - \frac{\Delta F(t)}{2AE}\right), \tag{10}$$

$$\frac{d\bar{\varepsilon}(t)}{dt} = -\frac{2c}{H}\left(\varepsilon_R(t, 0) + \frac{\Delta F(t)}{2AE}\right). \tag{11}$$

Here, Eq. (10) is equivalent to the classical equation (8), provided that we can neglect the term $\frac{\Delta F(t)}{2AE}$ in comparison to $\varepsilon_T(t, H)$. This condition was discussed by Kolsky [5], Gray [8], and Ravichandran and Subbash [10]. Equation (11) is equivalent to the classical equation (7) only provided the additional condition $|\varepsilon_{R(t, 0)}| \gg \left|\frac{\Delta F(t)}{2AE}\right|$. In this context, our aim is to evaluate $\frac{\Delta F(t)}{AE}$ and compare this quantity to $\varepsilon_R(t, 0)$.

One-dimensional model of elastic wave propagation in SHPB. For the sake of simplicity, let us consider the case of an arbitrary linear sample. Nevertheless, this case covers a broad spectrum of materials such as linear-elastic media, viscous materials, materials with regular and singular memory [11–17], and some others. Following the classical approach, let us consider a one-dimensional SHPB model. It is natural to use expansions of the fields with respect to harmonics in the sample and bars (we select the positive sign at the $i\omega t$ exponent).

The boundary conditions between the sample and bars can be written in the following form:

$$x = 0: \left\{\begin{array}{c} u_I(t, 0) + u_R(t, 0) = u_S(t, 0) \\ A(\sigma_I(t, 0) + \sigma_R(t, 0)) = A_S\sigma_S(t, 0) \end{array}\right\},$$
$$x = H: \left\{\begin{array}{c} u_S(t, H) = u_T(t, H) \\ A_S\sigma_S(t, H) = A\sigma_T(t, H) \end{array}\right\}. \tag{12}$$

After tedious but simple calculations, essentially repeating the analysis of wave propagation in a three-layer system (see, e.g., [17], where the opposite sign at the $(-i\omega t)$ exponent is used that leads to the opposite sign of the reflection coefficient), we obtain expressions for the average stress and strain in the sample,

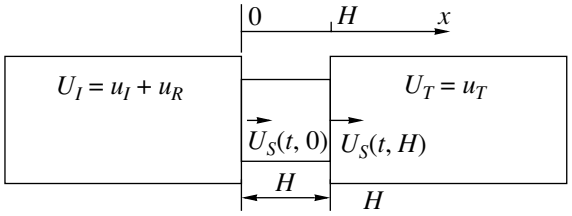

Fig. 2. Boundary conditions for a one-dimensional problem: U_I, displacement of the entrance bar–sample interface; u_I, particle displacement in the entrance wave at the entrance bar–sample interface; u_R, particle displacement in the reflected wave at the entrance bar–sample interface; U_T, displacement of the entrance sample–transmitter bar interface; u_T, particle displacement in the transmitted wave at the sample–transmitter bar interface.

$$\bar{\sigma}(\omega) = \frac{1}{2}\frac{A}{A_s} \times \frac{(1 - r^2) + (1 - r^2 f^-)e^{i\omega\tau_s} - r(f^- - 1)e^{i\omega\tau_s}}{(1 - r^2)}\sigma_T(\omega, H), \tag{13}$$

$$\bar{\varepsilon}(\omega) = -\frac{c}{H} \times \left(\frac{(1 - r^2)e^{-i\omega\tau_s} - r(f^- - 1) - 1 + r^2 f^-}{r(f^- - 1)}\right)\frac{\varepsilon_R(\omega, 0)}{i\omega}, \tag{14}$$

where

$$f^-(\omega) = e^{-2i\omega\tau_s}; \quad \tau_s = \frac{H}{c_s(\omega)}; \quad \tau = \frac{H}{c};$$
$$r(\omega) = \frac{A_s\rho_s c_s(\omega) - A\rho c}{A_s\rho_s c_s(\omega) + A\rho c}; \tag{15}$$

and $r(\omega)$ is the usual coefficient of reflection from the sample–bar interface. In the general case, the wave velocity can be a complex quantity.

Quasistatic approximation. The fronts of the propagating pulses of loading are usually smeared as a result of the geometric and/or physical wave dispersion in the bar material. As a result, the characteristic loading time is usually significantly greater than the time $\tau_s(\omega)$ of signal passage through the sample. Then, we may use only the low-frequency asymptotic behavior of expressions (13) and (14), which is referred to below as the quasistatic approximation.

Expanding $f^-(\omega)$ and $e^{\pm i\omega\tau_s}$ into series with respect to powers of $\omega\tau_s$, substituting these expansions into Eqs. (13) and (14), retaining only the first nonvanishing

terms, and returning to the time representation, we obtain

$$\bar{\sigma}(\omega) \approx \frac{A}{A_s}\sigma_T(\omega, H), \tag{16a}$$

$$\frac{d\bar{\varepsilon}(t)}{dt} \approx -\frac{2c}{H}(1 + \hat{K}_\varepsilon^{(0)})\varepsilon_R(t, 0), \tag{16b}$$

where

$$\hat{K}_\varepsilon^{(0)} \equiv -\mathbf{F}^{-1}\left(1 + \frac{(1 - r(\omega))^2}{4r(\omega)}\right)$$
$$= -\mathbf{F}^{-1}\left(1 + \frac{1}{\gamma^2(\omega) - 1}\right) = -\mathbf{F}^{-1}\left(\frac{\gamma^2(\omega)}{\gamma^2(\omega) - 1}\right). \tag{17}$$

$\mathbf{F}^{-1}$ is the inverse Fourier transform, and $\gamma(\omega) \equiv \frac{A_s\rho_s c_s(\omega)}{A\rho c}$ is the ratio of total impedances of the sample and bars. Note that, in the particular case of a linear-elastic sample, the operator $\hat{K}_\varepsilon^{(0)}$ represents a simple multiplication by a factor (because γ is independent of the frequency) and the kernel of $\hat{K}_\varepsilon^{(0)}$ is the Dirac delta function.

Equation (16a) for the average stress is fully equivalent to the corresponding classical equation (8), but Eq. (16b) for the average stress significantly differs from Eq. (7) by containing an additional operator factor $1 + \hat{K}_\varepsilon^{(0)}$. Evidently, the classical equation (7) for the effective strain is valid only when the operator $\hat{K}_\varepsilon^{(0)}$ is small and, hence (according to Eq. (17)), the sample impedance is small as compared to that of the measuring bars.

As can be readily checked, Eq. (9) can be represented in the quasistatic approximation as

$$\varepsilon_I(t, 0) + \varepsilon_R(t, 0) - \varepsilon_T(t, H) = \hat{K}_\varepsilon^{(0)}\varepsilon_R(t, 0). \tag{18}$$

A comparison of Eqs. (18) and (6) completely elucidates the nature of the mathematical error in the classical approach to analysis of the SHPB data, which is described in many handbooks and papers. The classical approach neglects the term $\hat{K}_\varepsilon^{(0)}\varepsilon_R(t, 0)$, which, in the general case, is on the same order of magnitude as the retained term $\varepsilon_R(t, 0)$. In fact, in assuming that the force balance has the form of Eq. (5), we have to assume to within the same accuracy that $\varepsilon_R(t, 0) = 0$! in Eq. (6). This condition has an absolutely clear physical meaning: a body in the state of perfect equilibrium cannot produce work; in particular, it cannot generate a reflected signal.

Comparison to the classical description of a linear-elastic sample. Considering the particular case of a linear-elastic sample, we can define the effective elastic modulus of this material as follows:

$$E_s = \frac{\bar{\sigma}}{\bar{\varepsilon}} = -(1 - \gamma^2)\frac{A}{A_s}E\frac{\varepsilon_T(t, H)}{\frac{2c}{H}\int_0^t \varepsilon_R(t, 0)dt}$$
$$= (1 - \gamma^2)E_s^{(cl)}, \tag{19}$$

where

$$E_s^{(cl)} = -\frac{A}{A_s}E\frac{\varepsilon_T(t, H)}{\frac{2c}{H}\int_0^t \varepsilon_R(t, 0)dt} \tag{20}$$

is the effective modulus defined in terms of the classical expressions (7) and (8). Let us consider the case of steel bars ($c \sim 5.13$ km/s, $\rho \sim 7.85$ g/cm^3) and a ceramic sample ($c \sim 9.74$ km/s, $\rho \sim 3.90$ g/cm^3) with equal diameters. In this case, $\gamma = \rho_s c_s/(\rho c) = 1.061$ and the effective strain in the sample is $\bar{\varepsilon} = 8.98\bar{\varepsilon}_{cl}$—that is, almost nine (!) times the value of $\bar{\varepsilon}_{cl}$ predicted by the classical theory. Accordingly, the effective elastic modulus calculated using the classical approach is about nine times the value calculated using the method proposed in this paper. Formally speaking, it is possible to reduce the sample impedance by using samples of sufficiently small size. However, this possibility is significantly restricted by the appearance of parasitic reflections from unloaded parts of the bars: in practice, the area of the sample cross section cannot be smaller than 0.6–0.7 of that of the bar cross section. A detailed consideration of this circumstance can be found in [8], while a theoretical analysis of deviations from the one-dimensional model is given in [18].

In principle, formula (20) readily provides convincing evidence that the classical theory leads in some cases to physically meaningless results. For example, formula (20) predicts an infinite modulus for a sample made of the same material (and diameter) as that of bars, in which case $\varepsilon_T(t, H) \neq 0$ and $\varepsilon_R(t, H) \equiv 0$. Moreover, a negative modulus is predicted for the samples possessing a greater acoustic stiffness than that of bars (in this case, the incident compression pulse is $\varepsilon_T(t, H) < 0$ and, hence, $\int_0^t \varepsilon_R(t, H)dt < 0$). Note that the proposed expression (19) predicts correct signs in all cases because the factor $1 - \gamma^2$ changes sign for stiff samples and is uncertain (0/0) for $\gamma = 1$. In the latter case, this uncertainty can be readily removed using the L'Hospital rule to yield a correct result $E_s = E$ in the limit of $\gamma \longrightarrow 1$ and $\rho_s = \rho$. This can be readily seen from Eq. (21) below, in which $\varepsilon_R(\omega, 0) \longrightarrow 0$ and $\zeta(\omega)$ tends to infinity.

SHPB data treatment in the general case. The rheological equation for linear materials, in the general

case, has the form of $\bar{\sigma}(t) = \hat{E}_s\bar{\varepsilon}(t)$, where $\hat{E}_s$ is a certain linear (integro-differential) operator. In the frequency representation, this operator can be written as $\hat{E}(\omega) = \dfrac{\bar{\sigma}(\omega)}{\bar{\varepsilon}(\omega)}$. Using Eq. (19) and taking into account that $\gamma(\omega) = \dfrac{\sqrt{\rho_s E_s(\omega)}}{\sqrt{\rho E}}$, we obtain an operator modulus of the medium in the time representation

$$\hat{E}_s = -\mathbf{F}^{-1}\left(\frac{i\omega\tau\dfrac{A}{2A_s}\zeta(\omega)}{\left(1 - i\omega\tau\dfrac{A}{2A_s}\dfrac{\rho_s}{\rho E}\zeta(\omega)\right)}\right),\quad \zeta(\omega) = \frac{\sigma_T(\omega, H)}{\varepsilon_R(\omega, 0)}. \tag{21}$$

Since the Fourier spectra of the measured quantities $\sigma_T(\omega, H)$ and $\varepsilon_R(\omega, 0)$ are limited in the frequency region, the value of $\zeta(\omega)$ is poorly defined in the high-frequency range and, hence, some regularization procedures have to be used in practice.

Conclusions. We have demonstrated that the classical SHPB method has significant defects and can be used only for studying the rheological properties of materials with an acoustic impedance significantly lower as compared to that of the measuring bars. A universal procedure of SHPB data processing has been proposed.

REFERENCES

1. R. M. Davies, Philos. Trans. R. Soc. London, Ser. A **240**, 375 (1948).
2. H. Kolsky, Proc. Phys. Soc. London **62**, 676 (1949).
3. J. Harding, E. D. Wood, and J. D. Campbell, J. Mech. Eng. Sci. **2**, 88 (1960).
4. U. S. Lindholm and L. M. Yeakley, Exp. Mech. **8**, 1 (1968).
5. Sia Nemat-Nasser, J. B. Issacs, and J. E. Starrett, Proc. R. Soc. London, Ser. A **453**, 371 (1991).
6. M. A. Meyers, *Dynamic Behavior of Materials* (Wiley, New York, 1994), pp. 54–59, 81–82, 305–310.
7. A. M. Bragov and A. K. Lumonov, Int. J. Impact Eng. **16**, 321 (1995).
8. G. T. Gray III, in *ASM Handbook* (ASM International, Materials Park, Ohio, 2000), Vol. 8, pp. 462–476.
9. C. Albertini and M. Montagnani, J. Phys. (France) **4**, C8-113 (1994).
10. G. Ravichandran and G. Subhash, J. Am. Ceram. Soc. **77**, 263 (1994).
11. M. Fabrizio and A. Moro, *Mathematical Problems in Linear Viscoelasticity* (SIAM, Philadelphia, 1992).
12. A. Hanyga, Math. Comp. Model. **34**, 1399 (2001).
13. M. Giona, S. Gerbelly, and H. E. Roman, Physica A **191**, 449 (1992).
14. S. Lopatnikov and B. Gurevich, Dokl. Akad. Nauk SSSR **281** (2), 47 (1985).
15. A. Hanyga and V. Rock, J. Acoust. Soc. Am. **107**, 2965 (2000).
16. B. Gurevich and S. Lopatnikov, Geophys. J. Int. **121**, 933 (1995).
17. L. M. Brekhovskikh, *Waves in Layered Media* (Nauka, Moscow, 1973; Academic, New York, 1980); L. M. Brekhovskikh, *Acoustics of Layered Media I: Plane and Quasi-Plane Waves* (Springer-Verlag, New York, 1998).
18. A. M. Samsonov, *Strain Solitons in Solids and How to Construct Them* (Chapman and Hall, London, 2001).

Translated by P. Pozdeev

Technical Physics Letters, Vol. 30, No. 2, 2004, pp. 106–108. Translated from Pis'ma v Zhurnal Tekhnicheskoĭ Fiziki, Vol. 30, No. 3, 2004, pp. 47–53.

The Role of Diffusion Current in the Formation of Spherical Striations

O. A. Nerushev, S. A. Novopashin*, V. V. Radchenko, and S. Z. Sakhapov

Institute of Thermal Physics, Siberian Division, Russian Academy of Sciences, Novosibirsk, Russia

** e-mail: sanov@itp.nsc.ru*

Received May 28, 2003; in final form, August 26, 2003

Abstract—We have experimentally studied spherical dc discharges with opposite polarities of the applied voltage. Under otherwise identical conditions, the phenomenon of spherical stratification takes place only when the central electrode is the anode (positive discharge). An analysis of the experimental data shows that the diffusion current component plays a decisive role in the formation of striations in a spherical glow discharge. © *2004 MAIK "Nauka/Interperiodica".*

The phenomenon of stratification of the positive column in a dc gas discharge tube is well known and exhaustively described [1–4]. Recently [5, 6], we experimentally observed stratification in a dc gas discharge of spherical geometry. Now, this effect is under extensive experimental and theoretical investigation [7–11].

The difference in geometry between a spherical discharge and that in a tube leads to a number of differences in characteristics of the discharge plasma, the foremost of which are as follows.

(i) The current density in the linear case is constant along the field line, whereas, in a spherical discharge, the current density increases in the direction toward the central electrode.

(ii) Recombination processes in a discharge tube proceed mostly on the walls, whereas, in the spherical case, the recombination can take place only in the discharge volume.

(iii) The radial inhomogeneity of a spherical discharge makes the total current dependent both on the drift of electrons in the electric field and on their diffusion.

(iv) The problem of describing a spherical discharge is strictly one-dimensional, in contrast to the discharge in a tube, where the flux of charged particles to the wall has to be taken into account.

For any polarity of a nonstratified spherical discharge, the electron density increases with decreasing radius. This implies that the diffusion motion is always directed outward from the center. For the positive polarity of the central electrode (positive discharge), the drift of electrons under the action of electric field is directed toward the center and, hence, is opposite to the diffusion direction. In the negative discharge, the directions of drift and diffusion coincide. Conservation of the total current in a stationary case implies the balance of diffusion and drift currents,

$$n\mu E - D\frac{dn}{dr} = \frac{J}{4\pi e r^2}, \qquad (1)$$

where e, n, μ, and D are the electron charge, density, mobility, and diffusion coefficient, respectively; E is the electric field strength; J is the total current; and r is the radius.

This study was aimed at determining the role of the diffusion current component in the formation of spherical striations. To this end, we have experimentally studied spherical discharges of both polarities in a wide range of discharge currents.

Experimental. The experiments were performed in a steel cylindrical vacuum chamber with a height of 60 cm and a diameter of 50 cm. One electrode was situated at the geometric center of the chamber, while grounded chamber walls acted as of the second electrode. The central electrode lead was introduced into the chamber via a quartz tube that served as an insulator, so that only a small end part of this lead remained uninsulated and carried a spherical electrode with a radius of 0.25–2.5 cm. The discharge was powered from a 400-μF capacitor charged up to a voltage of 1–2 kV (positive or negative relative to the ground). As the capacitor was discharged (via a 12-kΩ ballast), the voltage between electrodes decreased and the discharge current dropped. The current–voltage characteristics were obtained by simultaneously measuring the current in the circuit and the interelectrode voltage. We also monitored the optical emission from discharge and determined the range of currents for which the stratification took place. Prior to experiment, the chamber was evacuated to a residual pressure of 0.1 Pa and then filled with a working gas mixture. The experimental data pre-

sented below were obtained for a mixture of nitrogen with acetone vapor (50%) at a total pressure of 14.5 Pa.

Results and discussion. Figures 1a and 1b show the patterns of current and voltage variation with time in the discharges of positive and negative polarities of the central electrode, respectively. Figure 2 shows the current–voltage characteristics. Video monitoring of the luminescence from discharge showed that stratification takes place only for positive polarity of the central electrode. At a total current of 0.02 A, there appeared four striations with a maximum diameter of about 10 cm (Fig. 3). For the positive discharge, the size of the central electrode significantly influenced neither electrical characteristics of the discharge nor manifestations of the stratification phenomenon. The current–voltage characteristic of the positive discharge corresponds to that of a normal glow discharge, whereby the voltage remains almost unchanged when the current is varied within broad limits.

In the negative discharge, whereby the central electrode is the cathode, the entire range of currents (corresponding to the conditions of stratification in the positive discharge) could be covered only with a central electrode with a radius of 2.5 cm: the smaller cathode could not maintain the currents comparable to those developed with the central anode. The current–voltage characteristic of the negative discharge corresponds to that of an anomalous glow discharge that is related to a relatively small cathode area. Thus, the most important result is that, in the range of currents from 0.002 to 0.05 A, the formation of striations is observed only for the positive discharge.

Let us evaluate contributions of the diffusion and drift currents to the total charge transfer using the current–voltage characteristics. Assuming that the diffusion current component is small and neglecting the corresponding term in Eq. (1), we obtain an expression for the electron density as a function of the distance:

$$n = \frac{J}{\mu E \pi e r^2}. \quad (2)$$

Assuming also that the electric field outside the cathode layer is constant, we evaluate the diffusion current as

$$eD\frac{dn}{dr} = D\frac{2J}{\mu E 4\pi r^3}. \quad (3)$$

This yields the ratio of the absolute values of the diffusion and drift currents

$$\left|\frac{J_{\text{diff}}}{J_{\text{dr}}}\right| = \frac{2D}{r\mu E}. \quad (4)$$

Using the Einstein formula relating the mobility and diffusion coefficient, we eventually obtain

$$\left|\frac{J_{\text{diff}}}{J_{\text{dr}}}\right| = \frac{2kT}{erE}. \quad (5)$$

The reduced electric field in the positive column of glow discharge in a tube obeys the relation $E/p \sim 4$ V/(cm Torr) [4]. Assuming that this relation is valid in the spherical discharge under consideration, we obtain an estimate of $E \sim 0.4$ V/cm for the electric field strength at a working pressure used in our experiments. According to formula (5), for a characteristic electron temperature of ~1 eV, the drift and diffusion currents become close at a distance of $r \sim 5$ cm.

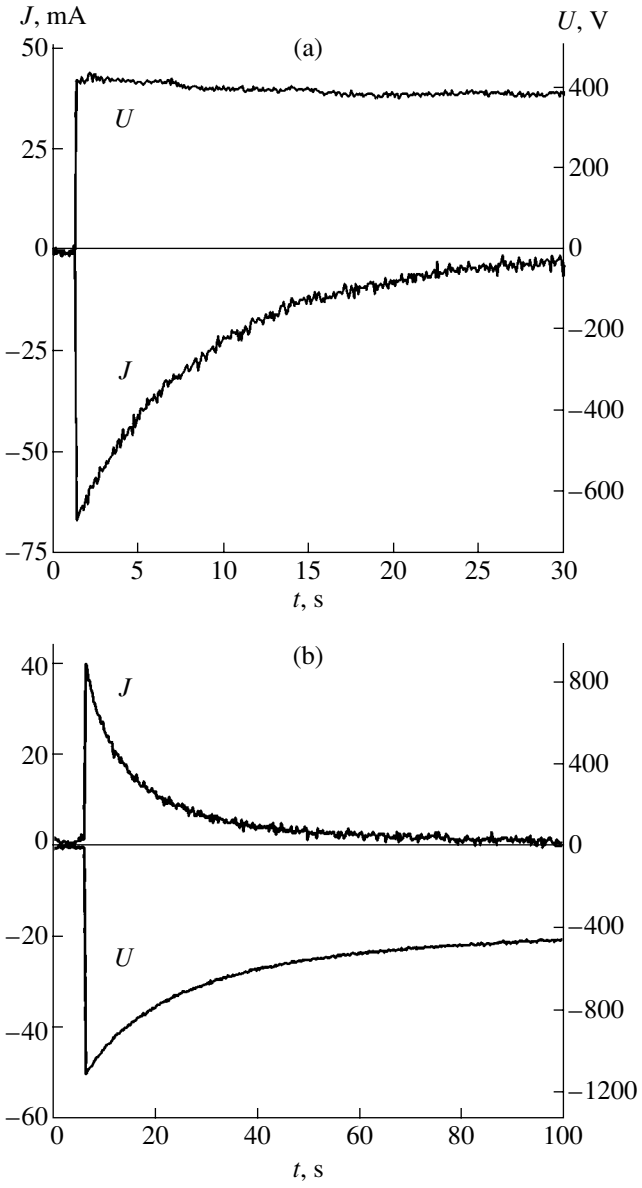

Fig. 1. Time variation of the current J and voltage U in a spherical discharge for (a) positive and (b) negative polarity of the central electrode.

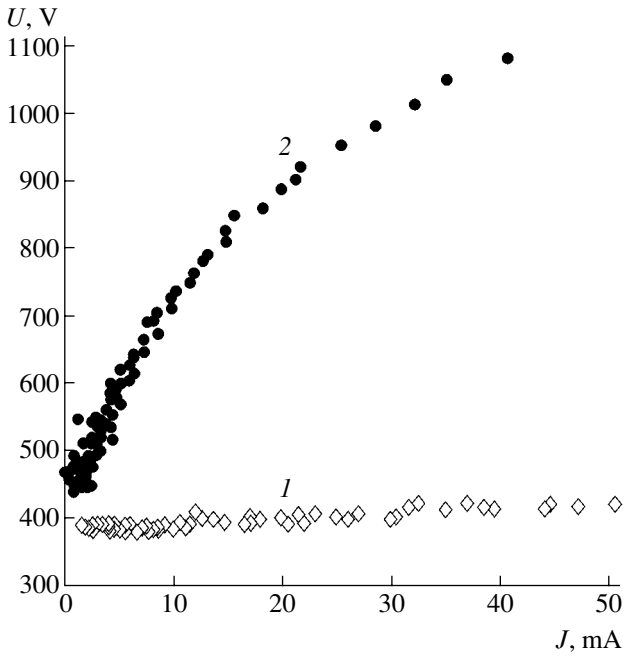

Fig. 2. The current–voltage characteristics of a spherical discharge measured for (*1*) positive and (*2*) negative polarity of the central electrode.

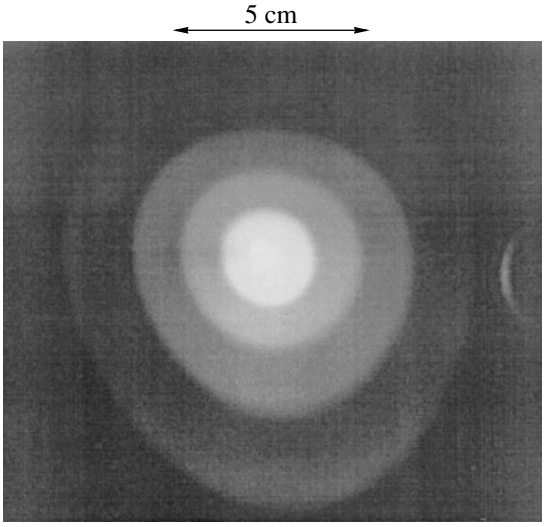

Fig. 3. Photograph of a stratified spherical gas discharge 15 s after initiation (top arrow indicates the spatial scale).

Since the diffusion and drift current components are added in the negative discharge and subtracted in the positive discharge, the latter case implies a higher electron density at the same total current. It can be also noted that the presence of opposite current components may lead to instability of the discharge, because each of the two electron fluxes may significantly vary while the total current remains constant. Based on the above qualitative analysis of the experimental results, we may conclude that the diffusion current component plays a decisive role in the formation of striations in a spherical discharge.

In conclusion, note that a strict analysis of the stability of positive and negative discharges presents a rather difficult task. Indeed, such an analysis must take into account a large number of factors, including the real dependence of the electron mobility on the reduced electric field, the balance of charged particles, the Poisson equation, the ion current, the formation of negative ions and metastable particles, and the plasmachemical reactions. Moreover, the diffusion–drift approximation used above may become insufficient for such a strict analysis that would require using a kinetic approach.

Acknowledgments. This study was supported by the International Science and Technology Center within the framework of the "Spherical Ionization Waves" project (grant no. 1425).

REFERENCES

1. L. Pekarek, Usp. Fiz. Nauk **94**, 463 (1968) [Sov. Phys. Usp. **11**, 188 (1968)].
2. A. V. Nedospasov, Usp. Fiz. Nauk **94**, 439 (1968) [Sov. Phys. Usp. **11**, 174 (1968)].
3. P. S. Landa, N. A. Miskinova, and Yu. V. Ponomarev, Usp. Fiz. Nauk **132**, 601 (1980) [Sov. Phys. Usp. **23**, 813 (1980)].
4. Yu. P. Raĭzer, *The Physics of Gas Discharge* (Nauka, Moscow, 1987).
5. O. A. Nerushev, S. A. Novopashin, V. V. Radchenko, *et al.*, Pis'ma Zh. Éksp. Teor. Fiz. **66**, 679 (1997) [JETP Lett. **66**, 711 (1997)].
6. O. A. Nerushev, S. A. Novopashin, G. I. Sukhinin, *et al.*, Phys. Rev. E: Stat. Phys., Plasmas, Fluids, Relat. Interdiscip. Top. **58**, 4897 (1998).
7. L. Conde and L. Leon, IEEE Trans. Plasma Sci. **27**, 80 (1999).
8. L. Conde, L. F. Ibanez, and C. Ferro-Fontan, Phys. Rev. E: Stat. Phys., Plasmas, Fluids, Relat. Interdiscip. Top. **64**, 046402 (2001).
9. F. Sigeneger, G. I. Sukhinin, and R. Winkler, Plasma Chem. Plasma Process. **20**, 87 (2000).
10. Y. Hoshi, H. Yoshida, and Y. Tsutsui, J. Appl. Phys. **92**, 5668 (2002).
11. O. A. Nerushev, S. A. Novopashin, V. V. Radchenko, and G. I. Sukhinin, Fiz. Plazmy **26**, 81 (2000) [Plasma Phys. Rep. **26**, 78 (2000)].

Translated by P. Pozdeev

Technical Physics Letters, Vol. 30, No. 2, 2004, pp. 109–112. Translated from Pis'ma v Zhurnal Tekhnicheskoĭ Fiziki, Vol. 30, No. 3, 2004, pp. 54–61.

A Model of Discontinuous Precipitation Based on the Balance and Maximum Production of the Entropy

Yu. A. Lyashenko

Cherkassy National University, Cherkassy, Ukraine

e-mail: urico@cdu.edu.ua

Revised manuscript received August 26, 2003

Abstract—A model of discontinuous precipitation in supercooled binary polycrystalline alloys at reduced temperatures, taking place as a result of the diffusion-induced grain boundary migration, is constructed with allowance of grain boundary diffusion. The proposed approach allows independent determination of the main parameters, including the interlamellar distance, the maximum velocity of the phase transformation front, and the concentration jump at this boundary. This is achieved by using a set of equations for the (i) mass transfer in the moving interphase boundary, (ii) balance of the entropy fluxes at the phase transformation front, and (iii) maximum rate of the free energy release. The model uses a minimum of thermodynamic information on the two-phase system: the curvature of the Gibbs potential surface in the decomposing phase and the free energy of the interface between the new phases. Theoretical results are compared to the available experimental data. © *2004 MAIK "Nauka/Interperiodica".*

Many problems in materials science are related to choosing a pathway in the diffusion evolution of a nonequilibrium metal system exhibiting phase transformations under uncertain conditions, whereby various regimes are possible for the same initial and boundary conditions. One such problem, involving an invariant in the form of a product of the squared period of the growing structure and the growth rate, is how to provide for a discontinuous precipitation of a binary alloy with a given composition, which is supersaturated as a result of supercooling [1, 2]. In contrast to a spinodal decomposition that takes place homogeneously in the whole volume and is controlled by changes in the elastic energy [3, 4], the transformation region represents a moving large-angle incoherent grain and phase boundary.

Figure 1 shows the configuration of a model system representing a binary alloy α_0 decomposing with the formation of a single cell of the depleted phase α in equilibrium with phase β. The transformation region R moving at a constant velocity v toward the decomposing phase α_0 coincides with the boundary between α_0 and α phases and has the height b, width h, and length Δz. Let $c^{\alpha/\beta}$ denote the equilibrium concentration at the α–β interface in the α phase; c^{β}, the equilibrium concentration in the β phase lamella; and $c_1^{\max}$, the maximum concentration in the α phase (at the center of the α phase lamella along the x axis).

The thermodynamic stimulus of the discontinuous precipitation, as well as of any other process at a constant temperature and pressure, is a decrease in the Gibbs potential. This is illustrated by a model phase diagram in Fig. 2. The dominating factor is the change in the chemical energy, while the role of elastic energy is insignificant. The motion of the transformation front partially decreases the degree of nonequilibrium in the system by reducing the concentration in the α phase cell and by inducing the β phase separation with the α–β interface formation. Attaining perfect equilibrium behind the transformation front corresponds to the formation of α phase cells with the $c^{\alpha/\beta}$ concentration which is principally possible in the case of a strongly retarded phase boundary.

At low temperatures, the rate of discontinuous precipitation is controlled by the diffusion of components in the flat grain boundary moving at a constant velocity v (for the frozen bulk diffusion) [1, 5]. The dependence

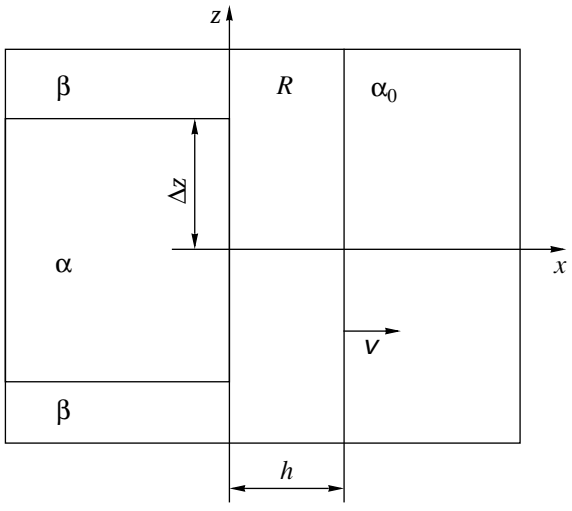

Fig. 1. Model system configuration in the x–z plane.

1063-7850/04/3002-0109$26.00 © 2004 MAIK "Nauka/Interperiodica"

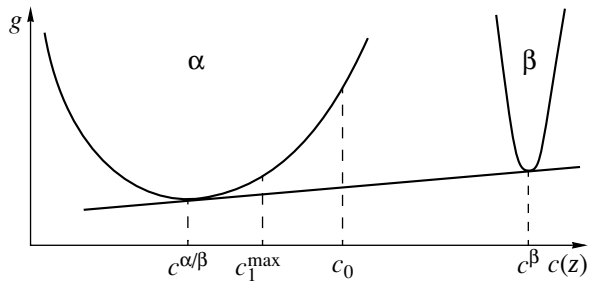

Fig. 2. A model phase diagram and the phase equilibria.

of concentration in the α phase on the coordinate z along the transformation boundary is described by a quasi-stationary grain boundary diffusion equation for a moving boundary [5] based on the balance of component fluxes (without specification of the mechanism of atomic jumps):

$$s\tilde{D}\frac{d^2c(z)}{dz^2} + \frac{c_0 - c(z)}{h}v = 0. \qquad (1)$$

Here, s is the segregation coefficient, $\tilde{D}$ is the coefficient of mutual diffusion in the phase boundary R, $c(z)$ is the local concentration in the boundary R, and h is the boundary width. The Cahn solution to this equation is as follows:

$$c(z) = c_0 - (c_0 - c^{\alpha/\beta})\frac{\cosh(z/L)}{\cosh(\Delta z/L)}, \qquad (2)$$

where the coordinate z varies from zero (in the middle of the α phase lamella) to Δz at the α–β interface. Accordingly, $c(z)$ changes from $c_1^{\max}$ to $c^{\alpha/\beta}$ over a half length of the cell, depending on the combination of parameters $\Delta z/L$. The interlamellar distance Δz, the kinetic coefficient $L = \sqrt{s\tilde{D}h/v}$, and the triple product $s\tilde{D}h$ are related as

$$sh\tilde{D} = \frac{1}{C}\Delta z^2 v, \qquad (3)$$

where C is the Cahn parameter determined from the relation

$$\frac{c_0 - c_1}{c_0 - c^{\alpha/\beta}} = \frac{2}{\sqrt{C}}\tanh\left(\frac{\sqrt{C}}{2}\right),$$

and c_1 is the average concentration in the α phase.

Each kinetically possible solution for an arbitrary transformation rate and the corresponding value of the parameter L gives a certain interlamellar distance Δz. For $\Delta z/L \longrightarrow 0$, the maximum concentration $c_1^{\max}$ in the α phase (at the center of the α phase lamella and along the lamella) tends to the equilibrium value $c^{\alpha/\beta}$. As the $\Delta z/L$ ratio increases, the degree of redistribution of the components decreases, the interphase boundary velocity increases, and the system remains substantially nonequilibrium. Thus, a single equation (1) with the solution (2) cannot unambiguously describe the kinetics of the discontinuous precipitation and do not provide for the independent determination of Δz and L. In order to eliminate this uncertainty, Cahn [5] employed the principle of maximum decrease in the free energy ΔF during the discontinuous precipitation reaction. This was achieved by considering a linear relationship between ΔF and the boundary velocity and by introducing the second kinetic coefficient representing the boundary mobility [5]. However, this linear relationship is not always confirmed in experiment [6].

The main idea of the approach developed in this study consists in a more thorough analysis of the balance of energy release and degradation in the transformation boundary moving at a constant velocity. In contrast to the Cahn model, it is suggested that the total decrease in the free energy has to be balanced with all ways of the energy degradation: both via diffusion along the transformation region and via interphase (α_0–α) jumps of atoms (with the jumping kinetics determining mobility of the phase boundary). For independently determining the main kinetic parameters, we will use the principle of maximum rate of the free energy release [7], the equation of balance of the entropy fluxes, and the Cahn solution (2) of the mass transfer equation. The analysis will be performed for a diffusion-controlled discontinuous precipitation reaction under the assumption of a readily moving (high-mobility) interphase boundary.

Let us assume that a change in the entropy d_eS during the elementary time interval dt as a result of the phase transformation in the region R (coinciding with the interphase boundary) shifting by its width is equal to the change in the entropy d_iS as a result of the diffusion redistribution of components in the same region R. We consider a quasi-stationary process obeying the condition [7]

$$\frac{dS}{dt} = \frac{d_iS}{dt} + \frac{d_eS}{dt} = 0,$$

which means that the total entropy change in the moving open system is zero (this condition is valid at a constant transformation front velocity v). In order to pass from the rate of entropy change to the rate of free energy release, we can use the relation (valid at a constant temperature and pressure)

$$\frac{dS_{i,e}}{dt} = -\frac{1}{T}\frac{dG_{i,e}}{dt}.$$

In this case, the rate of the free energy release is [8, 9]

$$\Psi \equiv T\frac{d_iS}{dt} = T\int_V \sigma dV = -\frac{d_iG}{dt} = \frac{d_eG}{dt} > 0. \qquad (4)$$

The entropy production as a result of the diffusion redistribution of components in the region R can be written as [8–10]

$$\Psi = \frac{hb}{\Delta z}\int_0^{\Delta z} IX\,dz = \frac{hb}{\Delta z}\int_0^{\Delta z}(-s\tilde{D})\frac{\partial c(z)}{\partial z}\left(-\frac{\partial\tilde{\mu}(z)}{\partial z}\right)dz, \quad (5)$$

where I is the generalized flux along the z axis, X is the driving force, and $\tilde{\mu}(z) = \mu_A - \mu_B = \dfrac{\partial g}{\partial c_A}$ is the generalized chemical potential at a point z of the region R.

Let us determine the change in the Gibbs potential as a result of the transformation of the α_0 phase in an element $dz + dz'$ at the point z of the interphase boundary. For this element, transformed into a band of the α phase of length dz and a band of the β phase of length dz', the law of conservation of the substance yields

$$c_0(dz + dz') = c(z)dz + c^{\beta}dz'. \quad (6)$$

The change in the Gibbs potential per unit volume can be written as

$$\Delta G(z) = g(c(z))dz + g^{\beta}dz' - g(c_0)(dz + dz'), \quad (7)$$

where $g(c(z))dz$ is the Gibbs potential of the α phase band of length dz at the point z with the concentration $c(z)$ in the region R, g^{β} is the Gibbs potential of the β phase, and $g(c_0)$ is the Gibbs potential in the supersaturated α_0 phase in front of the transformation boundary. Expanding the Gibbs potential for the α and α_0 phases into the Taylor series with respect to $g(c^{\alpha/\beta})$ and retaining terms up to the second order (which is permissible for regular solutions with a large energy of mixing), we obtain

$$\Delta G = \frac{1}{2}\left[(c(z) - c^{\alpha/\beta})^2 - \frac{c^{\beta} - c(z)}{c^{\beta} - c_0}(c_0 - c^{\alpha/\beta})^2\right] \times g''|_{c^{\alpha/\beta}} = f(c(z))k, \quad (8)$$

where $f(c(z)) < 0$ and $k = g''|_{c^{\alpha/\beta}} > 0$ is the curvature of the Gibbs potential surface in the α phase, at the point with the concentration $c^{\alpha/\beta}$.

The driving force can be expressed as

$$X = -\frac{\partial\tilde{\mu}}{\partial z} = -\frac{\partial c(z)}{\partial z}k,$$

where

$$\tilde{\mu} = \frac{\partial\Delta G}{\partial c(z)} = \left[(c(z) - c^{\alpha/\beta}) - \frac{(c_0 - c^{\alpha/\beta})^2}{2(c^{\beta} - c_0)}\right]k. \quad (9)$$

The rate of the free energy release as a result of the phase transformation in the region R can be written as

$$\Psi = \frac{d_eG}{dt} = -\frac{vb}{\Delta z}\int_0^{\Delta z}\Delta G(c(z))dz - g^{\alpha/\beta}bv. \quad (10)$$

Here, the first term in the right-hand part is the energy gain per unit volume and the second term corresponds to the formation of a new boundary region of length h between the α and β phases. The Gibbs potential per unit volume is $g^{\alpha/\beta} = \dfrac{2\gamma}{\Delta z}$, where γ is the free energy per unit area of the α–β interface.

Using expressions (2), (4), (5), (8)–(10) and integrating with respect to z, we eventually obtain

$$\Psi = \frac{d_eG}{dt} = -\frac{kLv}{16\Delta z}(c_0 - c^{\alpha/\beta})^2\left\{\frac{\Delta z}{L}\mathrm{sech}^2\left(\frac{\Delta z}{L}\right) - \frac{3c^{\beta} - c_0 - 2c^{\alpha/\beta}}{(c^{\beta} - c_0)}\tanh(\Delta z/L)\right\} - \frac{2\gamma v}{\Delta z} \quad (11)$$

$$= -\frac{d_iG}{dt} = \frac{kLv}{2\Delta z}(c_0 - c^{\alpha/\beta})^2\left\{\tanh(\Delta z/L) - \frac{\Delta z}{L}\mathrm{sech}^2\left(\frac{\Delta z}{L}\right)\right\}.$$

This equation determines the first relation between Δz and L:

$$kL(c_0 - c^{\alpha/\beta})^2 = 8\gamma\left\{\frac{\Delta z}{L}\mathrm{sech}^2\left(\frac{\Delta z}{L}\right) - \frac{2c^{\alpha/\beta} - c_0 - c^{\beta}}{c^{\beta} - c_0}\tanh\left(\frac{\Delta z}{L}\right)\right\}^{-1}. \quad (12)$$

Once this relationship is established, we can use the principle of maximum rate of the free energy release for determining the optimum Δz from the condition

$$\frac{d\Psi}{d(\Delta z)} = 0. \quad (13)$$

The explicit expression (13) is very complicated. For this reason, let us use a numerical method for finding the maximum of expression (11) with respect to Δz under the condition (12). As a result, we obtain a solution to the system of equations (12) and (13) by determining the values of $\Delta z = \Delta z^{\mathrm{SOL}}$ and L for the given values of the triple product $s\tilde{D}h$ and the equilibrium concentration $c^{\alpha/\beta}$. For the comparison with experiment, we will use the data for a Ni–1.4 at. % In system at 703 K [1] with the following model parameters: $k = 1.075 \times 10^{11}$ J/m^3; $\gamma = 0.5$ J/m^2; $c_0 = 1.4$ at. %; $c^{\alpha/\beta} = 0.43$ at. %; $c^{\beta} = 25$ at. %; and $s\tilde{D}h = 2.12 \times 10^{-24}$ m^3/s.

The calculations yield values of parameters coinciding with the experimental values: the average concentration in the cell, $c_1 = 0.82$ at. %; the interlamellar dis-

tance, $\Delta z^{SOL} = 0.134 \times 10^{-6}$ m; and the Cahn parameter, $C = 9.2$. The transformation boundary velocity is determined by the formula $v = s\tilde{D}h/L^2 = 2.7 \times 10^{-10}$ m/s. For the given parameters, the change in the Gibbs free energy determined by integrating relation (8) and taking into account the surface energy is $\Delta G = -14.6$ J/mol, which coincides with the experimental value.

Conclusions. Using the equation of balance of the entropy fluxes at the phase transformation front, we obtain a new scheme for determining the main parameters of discontinuous precipitation without using the Cahn assumption concerning a linear relationship between the driving force and the transformation front velocity (the form of this relationship can be established in the course of calculations). The proposed scheme allows additional ways of the energy degradation in the transformation region to be taken into account, in particular, those related to a reduced mobility of the interphase boundary or to the presence of driving forces of various kinds.

Acknowledgments. The author is grateful to A.M. Gusak and O.A. Shmatko for discussion of the problem formulation and results.

This study was supported by the INTAS Foundation, grant no. 00784.

REFERENCES

1. I. Kaur and W. Gust, *Fundamentals of Grain and Interphase Boundary Diffusion* (Ziegler, Stuttgart, 1989; Mashinostroenie, Moscow, 1991).
2. L. N. Larikov and O. A. Shmatko, *Discontinuous Precipitation of Oversaturated Solid Solutions* (Naukova Dumka, Kiev, 1976).
3. J. W. Cahn, Acta Metall. **9**, 795 (1961).
4. A. G. Khachaturyan, *The Theory of Phase Transformations and the Structure of Solid Solutions* (Nauka, Moscow, 1974).
5. J. W. Cahn, Acta Metall. **7**, 18 (1959).
6. G. R. Speich, Trans. Metall. Soc. AIME **242**, 1359 (1968).
7. H. Ziegler, in *Progress in Solid Mechanics*, Ed. by I. N. Sneddon and R. Hill (North-Holland, Amsterdam, 1963), Vol. 4, Chap. 2, pp. 93–192.
8. S. R. De Groot and P. Mazur, *Nonequilibrium Thermodynamics* (North-Holland, Amsterdam, 1962; Mir, Moscow, 1964).
9. I. Gyarmati, *Nonequilibrium Thermodynamics* (Springer, Berlin, 1970; Mir, Moscow, 1974).
10. J. S. Kirkaldy and D. J. Young, *Diffusion in the Condensed State* (The Institute of Metals, London, 1987).

Translated by P. Pozdeev

Technical Physics Letters, Vol. 30, No. 2, 2004, pp. 113–116. Translated from Pis'ma v Zhurnal Tekhnicheskoĭ Fiziki, Vol. 30, No. 3, 2004, pp. 62–67.

Intermediate Phases in the Region of a Morphotropic Transition and the Properties of Ferroelectric Piezoceramics

O. A. Demchenko*, L. A. Reznichenko, L. A. Shilkina, A. V. Turik, O. N. Razumovskaya, and S. I. Dudkina

Institute of Physics, Department of Physics, Rostov State University, Rostov-on-Don, Russia

**e-mail: olesia_demch@mail.ru*

Revised manuscript received August 11, 2003

Abstract—It is established that the region of a morphotropic phase transition in ternary solid solution systems based on lead zirconate titanate exhibits a complicated structure. The maxima of the physical characteristics of solid solutions in this morphotropic phase transition region are determined to a considerable extent by an intermediate phase. A series of solid solutions with good prospects for applications in high-temperature piezoceramics technology are found. © *2004 MAIK "Nauka/Interperiodica".*

In recent years, it was reported [1–4] that binary oxide systems of the lead zirconate titanate (PZT) type contain an intermediate phase in the region of a morphotropic phase transition (MPT), which accounts for the high piezoelectric properties of the corresponding solid solutions. This stimulated us to study in more detail the corresponding phase diagram region in two PZT-based three-component systems with the third component being $BaW_{1/3}Be_{2/3}O_3$ or "$SrW_{1/3}Bi_{2/3}O_3$." The former, $BaW_{1/3}Be_{2/3}O_3$, is a ferroelectric compound possessing a perovskite-like structure with a rhombohedral reduced cell at temperatures below the Curie temperature (T_C = 450°C) [5]; "$SrW_{1/3}Bi_{2/3}O_3$" is a hypothetical compound. The choice of these compounds was related to the expected possibility of obtaining high piezoelectric parameters (ensured by the "ferroelectrically soft" Ba and Sr cations) and high T_C values (characteristic of Bi-containing compositions).

The solid solution compositions corresponded to the formulas $0.98Pb(Ti_xZr_{1-x})O_3$–$0.02BaW_{1/3}Bi_{2/3}O_3$ (system 1) and $0.98Pb(Ti_xZr_{1-x})O_3$–0.02"$SrW_{1/3}Bi_{2/3}O_3$" (system 2) with $0455 \le x \le 0.49$. Since the content of the third components is small, the phase diagrams of these systems have to be close to that of the base system (PZT). The interval of variation of the parameter x provides for the formation of solid solution in the MPT region. The samples of solid solutions were prepared using the standard ceramic technology. The X-ray diffraction measurements were performed on a DRON-3 diffractometer using Mn-filtered FeK_α radiation. The dielectric, piezoelectric, and elastic characteristics, including the Curie temperature, the permittivities of the nonpolarized ($\varepsilon/\varepsilon_0$) and polarized ($\varepsilon_{33}^T/\varepsilon_0$) samples, the dielectric loss tangent $\tan\delta$, the electromechanical coupling factor K_p, the piezoelectric coefficient d_{31}, and the mechanical figure of merit Q_m, were determined according to the State Standard OST 11-0444-87.

An analysis of the X-ray diffraction patterns of the solid solutions belonging to both systems (Fig. 1) showed that the samples with x = 0.49 are characterized by 002 and 200 reflections of the tetragonal (T) phase in the region of $55° < 2\theta < 59°$, with the background intensity between these lines being much greater than outside the multiplet. In addition, there is a strongly smeared diffuse maximum related to the appearance of clusters of a new phase with an interplanar spacing of d = 2.04 Å. For x = 0.48, this diffuse maximum becomes more pronounced and there appears another weak maximum near the 200 line on the side of smaller θ angles. The former maximum corresponds to the 200 reflection of a pseudocubic (PSC) phase with a lattice parameter of $a \approx 4.08$ Å, and the second, to the 200 reflection of clusters of a rhombohedral (Rh) phase. Under the experimental conditions studied, it was impossible to determine the symmetry of the intermediate PSC phase with greater precision.

As can be seen in Fig. 1, the corresponding X-ray diffraction lines are strongly smeared and overlapped, which is related to a complex phase composition of solid solutions and close unit cell parameters of the component phases. The size of the coherent scattering regions of the new phases is small (≤300 Å), which also leads to line broadening. In the solid solution studied, the oxygen octahedra contain W and Bi ions in addition to Ti and Zr ions. The higher scattering power of the former ions leads to a further increase in intensity of the diffuse maxima, thus more significantly distorting the

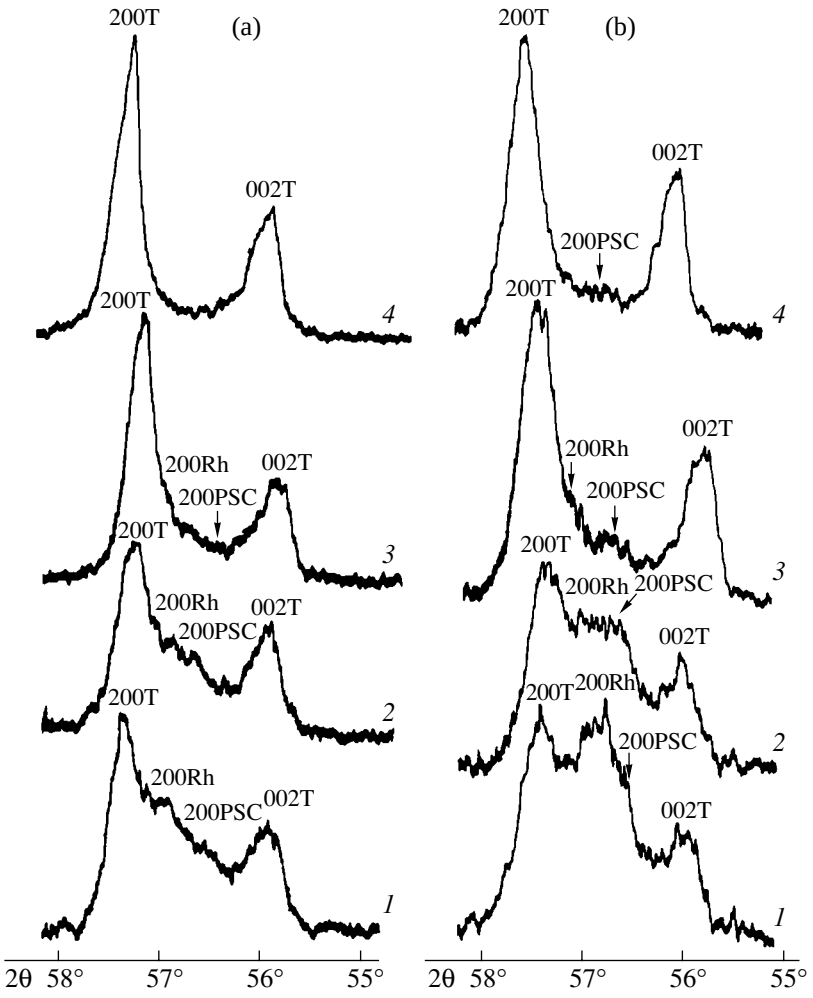

Fig. 1. X-ray diffraction patterns of the solid solutions of (a) system 1 and (b) system 2 with x = 0.455 (*1*), 0.465 (*2*), 0.48 (*3*), and 0.49 (*4*).

profiles of diffraction lines. As the x value decreases, the intensities of the diffuse maxima grow, while the intensities of lines corresponding to reflections of the T phase (i.e., the fraction μ_T^* of the T phase) decrease and their widths increase. For x = 0.46, the fractions of the PSC and Rh phases are almost equal (Fig. 1), while for x = 0.455, the Rh phase begins to dominate.[1]

It should be noted that the MPT regions in the systems studied contain composition intervals in which the structural and piezoelectric characteristics are almost constant or vary very slightly (Fig. 2). These intervals are adjacent to (or closely spaced from) the boundaries of transitions to the single-phase (T or Rh) regions. Outside these intervals, the parameters of the samples exhibit significant changes with the composition. The piezoelectric characteristics exhibit extrema (maxima of $\varepsilon/\varepsilon_0$, $\varepsilon_{33}^T/\varepsilon_0$, $\tan\delta$, d_{31}, and K_p and a minimum of Q_m) in the MPT region on the intervals of constant structural parameters where the amount of the intermediate phase is maximum.

Apparently, the maxima in the piezoelectric characteristics are favored by phase separation in the MPT region, whereby the system decomposes into T and Rh phases at a sufficiently high (~18%) concentration of the intermediate phase. This highly complicated heterophase system is characterized by facilitated motions of the interphase and domain boundaries, which accounts for the increased response to external electrical and mechanical actions. Thus, we may speak of an important role of the intermediate phase as determining

[1] The percentage fractions of the T (μ_T), PSC (μ_{PSC}), and Rh (μ_{Rh}) phases were determined using the formulas $\mu_T = 100 - (\mu_{PSC} + \mu_{Rh})$, $\mu_{PSC} = (T_{200}^{PSC}\,100)/(I_{200}^T + I_{002}^T + I_{200}^{Rh} + I_{200}^{PSC})$, and $\mu_{Rh} = (I_{200}^{Rh}\,100)/(I_{200}^T + I_{002}^T + I_{200}^{Rh} + I_{200}^{PSC})$, respectively, where I_{200} and I_{002} are the peak intensities of the corresponding reflections (the regions of pure T and Rh compositions were not studied).

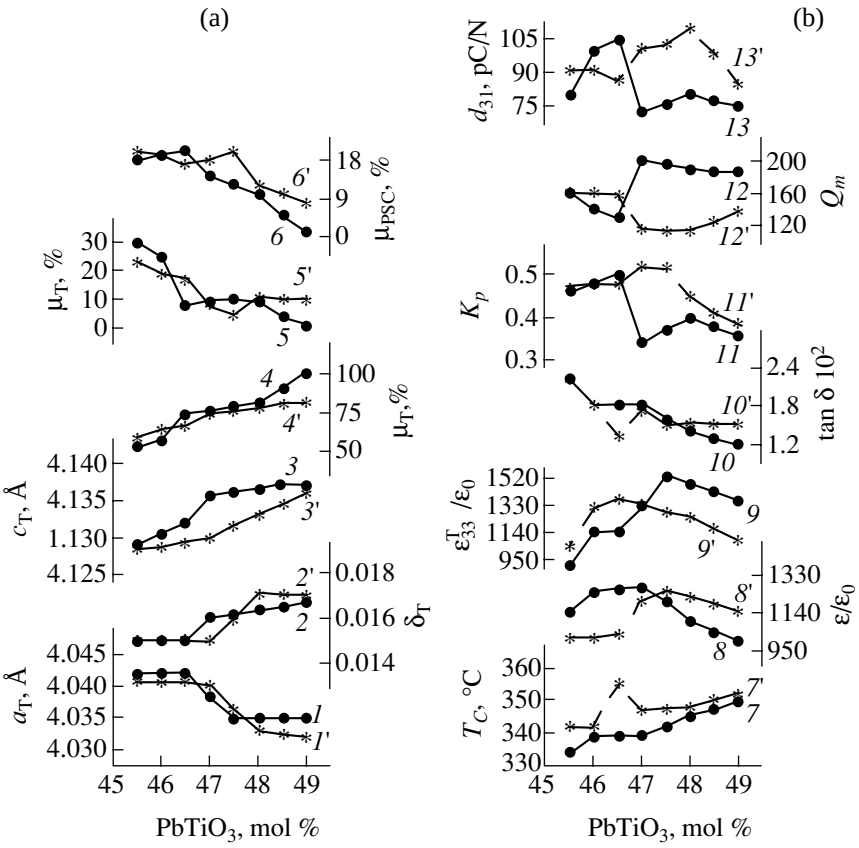

Fig. 2. Concentration dependences of the (a) structural and (b) piezoelectric characteristics of the solid solutions of system 1 (black circles) and system 2 (asterisks): (*1*, *1*') a_T; (*2*, *2*') δ_T; (*3*, *3*') c_T; (*4*, *4*') μ_T; (*5*, *5*') μ_{Rh}; (*6*, *6*') μ_{PSC}; (*7*. *7*') T_C; (*8*, *8*') $\varepsilon/\varepsilon_0$; (*9*, *9*') $\varepsilon_{33}^T/\varepsilon_0$; (*10*, *10*') $\tan\delta$; (*11*, *11*') K_p; (*12*, *12*') Q_m; (*13*, *13*') d_{31}. Note: $\delta_T = (2/3)(c/a - 1)$ is the parameter of homogeneous deformation of the *T* cell.

the structural and electrical properties of the solid solutions studied.

An analysis of the results presented in Fig. 2 and the published data [6] showed that dielectric, piezoelectric, and elastic characteristics of solid solutions usually vary (together with the structural parameters) in a smooth manner within single-phase regions far from the MPTs and change nonmonotonically (also together with the structural parameters) in the heterogeneous regions in the vicinity of the MPT, where the clusters of a new intermediate phase are formed. These characteristics exhibit extrema near or inside the MPT regions (on the intervals of constant structural parameters), where the amount of the intermediate phase is maximum. This behavior of physical properties in the MPT region, as well as that in the PZT system, is evidence of a complicated structure of this region in the phase diagram. The nature of this region, as well as the factors responsible for its two-phase character, inspired a discussion [6, 7] that is still continued.

As the number of components in the system increases, the phase diagram becomes more and more complicated. An additional contribution to the phase decomposition of solid solutions can be related to differences in the diffusion activity of various cations. We believe that this factor accounts for the fact that an intermediate phase was originally observed in the most complicated of the known multicomponent systems [8], including cations of eight types.

Based on the obtained results, we may separate a series of solid solutions with $x = 0.456$–0.47 that have good prospects for practical applications. Sufficiently high values of T_C (~365°C), K_p (~0.53), and d_{31} (~100 pC/N) in combination with low $\tan\delta$ (~1.8×10^{-2}) and Q_m (~120) suggest that solid solutions with such properties can serve a base for high-temperature broadband transducers. In contrast to all the existing high-temperature materials characterized by reduced or low $\varepsilon_{33}^T/\varepsilon_0$ values (~50–500), favoring their use in high-frequency devices, the solid solutions obtained for the first time in this study possess much higher values of this parameter ($\varepsilon_{33}^T/\varepsilon_0 \sim 1300$–$1400$). This property makes such ceramics the best candidates for use in

high-temperature piezoelectric devices operating in the medium frequency range.

Acknowledgments. This study was supported by the Russian Foundation for Basic Research, project no. 02-02-17781.

REFERENCES

1. B. Noheda, D. E. Cox, G. Shirane, *et al.*, Appl. Phys. Lett. **74**, 2059 (1999).
2. B. Noheda, J. A. Gonzalo, R. Guo, *et al.*, Phys. Rev. B **61**, 8687 (2000).
3. V. Yu. Topolov and A. V. Turik, Fiz. Tverd. Tela (St. Petersburg) **43**, 1525 (2001) [Phys. Solid State **43**, 1585 (2001)].
4. V. Yu. Topolov and A. V. Turik, Fiz. Tverd. Tela (St. Petersburg) **44**, 1295 (2002) [Phys. Solid State **44**, 1355 (2002)].
5. Yu. N. Venevtsev, E. D. Politova, and S. A. Ivanov, *Ferroelectrics and Antiferroelectrics in the Barium Titanate Family* (Khimiya, Moscow, 1985).
6. A. V. Turik, Kristallografiya **26**, 171 (1981) [Sov. Phys. Crystallogr. **26**, 94 (1981)].
7. V. A. Isupov, Fiz. Tverd. Tela (Leningrad) **12**, 1380 (1970) [Sov. Phys. Solid State **12**, 1084 (1970)].
8. Ya. B. Bogosova, G. M. Konstantinov, and M. F. Kupriyanov, Izv. Ross. Akad. Nauk, Ser. Fiz. **57** (6), 89 (1993).

Translated by P. Pozdeev

Technical Physics Letters, Vol. 30, No. 2, 2004, pp. 117–119. Translated from Pis'ma v Zhurnal Tekhnicheskoĭ Fiziki, Vol. 30, No. 3, 2004, pp. 68–74.

Subnanosecond 1-GW Pulsed 38-GHz Radiation Source

S. D. Korovin, G. A. Mesyats, V. V. Rostov*, M. R. Ul'maskulov, K. A. Sharypov, V. G. Shpak, S. A. Shunailov, and M. I. Yalandin**

Institute of Electrophysics, Ural Division, Russian Academy of Sciences, Yekaterinburg, Russia
Institute of High-Current Electronics, Siberian Division, Russian Academy of Sciences, Tomsk, Russia
*e-mail: * rostov@ife.hcei.tsc.ru; ** yalandin@iep.uran.ru*

Received July 14, 2003

Abstract—The regime of excitation of subnanosecond high-power microwave pulses has been studied in a Cherenkov device with an extended periodic slow-wave structure, using an electron beam from a compact pulsed high-current electron accelerator (290 keV, 2.3 kA, 1 ns). Conditions are established for which the power conversion coefficient can reach up to 1.5 at an output pulse power of 1.2 GW and a pulse duration of 200 ps.

Previously [1–5], we performed a series of theoretical and experimental investigations devoted to nonstationary regimes in relativistic microwave generators and demonstrated the possibility of obtaining electromagnetic radiation pulses with a peak power not limited by the pumping beam power. This direction in relativistic electronics offers attractive physical means of energy conversion and provides for the most complete realization of the possibilities of compact high-current electron accelerators. The experimental findings [2–5] were supported by the development of theoretical models and numerical methods, which provided conditions for a significant increase in the energy efficiency and the power conversion coefficient of microwave radiation sources. The present study was aimed at reaching this goal.

We have studied a Cherenkov electron generator for a 38 GHz range, representing an extended periodic slow-wave structure (SWS) with electron-beam-synchronized spatial harmonic of the TM_{01} backward wave. The new experiments required significant modification of the setup used previously [2]. The electron accelerator system, based on a small-size high-voltage generator of the RADAN-303BP type with a capacitive energy storage in the form of a double pulse-forming line, was modified so as to provide for a better stabilization of the accelerating voltage pulses. The pulse-forming line was switched by a controlled high-voltage discharger with field distortion near the grounded electrode [6], which ensured the generator start with a total time scatter not exceeding 50 ns at a pulsed storage charge time of 8 μs. This provided for stabilization of the uncontrolled pulse-shaping nitrogen-filled discharger in an additional inductance–capacitance pulse compression unit [7] generating an accelerating voltage pulse with a pronounced quasi-flat top plateau of 0.9-ns duration and 200-ps front width (Fig. 1). In addition to stabilization, the controlled start of the main discharger ensured skipless operation at a voltage (190–195 kV) close to the maximum charging level. This modification provided for a 10–15% increase in the electron diode current for the same cathode voltage (~290 kV as in [2]) and allowed the beam current to be increased up to 670–700 MW.

The electron injector parameters and the diode geometry were modeled in a numerical experiment using the particle-in-cell method (PIC code KARAT) [8]. The numerical modeling was used for optimization of the SWS geometry and the strength and configuration of the magnetic field transporting the electron beam with preset parameters. In selecting the SWS

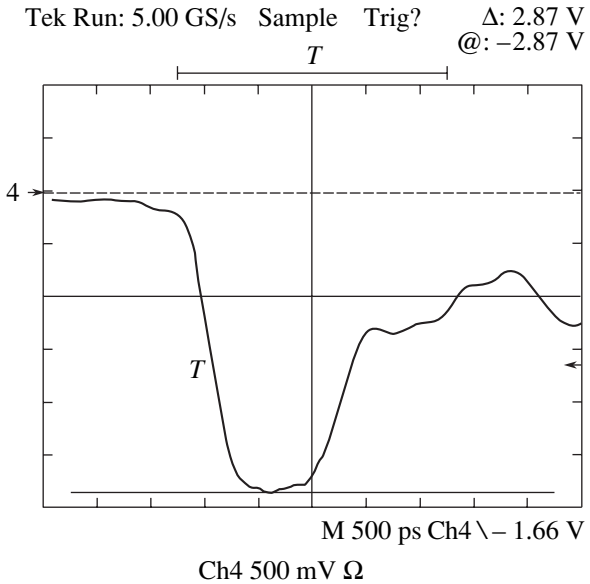

Fig. 1. The typical accelerating voltage pulse as measured by a Tektronix TDS684B oscillograph with a transient time of 350 ps.

1063-7850/04/3002-0117$26.00 © 2004 MAIK "Nauka/Interperiodica"

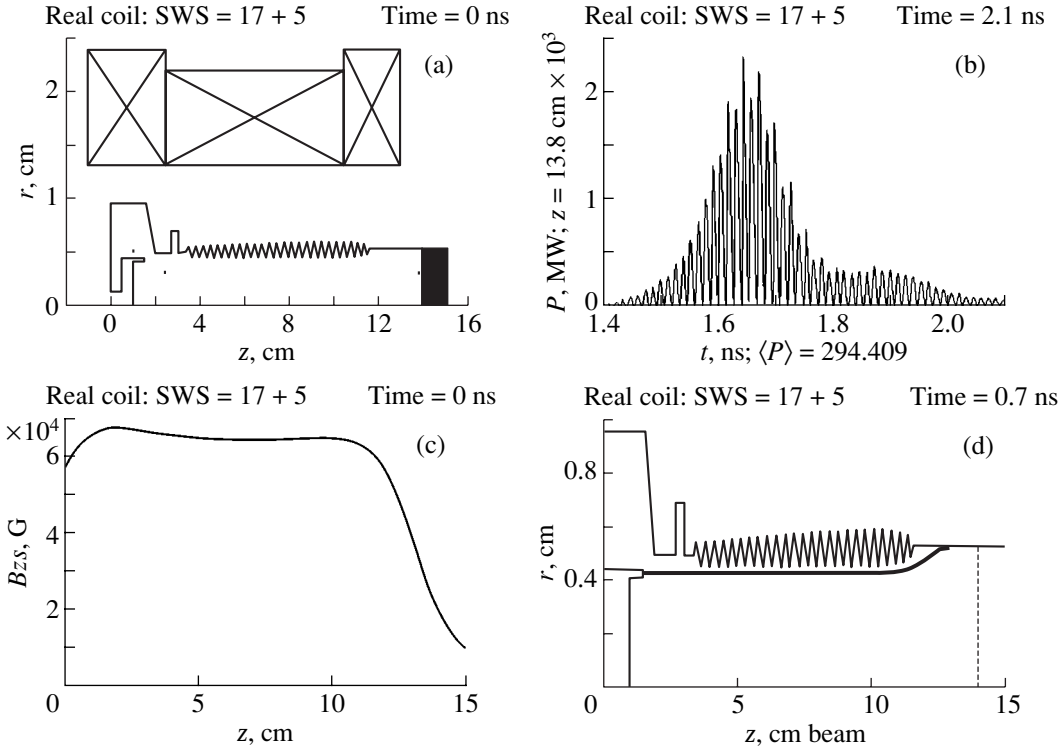

Fig. 2. The results of numerical modeling of a backward-wave tube generating subnanosecond pulses: (a) electron injector, focusing solenoid, and SWS geometry; (b) nonaveraged power flux of microwave pulses; (c) magnetic field profile along the SWS axis; (d) tubular electron beam trajectory.

configuration and the longitudinal profile of the beam–wave coupling resistance, we used the results of the numerical analysis of a one-dimensional model [4]. The optimized SWS had a median diameter of 1.3λ and a total length accommodating 25 corrugation periods (Fig. 2a). The electromagnetic pulse was reflected from the cathode end by a lumped broadband reflector [9] reflecting no less than 95% of the incident pulse energy.

According to the results of numerical modeling (Fig. 2b), the calculated peak power of the electromagnetic pulse could exceed 1 GW at a power conversion coefficient of 1.7. The best results were obtained for a sufficiently strong magnetic field (6.5 T) profiled as depicted in Fig. 2c, which was necessary for ensuring high-quality beam transport near the SWS walls. The coupling resistance at the cathode end of SWS was additionally reduced at the expense of beam decompression at the input end of the solenoid (Fig. 2d). The beam was displaced away from corrugations in the region of maximum values of the electromagnetic field intensity in the generated wave, which causes strong transverse oscillations and significant losses of electrons to the SWS walls (by analogy with the case of a homogeneous magnetic field).

In manufacturing the solenoid, the main attention was given to meeting the requirement of minimum deviations of the coil axis from the SWS axis (not to exceed 0.1 mm). The pulsed magnetic system was calibrated taking into account the decrease in the field strength as a result of the skin effect. Variation of the pulsed magnetic field along the axis of the electron-optic system was measured by an inductive sensor. The measurements were performed at the first maximum synchronized with the electron beam. The real field line configuration was taken into account for correcting the diameter of the tubular graphite cathode. During experiments, the time interval between accelerator pulses (60 s) was selected depending on the solenoid heating.

The parameters of the output subnanosecond microwave pulses were measured using semiconductor detectors and the calorimetric technique. The noncooled hot-carrier germanium detector and calorimeter were identical to those used previously [2, 5]. The diameter of the calorimeter detector capillary was 200 μm. The results of calibration measurements in the energy range from 50 to 500 mJ showed that the device response was linear to within 5%. For a sensitivity of about 8 mm/J, observations on an optical microscope allowed the absorbed microwave pulse energy to be reliably detected on a level of 300–400 mJ.

The microwave pulse envelope from the semiconductor detector output was fed to an S7-19 oscillograph with a 5-GHz bandwidth. The oscillograph sweep and vertical sensitivity were calibrated using test pulses with a 90-ps front width from a G5-84 oscillator, with simultaneous monitoring of the master signal using a

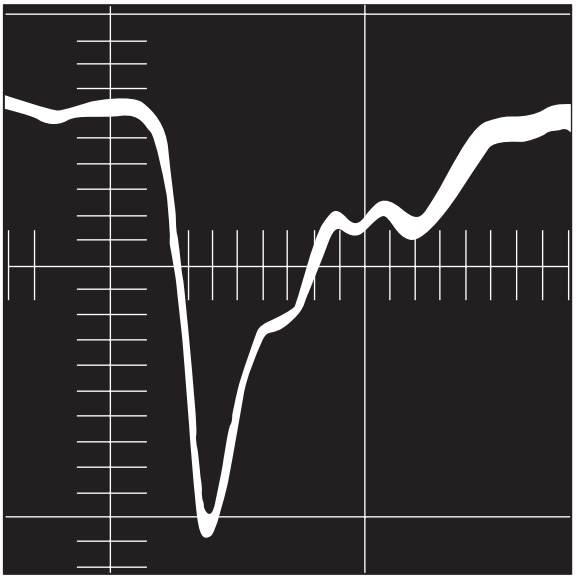

Fig. 3. The typical pulse with a 120-ps front measured with a germanium microwave detector and monitored by an S7-19 oscillograph (sweep, 1 ns/div). With allowance for the detector nonlinearity, the signal has FWHM not exceeding 200 ps.

6-GHz Tektronix TDS820 digital storage oscillograph. The same method was used to calibrate the detector output tract and the delay line of the S7-19 oscillograph, made of an RG405 microwave cable.

Using real-time calibration measurements performed in the measuring tracts as described in [2, 5], we have determined the amplitude attenuation coefficients, the degree of broadening, and the degree of front blurring of the test pulses modeling to within 5% the temporal characteristics of the microwave detector output signal. With allowance for a thorough calibration of the nonlinear characteristic of the microwave detector, these measures allowed the form-factor of the microwave pulse envelope to be calculated and the peak power of subnanosecond microwave pulses in an 8-mm range to be determined with a 20% accuracy (Fig. 3). For the typical calorimeter readings of 300–410 mJ, this peak power amounted to 0.9–1.25 GW.

It should be noted that the experimental data agree with the results of numerical modeling. The gigawatt microwave pulse duration (FWHM) did not exceed 200 ps. To within the experimental accuracy indicated above, the coefficient of the electron beam power conversion to the microwave radiation was 1.5 ± 0.2. In this case, the radiant flux density in the SWS could be as high as ~1.5 GW/cm^2. The efficiency of energy conversion in the "electron beam–electromagnetic wave" system for the microwave source studied can be estimated at 20–30%.

The high-voltage generator of the accelerator (RADAN-303BPM) can be operated in a pulsed-periodic regime with a pulse repetition rate of up to 100 Hz. Using a hybrid modulator [10], the repetition rate can be increased up to 3500 Hz [5]. Such operation regimes are of interest in systems with superconducting solenoids. Taking into account that the experiments were performed with a small-size high-voltage accelerator, the proposed microwave source can be used both for solving various research problems and in applications.

Acknowledgments. The authors are grateful to N.S. Ginzburg for his interest in this study and to A.I. Klimov for valuable advice.

This study was supported by the Russian Foundation for Basic Research, project no 01-02-17029.

REFERENCES

1. N. S. Ginzburg, I. V. Zotova, and A. S. Sergeev, Pis'ma Zh. Tekh. Fiz. **25** (23), 8 (1999) [Tech. Phys. Lett. **25**, 930 (1999)].
2. S. D. Korovin, G. A. Mesyats, V. V. Rostov, *et al.*, Pis'ma Zh. Tekh. Fiz. **28** (2), 81 (2002) [Tech. Phys. Lett. **28**, 76 (2002)].
3. A. A. El'chaninov, S. D. Korovin, I. V. Pegel', *et al.*, Izv. Vyssh. Uchebn. Zaved., Radioélektronika **46** (3–4), 55 (2003).
4. A. A. El'chaninov, S. D. Korovin, V. V. Rostov, *et al.*, Pis'ma Zh. Éksp. Teor. Fiz. **77**, 314 (2003) [JETP Lett. **77**, 266 (2003)].
5. D. M. Grishin, V. P. Gubanov, S. D. Korovin, *et al.*, Pis'ma Zh. Tekh. Fiz. **28** (19), 24 (2002) [Tech. Phys. Lett. **28**, 806 (2002)].
6. V. G. Shpak, S. A. Shunailov, and M. I. Yalandin, in *Proceedings of the 10th IEEE International Pulsed Power Conference, Albuquerque, 1995*, pp. 544–549.
7. M. I. Yalandin and V. G. Shpak, Prib. Tekh. Éksp., No. 3, 5 (2001).
8. V. P. Tarakanov, *User's Manual for Code KARAT* (Berkley, Springfield, 1992).
9. S. D. Korovin, I. K. Kurkan, V. V. Rostov, *et al.*, Izv. Vyssh. Uchebn. Zaved., Radiofiz. **42**, 1189 (1999).
10. S. K. Lyubutin, G. A. Mesyats, S. N. Rukin, *et al.*, Prib. Tekh. Éksp., No. 5, 80 (2001).

Translated by P. Pozdeev

Technical Physics Letters, Vol. 30, No. 2, 2004, pp. 120–122. Translated from Pis'ma v Zhurnal Tekhnicheskoĭ Fiziki, Vol. 30, No. 3, 2004, pp. 75–81.

Electrically Controlled Integrated Optical Filter

M. P. Petrov, A. V. Chamrai*, A. S. Kozlov, and I. V. Il'ichev

Ioffe Physicotechnical Institute, Russian Academy of Sciences, St. Petersburg, 194021 Russia

**e-mail: achamrai@mail.ioffe.ru*

Received July 21, 2003

Abstract—The possibility of electric control over the spectral transfer function of an integrated optical filter comprising a reflection Bragg grating in a photorefractive waveguide is demonstrated for the first time. The filter has a spectral selectivity of 0.15 nm, ensures continuous tuning within ~0.1 nm, and can be electrically switched on and off. The proposed method of control is effective and has good prospects for practical applications. © *2004 MAIK "Nauka/Interperiodica".*

Controlled narrowband optical filters are of considerable interest for various fields of laser technology, optical instrument building, and especially fiber-optic telecommunication systems based on the principles of wavelength division multiplexing (WDM). Electrically controlled filters, especially attractive in integrated-optics design, provide for a high-speed response, require relatively low control voltages, are compatible with fiber-optic line components, and can be manufactured on a commercial level.

Although the general principles of filters in integrated-optics design have been known for some time [1], the electrically controlled filters with a very narrow transmission band (on the order of 0.1 nm) necessary for WDM systems were not developed until quite recently [2]. The possibilities of continuous tuning in such filters are very restricted because of the relatively weak electrooptical response of the crystals (e.g., lithium niobate) suited for these purposes. On the other hand, our theoretical analysis showed that the electrooptical response of the available $LiNbO_3$ crystals is quite sufficient for controlling the spectral transfer function of a filter, which is even of greater interest than simple tuning for WDM systems. Therefore, investigation of the possibility of controlling the shape of the spectral transfer function, rather than the passband position of the filter, is of special importance.

This paper is the first experimental demonstration of the electric control over the shape of the spectral transfer function of an integrated optical filter. This possibility significantly expands the functionality of such devices and opens prospects for new practical applications.

The proposed device is based on a volume reflection Bragg grating recorded in an optical waveguide formed in an electrooptical material. The grating is characterized by a high spectral selectivity $\Delta\lambda/\lambda_0 \sim \Lambda/T$, where $\Delta\lambda$ is the bandwidth of the filter, λ_0 is the central wavelength, Λ is the grating period, and T is the grating length in the direction of light propagation. It is assumed that the grating refractive index amplitude n_1 is small as compared to Λ/n_0T, where n_0 is the effective index of the given waveguide mode. The Bragg condition for this grating is $\lambda_0 = 2\Lambda n_0$. Since the grating is recorded in an electrooptical crystal, the effective index n_0 and, hence, the central wavelength λ_0 can be controlled by applying an external electric field [2, 3]. The filter tuning without a change in shape of the spectral transfer function takes place when the applied field is homogeneous along the grating. The application of an inhomogeneous field will change the spectral transfer function, that is, modify the spectrum of reflected (diffracted) light. By setting a certain distribution of the applied electric field along the grating, it is possible to obtain the spectral transfer function of a desired shape.

Figure 1 shows a schematic diagram of the electrically controlled optical filter. The substrate was an X-cut $LiNbO_3$ crystal in which an optical waveguide was formed using the well-developed technology based on the thermal diffusion of titanium [4]. A 10-mm-long waveguide with a width of 10 μm in the substrate plane, formed on the crystal surface, enabled single-mode

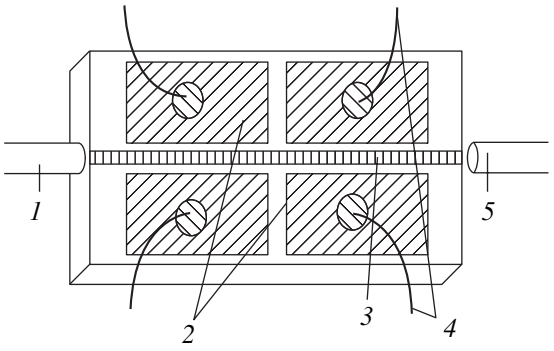

Fig. 1. Schematic diagram of the electrically controlled integrated optical filter: (*1*) input fiber; (*2*) electrodes; (*3*) optical waveguide with recorded grating; (*4*) electric leads; (*5*) output fiber.

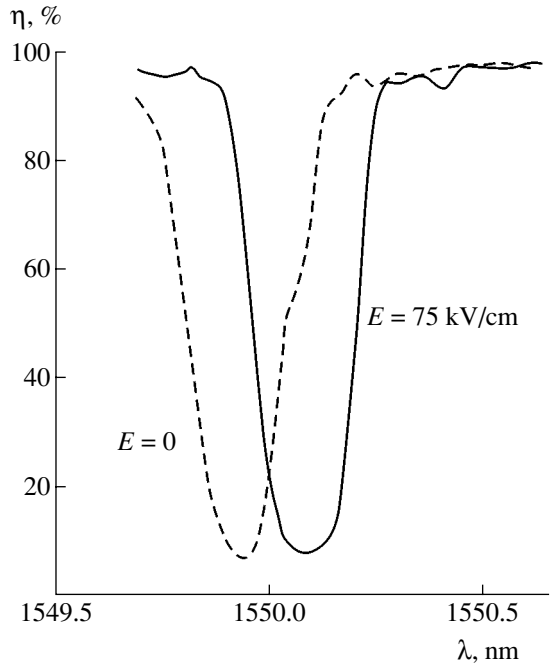

Fig. 2. Experimental demonstration of continuous tuning of the central wavelength of the integrated optical filter: dashed and solid curves show the spectra of optical transmission η measured before and after application of an external electric field, respectively.

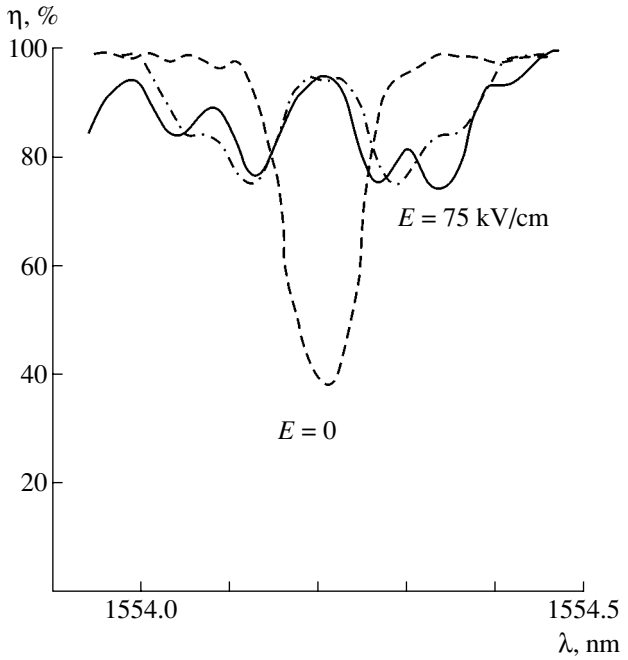

Fig. 3. Experimental demonstration of the electric control over the shape of the spectral transfer function of the integrated optical filter: dashed and solid curves show the spectra of optical transmission η measured before and after application of a external electric field, respectively; dash–dot curve shows the results of theoretical calculations.

operation in the 1500–1600 nm wavelength range. The reflection phase grating was formed by holographic recording at 532 nm using a YAG:Nd laser. The grating wavevector was directed along the waveguide axis, the grating period was equal to $\Lambda \approx 353$ nm, and the grating length (determined by the recording beam diameter) was $T = 9$ mm. The reading light beam of a laser tunable in the 1500–1620 nm range was introduced into the waveguide, extracted from it, and fed into a photodetector via optical fibers. In order to increase sensitivity to the recording light beam, the near-surface layer of the substrate was additionally diffusion-doped with copper ions.

The electric control was provided by means of a system of copper electrodes deposited onto the substrate surface on both sides of the waveguide. The electrode pads were spaced by $d = 20$ μm. For thin planar film electrodes, the electric field strength in the waveguide was $E \approx 2U\pi d$, where U is the voltage applied to the control electrodes. In order to increase the breakdown voltage and protect the waveguide from dust and moisture, the waveguide surface was covered with a silica film. This structure made it possible to obtain a sufficiently homogeneous electric field in the waveguide region, which was perpendicular to the C axis and had a strength of up to 80 kV/cm at an applied voltage of up to 250 V.

In the final stage of manufacture, the waveguide was connected to the input/output fiber optical pigtails. The spectral characteristics of the integrated optical filter were measured using a single-mode semiconductor laser tunable in a wavelength range from 1500 to 1620 nm at a 0.01-nm step. The spectral transfer function of the filter was determined by measuring the optical power at the filter output as a function of the readout light wavelength.

Figure 2 shows the spectral transfer functions of the filter measured before and after application of a control voltage producing a homogeneous electric field with a strength of 75 kV/cm. As can be seen from these data, the diffraction efficiency of the grating reaches 90%, the width of the spectrum (reflection bandwidth) is 0.15 nm, and the shift of the spectral transfer function in the applied field amounts to 0.1 nm. These values are in satisfactory agreement with the theory. Indeed, the absorption bandwidth determined as a full width at half maximum (FWHM) for a Bragg grating length of $T = 9$ mm is $\Delta\lambda = 1.778\lambda_0(\Lambda/T) \approx 0.11$ nm, while the shift of the central wavelength is $\delta\lambda_0 = n^2 r\lambda_0 E/2 = 0.096$ nm (r is the electrooptical coefficient of the crystal for the given electrooptical effect configuration: $r = r_{12} = 3.4$ pm/V for the TE mode, and $r = r_{22} = -r_{12}$ for the TM mode).

Figure 3 shows the change in shape of the spectral transfer function of the integrated optical filter observed when the applied field is inhomogeneous along the waveguide. The field is applied in such a manner that the whole grating can be represented as being

composed of two parts of equal length, the light reflected from the first part being shifted in phase by 180° relative to the light reflected from the second part. In this case, the quenching of reflection at the central wavelength is equivalent to the effect observed for the light diffraction from a sinusoidal grating with a phase jump of π in the middle [5, 6]. We have performed a theoretical calculation of the spectral transfer function for the Bragg grating with $\lambda_0 = 1554.2$ nm, $T = 9$ nm, $r_{eff} = 3.4$ pm/V, and the diffraction efficiency $\eta = 60\%$. As can be seen from Fig. 3, the result of this calculation fits the experiment well.

The above experimental data show that application of an inhomogeneous field offers a radical method of changing the spectral transfer function of the integrated optical filter. The filter controlled in this regime operates as a spectrally selective narrowband attenuator, light modulator, or spectral channel switch (of the so-called add/drop multiplexer type). Being of particular importance for WDM systems, these functions allow, for example, separation of a given spectral channel or leveling the light intensity and amplification coefficients of different channels. The filter can operate in both transmission and reflection geometry. The limiting control speed is determined by the reflection bandwidth. For a bandwidth of 0.1 nm, the filter response is restricted to a frequency on the order of 20 GHz. A significant advantage of the proposed filter is the integrated-optics design. By using a cascade of such devices arranged on the same substrate, it is possible to provide for the simultaneous controlled operation of several spectral channels.

In conclusion, it should be noted that the aim of this study was to show the principal possibility of real-time electric control over the shape of the spectral transfer function of an optical filter. We did not try to obtain a device possessing ultimate possible characteristics. By optimization of the regime of grating recording, electrode configuration, crystal orientation, and matching of the filter with optical fibers, it is possible to significantly improve the working parameters of the integrated optical filter.

Thus, we have developed and experimentally demonstrated an electrooptical device capable of controlling the shape of the spectral transfer function of a Bragg grating. Based on this method, we have designed and manufactured an electrically controlled integrated optical filter capable of continuously tuning the central wavelength within 0.1 nm at a bandwidth of 0.15 nm and providing for attenuation of the reflection coefficient at the central wavelength from 60 to 5%. These results show high efficacy of the proposed method and good prospects for its practical applications.

Acknowledgments. This study was supported in part within the framework of the State Contract "Studying the Possibilities of Developing Physico-Technical Processes Aimed at Creating Advanced Microwave Electronics." I.V.I. and A.V.S. gratefully acknowledge the support from the St. Petersburg Administration (Young Cand. Sci. Grants nos. PD03-1.2-119 and PD3-1.2-120) and the Scientific School of Academician Yu.N. Denisyuk (Grant no. NSh-98.2003.2).

REFERENCES

1. Y. P. Li and C. H. Henry, in *Optical Fiber Telecommunications* (Lucent Technology, 1997), Vol. IIIB, Chap. 8.
2. J. Hukriede, D. Runde, and D. Kip, J. Phys. D: Appl. Phys. **36**, R1 (2003).
3. M. P. Petrov, A. V. Shamray, V. M. Petrov, and J. J. Sanchez-Mondragon, Opt. Comm. **153**, 305 (1998).
4. D. Kip, Appl. Phys. B **67**, 131 (1998).
5. G. P. Agrawa and S Radic, IEEE Photonics Technol. Lett. **6**, 995 (1994).
6. V. M. Petrov, C. Caraboue, J. Petter, *et al.*, Appl. Phys. B **76**, 41 (2003).

Translated by P. Pozdeev

Technical Physics Letters, Vol. 30, No. 2, 2004, pp. 123–125. Translated from Pis'ma v Zhurnal Tekhnicheskoĭ Fiziki, Vol. 30, No. 3, 2004, pp. 82–88.

Microwave Switches Based on 4H-SiC *p–i–n* Diodes

A. V. Bludov, N. S. Boltovets, K. V. Vasilevskii, A. V. Zorenko, K. Zekentes, V. A. Krivutsa, T. V. Kritskaya, and A. A. Lebedev

"Orion" State Research Institute, Kiev, Ukraine

Ioffe Physicotechnical Institute, Russian Academy of Sciences, St. Petersburg, 194021 Russia

Institute of Electronic Structure and Lasers, Microelectronics Research Group, Foundation for Research and Technology–Hellas, Heraklion, Greece

Received April 30, 2003

Abstract—Problems pertaining to the modeling and development of a microwave modulator based on 4H-SiC *p–i–n* diodes are considered. The results of theoretical and experimental investigations of the microwave characteristics of 4H-SiC *p–i–n* diodes and the parameters of a microstrip modulator for a 1–10 GHz range based on these diodes are reported for the first time. In the diode switching schemes studied, the transmission losses amount to 0.8–8 dB and the decoupling is within –15 to –18 dB. The experimental characteristics of modulators are determined primarily by the parameters of diodes and agree well with the results of model calculations. © *2004 MAIK "Nauka/Interperiodica".*

Microwave modulators based on silicon *p–i–n* diodes enable switching times from a few nanoseconds to several milliseconds and can switch microwave powers from several hundred milliwatts to several kilowatts. However, the modulators with switching times within 1–10 ns provide for the commutation of microwave signals with powers not exceeding several hundred milliwatts. Moreover, the working temperatures of silicon *p–i–n* diodes do not exceed 125°C [1]. This is a limiting level of the device parameters that is determined by properties of the base material.

The unique combination of functional properties inherent in silicon carbide and the level achieved in the technology of p^+–n–n^+ diode structures based on this material make it possible to develop microwave switches with a response time of 2–10 ns capable of commutating signals with a power from several hundred watts to several kilowatts and operating at temperatures of up to 500°C [2, 3].

This paper reports the results of modeling of SiC-based *p–i–n* diodes, aimed at determining the requirements to parameters of the equivalent diode scheme. Based on these results, we have manufactured and characterized the prototypes of microwave modulators for a 1–10 GHz frequency range.

Using a diode model developed previously [4], we have analyzed the equivalent scheme of a microstrip modulator with parallel connection of the *p–i–n* diode into a transmission line. This equivalent scheme is depicted in Fig. 1. The modulator consists of two parts of a transmission line, TL_1 and TL_2, and a parallel 4H-SiC *p–i–n* diode. The bias voltage is applied via blocking capacitors C_3 and C_4. The model diode comprises a forward resistance of the *i* region (R_{Fi}), the *p–n* junction capacitance (C_i), the loss resistance (R_s), and the inductance of two leads (L_1 and L_2) connecting the upper electrode to the microstrip transmission line.

Figure 2 shows the results of modeling of the parameters of microwave diodes performed for frequencies of 1, 3, and 10 GHz in comparison to the measured data. The value of decoupling in the scheme under consideration is determined primarily by the forward resistance of the diode and is almost independent of the frequency. For providing a decoupling on the level of 20 and 25 dB, the forward resistance has to be 1.6 and 0.5 Ω, respectively. The switching losses depend on the frequency and are determined predominantly by the diode capacitance. Losses not exceeding 1 dB for frequencies of 10, 3, and 1 GHz can be obtained provided that the

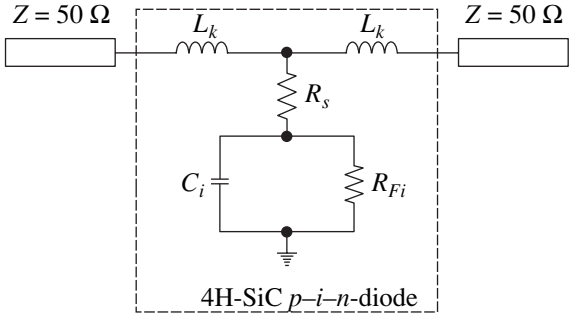

Fig. 1. An equivalent scheme of the microwave modulator based on a *p–i–n* diode. The transmission and blocking regimes are modeled by varying the values of R_{Fi} and C_i.

1063-7850/04/3002-0123$26.00 © 2004 MAIK "Nauka/Interperiodica"

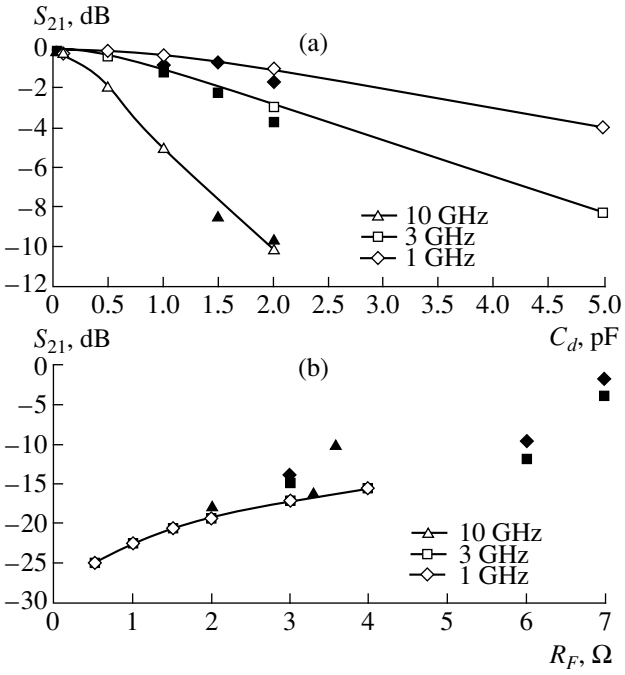

Fig. 2. The calculated (black symbols) and experimental (open symbols) plots of the (a) modulator losses versus diode capacitance C_i and (b) decoupling versus forward resistance R_F of the *p–i–n* diode.

diode capacitance is below 0.3, 1.0, and 2.0 pF, respectively.

The prototypes of switching diodes were 4H-SiC p^+–n–n^+ diodes with a mesa structure diameter of 60 μm [5]. The parameters of the equivalent scheme of a SiC-based diode were determined by measuring the forward resistance (R_F) as a function of the diode current at 3 and 10 GHz, the diode capacitance as a function of the inverse voltage, and the wiring capacitance at 10 GHz. The results of these measurements are presented in Figs. 3 and 4. As can be seen from these data, the microwave diode resistance at a forward current of 50 mA falls within 2–4 Ω; the resistance at 10 GHz is significantly smaller than that at 3 GHz; the diode capacitance at 1 MHz for a reverse bias of 0–40 V varies from 3 to 0.6 pF; and the inductance of leads at 10 GHz amounts to 0.6 nH. The reverse recovery time for the switching from forward current (10 mA) to reverse bias voltage (15 V) is 3 ns; the minority carrier lifetime determined from oscillograms of the diode switching in these regimes is 7–8 ns.

A prototype of the switching device comprised a segment of the microstrip line with a parallel diode. The prototype was connected to the measuring tract via a microstrip–coaxial line junction. Figure 5 shows the results of measurements of the switching device parameters at 1, 3, and 10 GHz. The maximum decoupling (18 dB) was observed at 10 GHz, while the minimum losses (0.8 dB) were obtained at 1 GHz. There is a correlation between the behavior of decoupling, forward resistance (R_F), and transmission losses as functions of the diode capacitance. The blocking losses in the region of saturation are satisfactorily correlated with the forward resistance of the diode (S_{21} versus R_F for the same forward current). Experimental values of the transmission losses and decoupling for the given diode capacitance and resistance (depending on the reverse voltage and direct current) are depicted in Fig. 2. The values of transmission losses show a quite acceptable agreement with the result of modeling of the microwave switch.

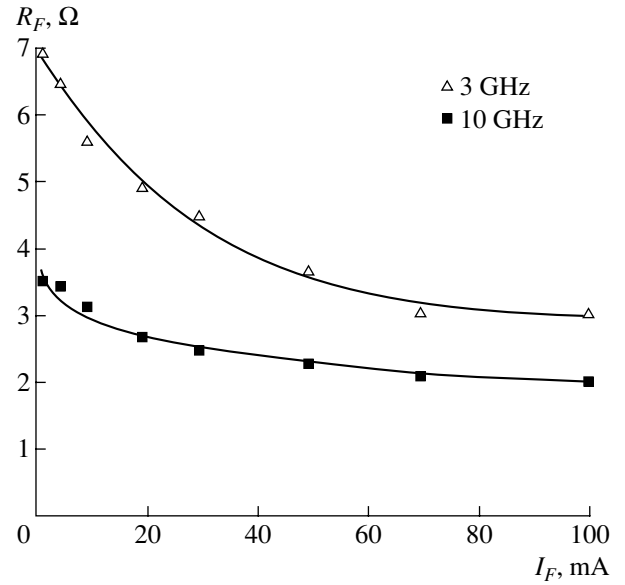

Fig. 3. Plots of the forward resistance R_F versus forward current for a 4H-SiC *p–i–n* diode at f = 10 and 3.0 GHz.

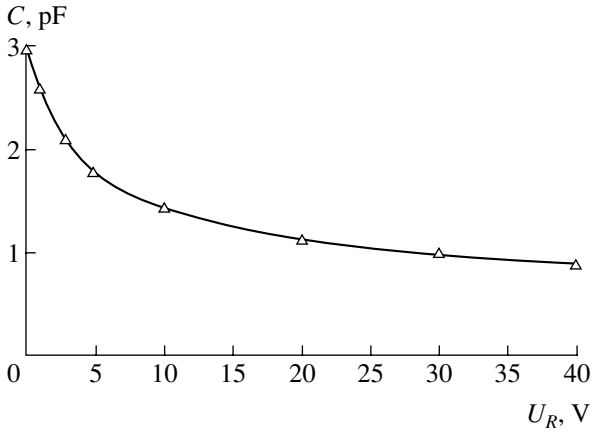

Fig. 4. A plot of the capacitance C versus reverse bias voltage U_R for a 4H-SiC *p–i–n* diode at f = 1 MHz.

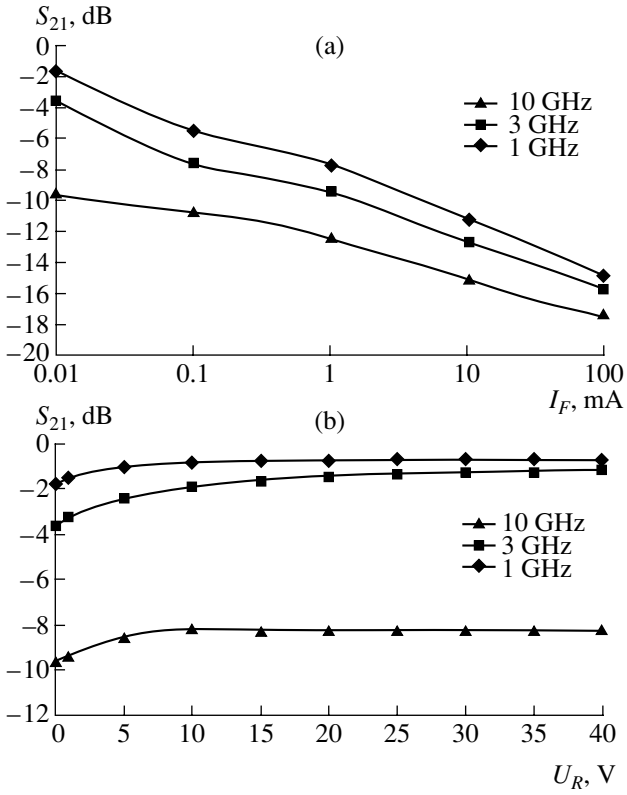

Fig. 5. Experimental plots of the (a) decoupling versus forward current I_F and (b) transmission losses versus reverse bias voltage U_R for various frequencies. Losses in the contacts and in the microstrip line with bias elements are below 1.5 dB.

The level of switching parameters is determined primarily by the diode characteristics. In order to increase the level of decoupling and decrease the transmission losses, so as to reach the levels acceptable for the commercial devices and fully realize the potential of SiC-based microwave devices, it is necessary to reduce the forward-biased diode resistance to 0.5–1.0 Ω (in the working bias range) and the reverse-biased diode capacitance to 0.1–0.2 pF (at a frequency of 10 GHz), 0.5–1.0 pF (3 GHz), and 1.5–2 pF (1 GHz).

Conclusions. We have demonstrated the possibility of creating a microwave modulator for the 1–10 GHz range based on 4H-SiC p^+–n–n^+ diodes. The experimental values of the transmission losses (0.8 dB at 1 GHz) and decoupling (–18 dB at 10 GHz) are satisfactorily described by the proposed diode model and are determined primarily by the level of the forward diode resistance (R_F) at a given diode capacitance.

Acknowledgments. This study was supported by the INTAS Foundation (grant no. 01-603) and the NATO Science for Peace Program (grant no. SfP-978 011).

REFERENCES

1. *A Handbook on Semiconductor Devices: Microwave Diodes*, Ed. by B. A. Nalivaĭko (Rasko, Tomsk, 1992).
2. A. A. Lebedev and V. E. Chelnokov, Fiz. Tekh. Poluprovodn. (St. Petersburg) **33**, 1096 (1999) [Semiconductors **33**, 999 (1999)].
3. R. J. Trew *et al.*, Proc. IEEE **79**, 598 (1991).
4. *Advanced Design System 2002: A Set of Program Codes* (Agilent Technologies, 2002).
5. K. Vasilevskii, K. Zekentes, G. Constantinidis, and A. Strel'chuk, Solid-State Electron. **44**, 1173 (2000).

Translated by P. Pozdeev

Technical Physics Letters, Vol. 30, No. 2, 2004, pp. 126–128. Translated from Pis'ma v Zhurnal Tekhnicheskoĭ Fiziki, Vol. 30, No. 3, 2004, pp. 89–94.

Misfit Dislocation Loop Nucleation at a Quantum Dot

A. L. Kolesnikova[a,*] and A. E. Romanov[b,]**

[a] *Institute of Problems of Mechanical Engineering, Russian Academy of Sciences, St. Petersburg, 199178 Russia*

[b] *Ioffe Physicotechnical Institute, Russian Academy of Sciences, St. Petersburg, 194021 Russia*

*e-mail: * ankolesnikova@yandex.ru; ** aer@mail.ioffe.ru*

Received July 31, 2003

Abstract—An energy criterion for the nucleation of a circular prismatic misfit dislocation loop in a spheroidal inclusion modeling a quantum dot is considered. The critical radius of the inclusion, for which the misfit dislocation loop can nucleate, is studied as a function of the lattice misfit between the inclusion and the matrix. © *2004 MAIK "Nauka/Interperiodica".*

The nucleation of misfit dislocations (MDs) is the dominating mechanism of relaxation of the elastic stresses arising in thin heteroepitaxial films as a result of the misfit between crystal lattices of the film and substrate [1]. As is well known, MDs nucleate when the epitaxial film thickness h exceeds a certain critical value h_c that depends on the misfit strain ε_m. An analogous phenomenon has to take place in the case of elastically strained quantum dots (QDs).

This study was aimed at establishing the conditions of MD nucleation in a small strained inclusion modeling a QD. This simple problem was not formulated and solved until now, while a number of models describing the nucleation of MDs [2, 3] were suggested for the coherent islands on substrates, that is, for the stage of QD nucleation. However, these models were based on two-dimensional problems and, hence, were rather approximate.

Elastic strains and stresses in QDs lead to significant changes in their properties. In particular, homogeneous elastic straining changes the bandgap width [4], while inhomogeneous elastic fields of MDs can influence the optical properties of materials with QDs [5].

Let us consider a QD model representing a spheroidal inclusion of radius R_{sp} with a given isotropic plastic dilatation embedded into a matrix material (Fig. 1). Mathematically, the dilatation can be described using a plastic distortion tensor [6]

$$\beta^*_{xx} = \beta^*_{yy} = \beta^*_{zz} = \varepsilon_m \delta(\Omega_{sp}), \qquad (1)$$

where $\varepsilon_m = (a_{sp} - a_M)/a_M$ is the parameter of misfit between the inclusion and the matrix; a_{sp} and a_M are the lattice parameters of the spheroid and matrix, respectively; and $\delta(\Omega_{sp})$ is the Dirac delta function for the region Ω_{sp} occupied by the spheroid:

$$\delta(\Omega_{sp}) = \begin{cases} 1, & \mathbf{r} \in \Omega_{sp} \\ 0, & \mathbf{r} \notin \Omega_{sp} \end{cases}.$$

The sign of ε_m reflects the character of dilatation: $\varepsilon_m > 0$ corresponds to expansion and $\varepsilon_m < 0$ implies contraction.

Equations for the elastic stresses and the energy of an inclusion with distortion (1) are well known and the solution can be expressed in elementary functions [6, 7]. The stresses inside the inclusion are constant:

$$\sigma^{(in)}_{rr} = \sigma^{(in)}_{\varphi\varphi} = \sigma^{(in)}_{zz} = -\frac{4G\varepsilon_m(1+\nu)}{3(1-\nu)}, \qquad (2)$$

where (r, φ, z) are cylindrical coordinates (Fig. 1), G is the shear modulus, and ν is the Poisson coefficient.

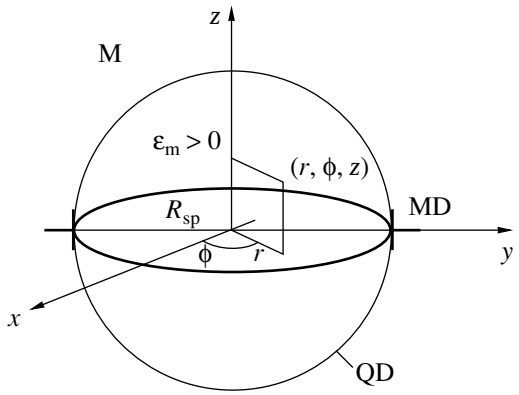

Fig. 1. The model of a quantum dot (QD) with misfit dislocation (MD); M is the matrix; ε_m is the lattice misfit parameter.

The elastic energy of the inclusion is given by the formula

$$E_{sp} = \frac{8\pi(1+\nu)}{3(1-\nu)} G\varepsilon_m^2 R_{sp}^3. \quad (3)$$

Formulas (2) and (3) were obtained with neglect of the difference between the elastic properties of inclusion and matrix.

It would be reasonable to assume that the elastic energy of the inclusion tends to decrease by means of nucleation of a circular prismatic misfit dislocation loop (Fig. 1) situated on the surface of the spheroid. Since the energy of the inclusion with an MD loop has to be smaller than the initial value, we obtain the following energy criterion for the MD loop nucleation:

$$E_{sp} \geq E_{sp} + E_{loop} + W, \quad (4)$$

where E_{loop} is the MD loop energy and W is the energy of interaction between the loop and spheroid.

The self elastic energy of a prismatic MD loop with the Burgers vector b and radius a, such that $a \gg b$, is described by the formula [8]

$$E_{loop} \approx \frac{Gb^2 a}{2(1-\nu)}\left(\ln\frac{8\alpha a}{b} - 2\right), \quad (5)$$

where α is the parameter taking into account the contribution of the dislocation core (for nonmetals, $\alpha \approx 4$ [9]).

In the general case, the energy of interaction between two defects, I and II, is determined as [6]

$$W = -\int_{\Omega_I} \beta_{ij}^{*I} \sigma_{ij}^{II} dV = -\int_{\Omega_{II}} \beta_{ij}^{*II} \sigma_{ij}^{I} dV, \quad (6)$$

where Ω_I and Ω_{II} are the regions occupied by defects I and II, respectively; β_{ij}^{*I} and β_{ij}^{*II} are the plastic distortions of these defects; and σ_{ij}^{I} and σ_{ij}^{II} are the elastic stresses created by the defects.

The plastic distortion of a prismatic loop situated in the $X0Y$ plane (Fig. 1) can be expressed as [6]

$$\beta_{zz}^{*loop} = \pm bH\left(1 - \frac{r}{a}\right)\delta(z), \quad (7)$$

where the upper and lower signs correspond to the interstitial and vacancy loops, respectively (Fig. 1 shows the latter case), and $\delta(z)$ is the one-dimensional Dirac delta function.

Using relations (2), (4)–(7), we obtain the following energy criterion for the MD loop nucleation at the boundary between a spheroidal inclusion and the matrix:

$$\frac{Gb^2 R_{sp}}{2(1-\nu)}\left(\ln\frac{32R_{sp}}{b} - 2\right) - \frac{4\pi Gb\varepsilon_m(1+\nu)R_{sp}^2}{3(1-\nu)} \leq 0. \quad (8)$$

This expression takes into account that the inclusion with expansion ($\varepsilon_m > 0$) corresponds to the MD vacancy loop with the radius $a = R_{sp}$, for which the energy gain of the "inclusion–MD loop" system is maximum.

A relation for the critical radius R_c of the inclusion corresponding to nucleation of the MD loop can be written as

$$R_c = \frac{3b}{8\pi(1+\nu)\varepsilon_m}\left(\ln\frac{1.08\alpha R_c}{b}\right). \quad (9)$$

For comparison, consider the relation for the critical film thickness h_c at which an edge MD is nucleated at a heteroboundary (with the Burgers vector parallel to this boundary) [1]:

$$h_c = \frac{b}{8\pi(1+\nu)\varepsilon_m}\left(\ln\frac{\alpha h_c}{b}\right). \quad (10)$$

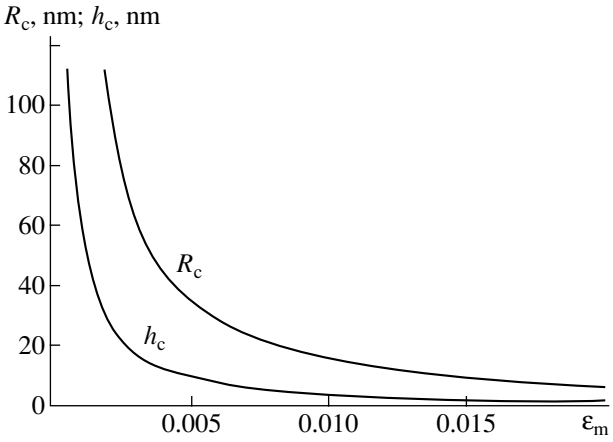

Fig. 2. Plots of the critical radius of inclusion R_c and the critical film thickness versus the lattice misfit parameter ε_m ($\nu = 0.3$; $\alpha = 4$; $b = 0.3$ nm).

Figure 2 shows a plot of the critical radius R_c determined by formula (9) as a function of the misfit parameter ε_m. We also plot the function $h_c(\varepsilon_m)$ according to formula (10) for the simplest case of MD in a film. As can be seen, the critical radius of inclusion is 3.5–4 times the critical film thickness for the same value of the misfit parameter ε_m.

It should be noted that the MD loops can be formed according to either diffusion or deformation mechanisms. An alternative mechanism of decrease in the energy of an inclusion with given plastic dilatation con-

sists in the nucleation of an MD loop in the matrix outside the inclusion [10].

In conclusion, we obtained an expression for the critical radius of an inclusion at which the MD loop nucleation is energetically favorable and studied this value as a function of the misfit between the inclusion and matrix lattices.

REFERENCES

1. R. Beanland, D. J. Dunstan, and P. J. Goodhew, Adv. Phys. **45** (2), 87 (1996).
2. E. Pehlke, N. Moll, A. Kley, and M. Scheffler, Appl. Phys. A **65**, 525 (1997).
3. K. Tillmann and A. Forster, Thin Solid Films **368**, 93 (2000).
4. O. V. Konstantinov, E. Yu. Kotel'nikov, A. V. Matveentsev, and A. E. Romanov, Pis'ma Zh. Tekh. Fiz. **27** (16), 40 (2001) [Tech. Phys. Lett. **27**, 683 (2001)].
5. X. Chen, Y. Lou, A. C. Samia, and C. Burda, Nano Letters **3**, 799 (2003).
6. T. Mura, *Micromechanics of Defects in Solids* (Nijhoff, Boston, 1987), p. 587.
7. C. Teodosiu, *Elastic Models of Crystal Defects* (Springer-Verlag, Berlin, 1982; Mir, Moscow, 1985).
8. J. Dundurs and N. J. Salamon, J. Phys. C **50**, 125 (1972).
9. J. P. Hirth and J. Lothe, *Theory of Dislocations* (McGraw-Hill, New York, 1967; Atomizdat, Moscow, 1972); X. Chen, Y. Lou, A. C. Samia, and C. Burda, Nano Letters **3**, 799 (2003).
10. N. A. Bert, A. L. Kolesnikova, A. E. Romanov, and V. V. Chaldyshev, Fiz. Tverd. Tela (St. Petersburg) **44**, 2139 (2002) [Phys. Solid State **44**, 2240 (2002)].

Translated by P. Pozdeev

Technical Physics Letters, Vol. 30, No. 2, 2004, pp. 129–130. Translated from Pis'ma v Zhurnal Tekhnicheskoĭ Fiziki, Vol. 30, No. 4, 2004, pp. 1–5.

The Binding Energy of Molecules in Thin Fullerene Films

M. A. Khodorkovskiĭ*, S. V. Murashov, T. O. Artamonova, A. L. Shakhmin, and A. A. Belyaeva

State Scientific Center of Applied Chemistry, St. Petersburg, Russia

** e-mail: mkhodorkovskii@rscac.spb.ru*

Received July 18, 2003

Abstract—Thin fullerene films formed using the methods of pulsed supersonic molecular beam (SMB) deposition and thermal deposition (TD) in vacuum were studied by thermodesorption (TDS) mass spectroscopy. The TDS spectra of SMB films show a significantly higher temperature of desorption (827.8 K) of fullerene molecules as compared to the value (583 K) observed in the spectra of TD films. It is suggested that the higher binding energies of fullerene molecules in the former films are explained by the formation of polymer structures due to heating in the course of TDS measurements. © *2004 MAIK "Nauka/Interperiodica".*

Previously [1], we proposed a new method for obtaining films using a supersonic molecular beam of an inert gas enriched with molecules of a substance to be deposited. Recently, the phase composition of fullerene films obtained by the supersonic molecular beam (SMB) deposition method and modified by laser radiation was studied by Raman spectroscopy [2]. It was found that, depending on the laser radiation dose, SMB films acquire the same polymer structures as those observed in bulk fullerene samples formed under conditions of high pressures and temperatures [3].

These structures ensure transfer of the supplied laser energy over the whole polymer ensemble, so that the molecular structure of the fullerene framework is retained in the SMB films until their complete evaporation. It should be noted that high "laser strength" is characteristic only of the SMB films, while the films obtained by the traditional method of thermal deposition (TD) in vacuum exhibit degradation even under the action of a low-power laser radiation [2]. It was suggested [2] that the susceptibility of SMB films to polymerization could be related to the higher density of these films and to the significantly greater energy of binding between fullerene molecules.

In this context, we have studied the binding energy of fullerene molecules in various films by the method of thermodesorption (TDS) mass spectroscopy.

The TDS experiments consisted in measuring the concentration of fullerene molecules in the gas phase depending on the temperature of a film sample. For this purpose, fullerene films deposited onto single crystal molybdenum or nickel substrates were heated (at a rate of 10 K/s) in a vacuum chamber and the concentration of C_{60} molecules was measured using a quadrupole mass spectrometer tuned to 720 amu.

The results of TDS measurements for the SMB and TD films are presented in the figure. As can be seen from these data, the peak of desorption of fullerene molecules from the films obtained by thermal deposition takes place at T_{max} = 584 K. The same desorption temperature was reported in [4] for films obtained by deposition of fullerene vapor from a Knudsen cell onto a preliminarily heated (1200 K) surface of highly oriented pyrolytic graphite (HOPG). The activation energy E_d of C_{60} desorption from the first monolayer on HOPG was 1.69 eV, which corresponds (by the order of magnitude) to weak van der Waals interactions between molecules.

At the same time, the maximum rate of fullerene desorption from SMB films is observed at a temperature T_{max} above 800 K (see figure), which indicates that the binding energy of fullerene molecules in these films is significantly higher than in the TD films. Analogous

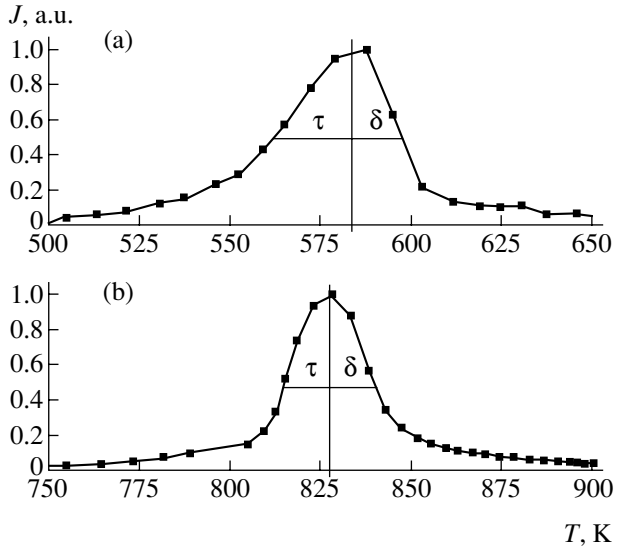

TDS spectra of fullerene films obtained by (a) thermal deposition and (b) supersonic molecular beam deposition methods.

1063-7850/04/3002-0129$26.00 © 2004 MAIK "Nauka/Interperiodica"

values of the temperature of fullerene desorption were observed for fullerenes in films on the surface of a high-temperature rigid-chain polyimide and in a compound with this polymer [5]. In the latter case, the temperature of fullerene desorption also exceeded 800 K. Based on a comparison of the thermodesorption states of C_{60} on the surface and in the bulk of polyimide [5], it was suggested that the bonds of C_{60} with macromolecules on the surface of a formed polyimide film are not as strong as the bonds of C_{60} introduced into an initial matrix before application onto a metal substrate and the polyimide film formation.

Approximately equal values of the maximum rate of fullerene desorption from polyimide and SMB fullerene films probably reflect a similar nature of the intermolecular forces in these cases, although it was pointed out [5] that the desorption of fullerene from polyimide films could also be related to decomposition of the polymer matrix at temperatures above 800 K.

According to the results obtained previously [2], fullerene molecules in the SMB films initially occur in a nonpolymerized (pristine C_{60}) state and it is only the laser action that gives rise to a fast polymerization process, in which a significant role is played by the thermal factor. Since there is evidence (e.g., some features in the electron energy loss spectra [6]) that SMB films possess increased density, rapid heating of such films can lead to the process of polymer structure formation analogous to that taking place under the conditions of high pressures and temperatures. In SMB films, the stages of contraction (dense fullerene film formation) and heating are separated in time.

A comparison of the TDS peaks of SMB and TD films reveals a significant difference in their shapes (see figure). In the TDS spectra of our samples, the ratio of halfwidths of the low- (τ) and high-temperature (δ) parts of the peak is 1.84 and 1.08 for the TD and SMB films, respectively. As is known, the shape of the TDS peak depends on the order of desorption [7] and can be used for determining the order of this reaction. The second-order desorption peak is symmetric ($\tau \approx \delta$), while the first-order peak is asymmetric ($\tau > \delta$). In the case of SMB films, the areas of the low- and high-temperature parts of the peak are almost equal, which suggests a reaction of the second order. In contrast, the asymmetric spectrum of the TD film is indicative of the first-order reaction.

Using the experimental values of δ and T_{max}, we have calculated the binding energy (more precisely, the desorption energy E_d) of adsorbed fullerene molecules using the Redhead formula [7]

$$E_d = \chi R T_{max}^2/\delta,$$

where χ is the reaction order (1 or 2 for the first- and second-order processes, respectively), T_{max} is the TDS peak temperature (827.8 and 583 K for the SMB and TD films, respectively), and δ is the width at half-maximum of the high-temperature part of the TDS peak (12 and 15.3 K for the SMB and TD films, respectively). The desorption activation energy calculated using the experimental data for the TD films is E_d = 1.91 eV, which is close to the energy of desorption for fullerene molecules on the surface carbons [4]. At the same time, the SMB films are characterized by a significantly higher value of E_d = 9.8 eV. This anomalous activation energy is close to the binding energy of fullerene molecules in a polymer structure, from which the molecules are desorbed via a second-order reaction.

To summarize, we have demonstrated that the energy of desorption of fullerene molecules from SMB films is significantly higher than the value for the films obtained by the standard method of thermal deposition in vacuum. The unusual behavior of SMB films can be related to their polymerization due to heating in the course of TDS measurements.

Acknowledgments. The authors are grateful to E.E.E. Campbell for the methodological help in conducting the experiment.

This work was supported by the Russian Foundation for Basic Research (project nos. 01-03-33162 and 01-02-16782) and by the Federal Scientific-Technological Program "Fullerenes and Atomic Clusters."

REFERENCES

1. M. A. Khodorkovskiĭ, A. L. Shakhmin, S. V. Murashov, *et al.*, Pis'ma Zh. Tekh. Fiz. **24** (10), 20 (1998) [Tech. Phys. Lett. **24**, 379 (1998)].
2. M. A. Khodorkovskiĭ, S. V. Murashov, T. O. Artamonova, *et al.*, Zh. Tekh. Fiz. **74**, 118 (2004) [Tech. Phys. **49**, 258 (2004)].
3. A. M. Rao, P. C. Eklund, J.-L. Hodeau, *et al.*, Phys. Rev. B **55**, 4766 (1997).
4. H. Ulbricht, G. Moos, and T. Hertel, Phys. Rev. Lett. **90**, 095501 (2003).
5. A. O. Pozdnyakov, B. M. Ginzburg, O. F. Pozdnyakov, *et al.*, Pis'ma Zh. Tekh. Fiz. **26** (17), 46 (2000) [Tech. Phys. Lett. **26**, 775 (2000)].
6. A. L. Shakhmin, A. M. Khodorkovskiĭ, S. V. Murashov, *et al.*, Pis'ma Zh. Tekh. Fiz. **27** (3), 1 (2001) [Tech. Phys. Lett. **27**, 87 (2001)].
7. D. P. Woodruff and T. A. Delchar, *Modern Techniques of Surface Science*, 2nd ed. (Cambridge University Press, Cambridge, 1994; Mir, Moscow, 1989).

Translated by P. Pozdeev

Technical Physics Letters, Vol. 30, No. 2, 2004, pp. 131–134. Translated from Pis'ma v Zhurnal Tekhnicheskoĭ Fiziki, Vol. 30, No. 4, 2004, pp. 6–14.

The Modulation Instability of Dispersed Electromagnetic Waves in the Josephson Junction with Nonlocal Interaction

A. I. Lomtev

Donetsk Physicotechnical Institute, National Academy of Sciences of Ukraine, Donetsk, Ukraine
e-mail: lomtev@kinetic.ac.donetsk.ua

Received August 18, 2003

Abstract—The modulation instability of dispersed electromagnetic waves propagating in the Josephson junction between massive superconductors has been studied. A dispersion equation for the increment of small perturbations of the wave amplitude is obtained. It is shown that the spatial nonlocality produces a stabilizing influence with respect to the development of modulation instability in a long-wavelength region of the perturbation wavevectors $0 \le Q \le Q_{B1}(\mathbf{k})$. The region of modulation instability $Q_{B1}(\mathbf{k}) < Q < Q_{B2}(\mathbf{k}, A, L)$ can be controlled by the dispersion parameter—the wavevector $\mathbf{k}$ (or the frequency $\omega(\mathbf{k})$) of the carrier wave in the linear approximation. © *2004 MAIK "Nauka/Interperiodica".*

Numerous phenomena related to the instability of waves in various nonlinear systems and media still receive much attention [1, 2]. As is known, contraction of a nonlinear wave can take place both across and along the direction of wave propagation. Examples are offered by the self-focusing of light predicted by Askar'yan [3, 4] and by the development of instabilities in the form of wave separation into packets and the self-contraction of wave packets. The latter type of modulation instability was originally studied by Lighthill [5].

The modulation instability of electromagnetic waves excited in distributed Josephson junctions is described in terms of the instability of solutions of the corresponding sine-Gordon equations. In many cases, the modulation instability has to be studied using spatially nonlocal modifications of the sine-Gordon equation [6, 7]. The spatially nonlocal character of equations for the phase difference arises due to the nonlocal coupling of magnetic fields at the interface and in the bulk of a superconductor. This is a universal reason for the spatial nonlocality to arise in electrodynamics of the Josephson junctions.

Within the framework of electrodynamics of the spatially nonlocal Josephson junction between massive superconductors with a thickness d much greater than the London penetration depth λ, the modulation instability of electromagnetic waves was originally studied by Aliev *et al.* [6]. The analysis was based on a system of approximate equations for perturbations of the complex amplitude (real perturbations of the amplitude and phase), derived using an expansion of the spectrum of dispersed waves in the linear approximation with respect to small perturbations of the wave frequency and the wavevector. It was shown that the growth of small perturbations in the wave amplitude and phase corresponds to the development of modulation instability of an electromagnetic wave with a finite constant amplitude, a nonlinear frequency shift, and a dispersion law in the linear approximation. It was established that the spatial nonlocality produces a stabilizing influence with respect to the development of modulation instability in the intermediate and short-wavelength regions of the perturbation wavevectors.

Abdullaev [8] studied the modulation instability of a homogeneous (non-dispersed) plane nonlinear electromagnetic wave with the Josephson frequency, a finite amplitude, and a nonlinear frequency shift in the Josephson junction between massive superconductors with $d \gg \lambda$. The instability was related to the buildup of only small amplitude perturbations and led to separation of the wave into wave packets. In the systems studied in both papers [6, 8] cited above, the modulation instability for perturbations with the wavevectors $\mathbf{Q}$ takes place in the region of $0 < Q < Q_B$, where $\mathbf{Q}_B$ is a certain boundary wavevector. Thus, the region of long-wavelength perturbations $\mathbf{Q} \longrightarrow 0$ was always the region of instability.

As will be shown below, the spatial nonlocality in the equations of electrodynamics for the waves with dispersion in the Josephson junction produces a stabilizing influence with respect to the development of modulation instability caused only by small perturbations with wavevectors in the long-wavelength region $0 \le Q \le Q_{B1}(\mathbf{k})$.

In the Josephson junction between massive superconductors with thicknesses $d \gg \lambda$, the dynamics of the phase difference $\varphi(x, t)$ in a dissipationless limit is

described by a nonlinear sine-Gordon equation with spatial nonlocality [6, 7],

$$\frac{1}{\omega_J^2}\frac{\partial^2\varphi(x,t)}{\partial t^2} + \sin\varphi(x,t) = \frac{\lambda_J^2}{\pi\lambda}\int_{-\infty}^{\infty} K_0\left(\frac{|x-x'|}{\lambda}\right)\frac{\partial^2\varphi(x',t)}{\partial x'^2}dx'. \quad (1)$$

Here, ω_J is the Josephson frequency, λ_J is the Josephson length, and $K_0(x)$ is the zero-order Macdonald function. For $\lambda \longrightarrow 0$, this equation converts into the well-known sine-Gordon equation [9, 10].

In the linear approximation, whereby $\sin\varphi(x, t) \approx \varphi(x, t)$, Eq. (1) describes dispersed small-amplitude electromagnetic waves propagating along the junction,

$$\varphi(x,t) = \varphi_0\exp[i(\mathbf{k}x - \omega t)], \quad |\varphi_0| \ll 1, \quad (2)$$

with the wavevector $\mathbf{k}$ and frequency ω obeying the dispersion relation

$$\omega^2(\mathbf{k}) = \omega_J^2 + v_S^2\mathbf{k}^2/(1+\lambda^2\mathbf{k}^2)^{1/2}, \quad (3)$$

where $v_S = \lambda_J\omega_J$ is the Swihart wavelength. We will consider the evolution of nonlinear dispersed electromagnetic waves of small but finite amplitude in the Josephson junction. The phase difference $\varphi(x, t)$ can be written in the following form:

$$\varphi(x,t) = u(x,t)\exp\{i[\mathbf{k}x - \omega(\mathbf{k})t]\} + u^*(x,t)\exp\{-i[\mathbf{k}x - \omega(\mathbf{k})t]\}, \quad |u(x,t)| \ll 1. \quad (4)$$

Let us use the approximation $\sin\varphi(x, t) \approx \varphi(x, t) - \varphi^3(x, t)/3!$ [11], retain only nonlinear terms of the lowest order for the main carrier harmonic in Eq. (1), and restrict the consideration to the approximation of amplitude $u(x, t)$ slowly varying with time, for which $|\partial^2 u(x, t)/\partial t^2| \ll 2\omega(\mathbf{k})|\partial u(x, t)/\partial t|$. Substituting expression (4) into Eq. (1), we obtain the following equation for the amplitude:

$$i2\omega(\mathbf{k})\frac{\partial u(x,t)}{\partial t} + \left[\omega^2(\mathbf{k}) - \omega_J^2 + \frac{\omega_J^2}{2}|u(x,t)|^2\right]u(x,t) + \frac{v_S^2}{\pi\lambda}\int_{-\infty}^{\infty} K_0\left(\frac{|x-x'|}{\lambda}\right)\left[\frac{\partial^2 u(x',t)}{\partial x'^2} + i2\mathbf{k}\frac{\partial u(x',t)}{\partial x'} - \mathbf{k}^2 u(x',t)\right]\exp[-i\mathbf{k}(x-x')]dx' = 0. \quad (5)$$

This nonlinear nonlocal equation has an exact solution in the form of a plane homogeneous nonlinear wave with a constant amplitude A and a nonlinear frequency shift:

$$u_0(t) = A\exp[i\omega_J^2A^2t/4\omega(\mathbf{k})], \quad A \ll 1. \quad (6)$$

Let us study the stability of this solution. The character of decay of the plane wave of type (6) can be judged by the behavior of small perturbations. Consider a wave with a small perturbation in the amplitude:

$$u(x,t) = [A + \psi(x,t)]\exp[i\omega_J^2A^2t/4\omega(\mathbf{k})], \quad |\psi(x,t)| \ll A. \quad (7)$$

Using Eq. (5), we obtain a linear equation for the small perturbation $\psi(x, t)$:

$$i\frac{2\omega(\mathbf{k})}{\omega_J^2}\frac{\partial\psi(x,t)}{\partial t} + \left[\frac{\omega^2(\mathbf{k})}{\omega_J^2} - 1\right]\psi(x,t) + \frac{A^2}{2}[\psi(x,t) + \psi^*(x,t)] + \frac{\lambda_J^2}{\pi\lambda}\int_{-\infty}^{\infty} K_0\left(\frac{|x-x'|}{\lambda}\right)\left[\frac{\partial^2\psi(x',t)}{\partial x'^2} + i2\mathbf{k}\frac{\partial\psi(x',t)}{\partial x'} - \mathbf{k}^2\psi(x',t)\right]\exp[-i\mathbf{k}(x-x')]dx' = 0. \quad (8)$$

Setting $\psi(x, t) = v(x, t) + iw(x, t)$, we arrive at a system of two equations for the real and imaginary parts of the perturbation propagating along the Josephson junction. For perturbations of the type

$$v(x,t) = V(\mathbf{Q},\Omega)\exp[i(\mathbf{Q}x - \Omega t)], \quad w(x,t) = W(\mathbf{Q},\Omega)\exp[i(\mathbf{Q}x - \Omega t)] \quad (9)$$

(arbitrary perturbations can be represented as superpositions of such components) with the wavevector $\mathbf{Q}$ and a frequency Ω, these equations give the following dispersion relation for $\Omega = \Omega(\mathbf{Q})$:

$$\frac{\Omega(\mathbf{Q})}{\omega_J} = \frac{\omega_J\lambda_J^2\mathbf{k}\mathbf{Q}}{\omega(\mathbf{k})\sqrt{1+\lambda^2(\mathbf{k}+\mathbf{Q})^2}} \pm \frac{\omega_J}{2\omega(\mathbf{k})}\left[\frac{\omega^2(\mathbf{k}+\mathbf{Q})}{\omega_J^2} - \frac{\omega^2(\mathbf{k})}{\omega_J^2} - \frac{2\lambda_J^2\mathbf{k}\mathbf{Q}}{\sqrt{1+\lambda^2(\mathbf{k}+\mathbf{Q})^2}}\right]^{1/2} \times\left[\frac{\omega^2(\mathbf{k}+\mathbf{Q})}{\omega_J^2} - \frac{\omega^2(\mathbf{k})}{\omega_J^2} - \frac{2\lambda_J^2\mathbf{k}\mathbf{Q}}{\sqrt{1+\lambda^2(\mathbf{k}+\mathbf{Q})^2}} - A^2\right]^{1/2}, \quad (10)$$

where $\omega(\mathbf{k})$ is given by relation (3). This dispersion equation determines the growth of the wave amplitude perturbation with an increment of $\gamma(\mathbf{Q}) = \mathrm{Im}\Omega(\mathbf{Q})$.

According to Eq. (10), which always has a solution of the type $\Omega(\mathbf{Q}) = \mathrm{Re}\Omega(\mathbf{Q}) + i\mathrm{Im}\Omega(\mathbf{Q})$ with a positive imaginary part, small amplitude perturbations (9) grow with the time as described by the increment $\gamma(\mathbf{Q})$. The buildup of small amplitude perturbations corresponds to the development of a modulation instability of the wave with a constant amplitude A, a nonlinear phase shift (6), and a dispersion law in the linear approximation (3). Note that the increment $\gamma(\mathbf{Q})$ is determined according to relation (10) directly by the wave spectrum $\omega(\mathbf{k})$ in the linear approximation (3) rather than by the derivative $\partial^2\omega(\mathbf{k})/\partial\mathbf{k}^2$ as in [6]. It should also be noted that, in the absence of wave dispersion, Eq. (10) with $\mathbf{k} = 0$ gives all the results reported in [8].

In the local limit of $\lambda_J^2/\lambda \gg \lambda_J \gg \lambda$, the spatial nonlocality in Eq. (1) for the phase difference is insignificant (the transition $\lambda \longrightarrow 0$ yields the usual sine-Gordon equation). In this case, dispersion relation (10) acquires the form

$$\frac{\Omega(\mathbf{Q})}{\omega_J} = \frac{1}{\sqrt{1+\lambda_J^2\mathbf{k}^2}}\left[\lambda_J^2\mathbf{k}\mathbf{Q} \pm i\frac{\lambda_J\mathbf{Q}}{2}\left(A^2 - \lambda_J^2\mathbf{Q}^2\right)^{1/2}\right], \quad (11)$$

from which it follows that waves with arbitrary wavevectors $\mathbf{k}$ are unstable with respect to small amplitude perturbations with the wavevectors $0 < Q < Q_B = A/\lambda_J$. The maximum increment of the perturbation buildup is determined by the relation $\gamma_{\max}(\mathbf{Q}_m)/\omega_J = A^2/4(1 + \lambda_J^2\mathbf{k}^2)^{1/2}$ and is reached for the perturbation wavevector $\mathbf{Q} = \mathbf{Q}_m = A/\sqrt{2}\,\lambda_J$.

In the limit of strong spatial nonlocality, for a finite depth λ of the field penetration into the superconductor obeying the conditions $\lambda_J^2/\lambda \ll \lambda_J \ll \lambda$ and $\mathbf{k}\lambda \gg 1$, dispersion relation (10) acquires the following form:

$$\frac{\Omega(\mathbf{Q})}{\omega_J} = \frac{1}{\sqrt{1+\lambda_J^2\mathbf{k}/\lambda}}\left\{\frac{\lambda_J^2\mathbf{k}\mathbf{Q}}{\lambda(\mathbf{k}+\mathbf{Q})} \pm \frac{1}{2}\left[\frac{\lambda_J^2\mathbf{Q}(\mathbf{Q}-\mathbf{k})}{\lambda(\mathbf{Q}+\mathbf{k})}\right]^{1/2}\left[\frac{\lambda_J^2\mathbf{Q}(\mathbf{Q}-\mathbf{k})}{\lambda(\mathbf{Q}+\mathbf{k})} - A^2\right]^{1/2}\right\}. \quad (12)$$

According to this, for a wave with an arbitrary wavevector $\mathbf{k}$ in the Josephson junction, there are two regions of stability with respect to the buildup of small amplitude perturbations with wavevectors $\mathbf{Q}$:

$$0 \le Q \le Q_{B1}(\mathbf{k}) \quad \text{and} \quad Q \ge Q_{B2}(\mathbf{k}, A, L),$$

where $L = (\lambda_J/\lambda)^2$, $\mathbf{Q}_{B1}(\mathbf{k}) = \mathbf{k}$, and

$$\mathbf{Q}_{B2}(\mathbf{k}, A, L) = \frac{1}{2}(\mathbf{k} + A^2\lambda/\lambda_J^2) + \sqrt{\frac{1}{4}(\mathbf{k} + A^2\lambda/\lambda_J^2)^2 + \mathbf{k}A^2\lambda/\lambda_J^2}.$$

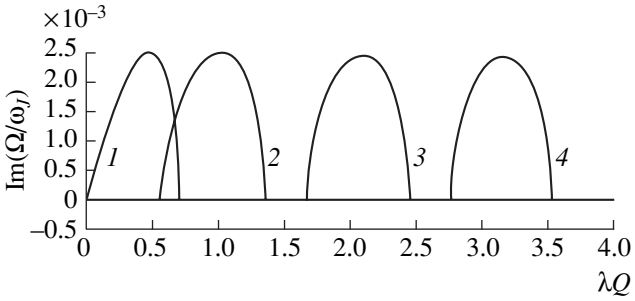

The regions of modulation instability for a plane nonlinear electromagnetic wave (6) with a constant amplitude $A = 10^{-1}$, the parameter $L = 0.25 \times 10^{-1}$, and various values of the reduced wavevector $k\lambda = 0$ (*1*), 1 (*2*), 2 (*3*), and 3 (*4*).

For the perturbations with wavevectors $\mathbf{Q}$ in the region $Q_{B1}(\mathbf{k}) < Q < Q_{B2}(\mathbf{k}, A, L)$, the plane nonlinear electromagnetic wave is subject to modulation instability. The maximum increment of the perturbation buildup is determined by the relation $\gamma_{\max}(\mathbf{Q}_m)/\omega_J = A^2/4(1 + \lambda_J^2\mathbf{k}/\lambda)^{1/2}$ and is reached for the perturbation wavevector

$$\mathbf{Q} = \mathbf{Q}_m = \frac{1}{2}(\mathbf{k} + A^2\lambda/2\lambda_J^2) + \sqrt{\frac{1}{4}(\mathbf{k} + A^2\lambda/2\lambda_J^2)^2 + \mathbf{k}A^2\lambda/2\lambda_J^2}.$$

In the general case, the dispersion equation (10) can be studied only by numerical methods. In the range of wavevectors $\mathbf{k}\lambda \ge 1$, where the spatial nonlocality is also significant, the numerical analysis for $\lambda_J \le \lambda$ showed the existence of two regions of stability, $0 \le Q \le Q_{B1}(\mathbf{k})$ and $Q \ge Q_{B2}(\mathbf{k}, A, L)$, and the region of instability $Q_{B1}(\mathbf{k}) < Q < Q_{B2}(\mathbf{k}, A, L)$. Here, by the modulation instability, we imply the region of wavevectors of small amplitude perturbations $\mathbf{Q}$ for which the increment $\gamma(\mathbf{Q})$ is positive.

The regions of modulation instability of the plane nonlinear electromagnetic wave with fixed amplitude A and parameter L are depicted in the figure for various values of the reduced wavevector $\mathbf{k}\lambda$. According to these data, the region of modulation instability $Q_{B1}(\mathbf{k}) < Q < Q_{B2}(\mathbf{k}, A, L)$ can be controlled by varying the wavevector $\mathbf{k}$ of the linear approximation mode (or the corresponding frequency $\omega(\mathbf{k})$): as the reduced wavevector increases, the region of instability shifts as a whole toward greater Q values. Therefore, for $\mathbf{k} \ne 0$ (i.e., for the waves with dispersion), the long-wavelength region $0 \le Q \le Q_{B1}(\mathbf{k})$ is always the region of stability.

Thus, the spatially nonlocal character of the equation for the phase difference is very significant for plane nonlinear dispersed waves with a constant amplitude and a nonlinear phase shift in the Josephson junction.

First, the region of large-scale amplitude perturbations is always the region of stability for the waves with dispersion. Second, it is possible to control the region of modulation instability by varying the dispersion parameter **k** (or the frequency $\omega(\mathbf{k})$), which is very important for experimental investigations. It is important to note that, in the theory of the Josephson junction, the frequency $\omega(\mathbf{k})$ should be smaller than the limiting frequency Δ_{lim} [12] determined by the energy bandgap width Δ.

Experimentally, the development of modulation instability can be observed in extended Josephson junctions between massive superconductors, in which dispersed electromagnetic waves with small but finite amplitude subject to small modulations are excited at the Josephson frequency. In the course of development of the modulation instability, a plane nonlinear wave will evolve into a train of pulses (wave packets) with a repetition frequency determined by the period of modulation of the initial wave amplitude $L_0 = 2\pi/Q$, where wavevectors **Q** belong to the region $Q_{B1}(\mathbf{k}) < Q < Q_{B2}(\mathbf{k}, A, L)$. Note that, since the consideration was restricted to the amplitude modulation (with neglect of the phase modulation), the wave packets exhibit no self-contraction. An analogous behavior of the regions of modulation instability of dispersed electromagnetic waves can be expected for the Josephson junctions in thin superconducting films with thicknesses $d \ll \lambda$.

Acknowledgments. The author is grateful to Yu.V. Medvedev, I.B. Krasnyuk, Yu.E. Kuzovlev, and S.A. Fedorov for fruitful discussions, attention, and support.

REFERENCES

1. V. I. Karpman, *Nonlinear Waves in Dispersive Media* (Nauka, Moscow, 1973; Pergamon, Oxford, 1975).
2. B. B. Kadomtsev, *Collective Phenomena in a Plasma* (Nauka, Moscow, 1988) [in Russian].
3. G. A. Askar'yan, Zh. Éksp. Teor. Fiz. **42**, 1567 (1962) [Sov. Phys. JETP **15**, 1088 (1962)].
4. V. I. Bespalov and V. I. Talanov, Pis'ma Zh. Éksp. Teor. Fiz. **3**, 471 (1966) [JETP Lett. **3**, 307 (1966)].
5. M. J. Lighthill, J. Inst. Math. Appl. **1**, 269 (1965).
6. Yu. M. Aliev, V. P. Silin, and S. A. Uryupin, Sverkhprovodimost: Fiz. Khim. Tekh. **5**, 228 (1992).
7. A. Gurevich, Phys. Rev. B **46**, 3187 (1992).
8. F. Kh. Abdullaev, Pis'ma Zh. Tekh. Fiz. **23** (2), 8 (1997) [Tech. Phys. Lett. **23**, 52 (1997)].
9. A. Barone and G. Paterno, *Physics and Applications of the Josephson Effect* (Wiley, New York, 1982; Mir, Moscow, 1984).
10. K. K. Likharev, *Introduction to the Dynamics of Josephson Junctions* (Nauka, Moscow, 1985) [in Russian].
11. R. K. Dodd, J. C. Eilbeck, J. Gibbon, and H. C. Morris, *Solitons and Nonlinear Wave Equations* (Academic, New York, 1982; Mir, Moscow, 1988).
12. A. I. Larkin and Yu. N. Ovchinnikov, Zh. Éksp. Teor. Fiz. **51**, 1535 (1966) [Sov. Phys. JETP **24**, 1035 (1966)].

Translated by P. Pozdeev

Technical Physics Letters, Vol. 30, No. 2, 2004, pp. 135–137. Translated from Pis'ma v Zhurnal Tekhnicheskoĭ Fiziki, Vol. 30, No. 4, 2004, pp. 15–19.

Nanodimensional Effects in the Structure of Epitaxial $YBa_2Cu_3O_{7-y}$ Films

D. S. Korol'kov, E. M. Kaĭdashev, K. G. Abdulvakhidov, and M. F. Kupriyanov

Rostov State University, Rostov-on-Don, Russia

Received May 12, 2003; in final form, August 22, 2003

Abstract—We have studied the structure of $YBa_2Cu_3O_{7-y}$ (YBCO) high-T_c superconductor films obtained by deposition for various times under otherwise identical conditions. Thin YBCO films prepared by the nonaxial laser shadow deposition technique are epitaxial and have microstrains below 1×10^{-3}. The main factor determining variations of the unit cell parameter c in the films is the difference of the crystal block size $\langle D \rangle$ in the direction normal to the film surface, which reflects the nanodimensional effects known in oxides. *© 2004 MAIK "Nauka/Interperiodica".*

The results of numerous investigations show that the structure and physical properties of thin films of the $YBa_2Cu_3O_{7-y}$ (YBCO) high-T_c superconductor significantly depend on a number of factors, the main of which are as follows.

(i) On the unit cell level: the chemical composition (in particular, the oxygen stoichiometry) and the type and degree of ordering with respect to oxygen and vacancies [1–4].

(ii) On the level of crystal blocks: the crystal grain symmetry and volume and the degree of structural inhomogeneities (microstrains) [5, 6].

(iii) On the crystal level: the presence of extended defects and their types (dislocations, twin boundaries) [7].

(iv) Structural matching between the film and substrate [8].

In recent years featuring the rapid progress in nanoelectronics, much attention has been paid to the problem of modification and stabilization of the properties of nanostructured materials related to the manifestations of size effects. Thin epitaxial single crystal films of electrically active substances (ferroelectrics, superconductors) exhibit the size effects of two types related to the dependence of the structure and properties of such films on their thickness and peculiarities of the microblock structure.

We have used X-ray diffraction to study the relationships between various parameters characterizing the structural order and disorder on various levels in thin epitaxial YBCO films.

The samples of YBCO films were prepared by the nonaxial laser shadow deposition technique on (001)MgO single crystal substrates [9]. The beam of a YAG:Nd^{3+} laser was focused on a rotating ceramic target with the composition $YBa_2Cu_3O_{6.75}$ prepared as described in [10]. In order to increase the film deposition area, the laser beam was scanned over the target surface. The substrate temperature was varied in the interval from 700 to 760°C. The oxygen pressure in the chamber during deposition was 10–30 Pa. After termination of the deposition process, the chamber was filled with oxygen and the films were cooled to room temperature for 0.5 h.

The structures of the YBCO films of various thicknesses (samples (a)–(d)) were studied on an automated X-ray diffractometer of the HZG-4B type using CuK_α radiation. The measurements were performed in the Bragg–Brentano θ–2θ scheme with an intensity accumulation time of t = 2 s for a detector scanning in the angle interval $5° \le 2\theta \le 90°$ at a step of 0.02°. For the chosen goniometer slit widths, the X-ray diffraction patterns were obtained with a resolution of $\Delta\theta = 0.01°$.

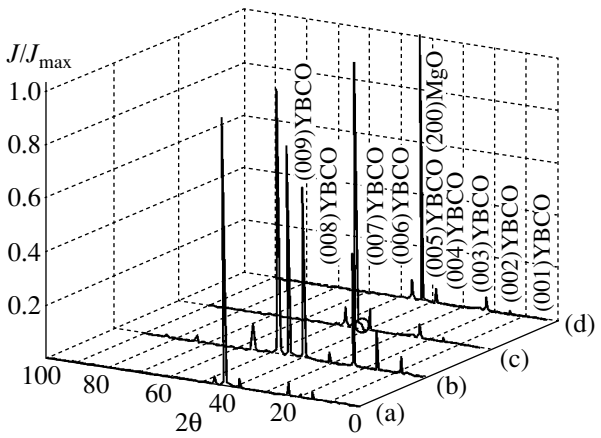

X-ray diffraction patterns of epitaxial YBCO films with various relative thicknesses: (a) 0.764; (b) 1; (c) 0.822; (d) 0.816 (the thickness of film (b) is 0.3 μm).

1063-7850/04/3002-0135$26.00 © 2004 MAIK "Nauka/Interperiodica"

The lattice parameter *c*, coherent scattering region size *D*, and reflection halfwidths *B* for thin epitaxial YBCO films

Sample	θ(006)	*c*, Å	*B*, deg	*D*, Å
a	23.272	11.697	0.37	259.6959
b	23.271	11.6976	0.37	259.6939
c	23.271	11.698	0.35	274.5336
d	23.292	11.6877	0.33	291.2179

Processing of the diffraction patterns included (i) high-precision determination of the lattice parameters, (ii) estimation of the size of coherence scattering regions ($\langle D \rangle$) and levels of microstrains, and (iii) evaluation of the effective film thicknesses.

The film thicknesses were estimated using the ratios of the integral intensities of X-ray reflections from film and substrate, I(006)YBCO/I(002)MgO, determined with allowance for the scattering factors according to the kinematic theory of X-ray diffraction. Using simple transformations, one can readily obtain the following equations for determining the film thicknesses:

$$I_1(h_1) \approx \frac{[1 + \cos^2(2\theta_1)]|F_1|^2\left(1 - \exp\left(-\frac{2\mu_1 h_1}{\sin\theta_1}\right)\right)N_1^2}{\sin(2\theta_1)\mu_1},$$

$$\frac{I_2(h_1)}{\approx \frac{[1 + \cos^2(2\theta_2)]|F_2|^2\left(1 - \exp\left(-\frac{2\mu_2 h_2}{\sin\theta_2}\right)\right)N_2^2\exp\left(-\frac{2\mu_2 h_2}{\sin\theta_2}\right)}{\sin(2\theta_2)\mu_2}},$$

where I_1 and I_2 are the intensities of reflections (here and below, indices 1 and 2 refer to the film and substrate, respectively); $|F_1|^2$ and $|F_2|^2$ are the structural factors; θ_1 and θ_2 are the Bragg reflection angles; h_1 and h_2 are the thicknesses; and μ_1 and μ_2 are the linear absorption coefficients.

The X-ray diffraction patterns of four thin YBCO films (a)–(d) with different relative thicknesses are presented in the figure. The thickness of film (b) is 0.3 μm. Evidently, the films have to be sufficiently "transparent" so as to detect the rays reflected from the substrate and measure the integral intensities of reflections with high precision.

It was established that the laser-deposited YBCO films represent epitaxial single crystal layers with the [001] direction perpendicular to the substrate plane. Only the X-ray diffraction pattern of sample (c) exhibited, besides reflections of the (00*l*) type, the (200) reflection showing the presence of a 90° (*a*–*c*)-twin structure. The influence of the coherent scattering regions and microstrains was determined by studying the dependence of the reflection halfwidths on the Bragg angle. The values of microstrains estimated from the halfwidths of the X-ray diffraction peaks were below 1×10^{-3} for all films. The main contribution to broadening of the (00*l*) reflections was related to the coherence scattering regions with dimensions $\langle D \rangle$ in the direction perpendicular to the film plane. Previously [11, 12], it was demonstrated that the unit cell parameter *c* of YBCO is highly sensitive to the parameter of nonstoichiometry *y* with respect to oxygen.

The fact that thin YBCO films (a)–(d) were prepared under identical conditions only differing by the deposition time excludes variation of the oxygen content. Therefore, the main factor responsible for the difference in the unit cell parameter *c* is the variation of the crustal block size $\langle D \rangle$ in the direction perpendicular to the film surface (see table). The increase in the parameter *c* observed in thin YBCO films with decreasing $\langle D \rangle$ reflects the size effects known in oxides, which were previously reported only for nanocrystalline powder oxide systems [13–17]. It should be noted that "loosening" of the crystal structure with decreasing size of nanocrystalline oxide particles in the region of critical dimensions (in contrast to the behavior observed in metals) leads to an increase in the crystal symmetry and, sometimes, to phase transitions of the reconstruction type.

The electric parameters determined by the four-point-probe technique and the results of magnetic susceptibility measurements for the obtained epitaxial YBCO films showed that the critical current density at 77 K and $B = 0$ in film (d) with maximum $\langle D \rangle$ reaches $J_c = 3 \times 10^6$ A/cm^2 and the phase transition temperature is $T_c = 90$ K. In the films with smaller $\langle D \rangle$ values, the critical currents decreased, while T_c remained virtually unchanged.

REFERENCES

1. I. Barbur, E. Burzo, V. Pop, *et al.*, Mater. Lett. **24**, 195 (1995).
2. K. Nakamura, A. Yu. Gufan, Yu. M. Gufan, *et al.*, Kristallografiya **44**, 510 (1999) [Crystallogr. Rep. **44**, 469 (1999)]; Kristallografiya **44**, 650 (1999) [Crystallogr. Rep. **44**, 603 (1999)].
3. Ya. S. Bobovich, Usp. Fiz. Nauk **167**, 973 (1997) [Phys. Usp. **40**, 925 (1997)].
4. A. Yu. Gufan, Yu. M. Gufan, Yu. V. Prus, and K. Nakamura, Fiz. Tverd. Tela (St. Petersburg) **42**, 1774 (2000) [Phys. Solid State **42**, 1819 (2000)].
5. M. S. Multani, P. Guptasarma, V. R. Palkar, *et al.*, Phys. Lett. A **142**, 293 (1989).
6. P. Ayyub, V. R. Palkar, S. Chattopadhyay, *et al.*, Phys. Rev. B **51**, 6135 (1995).

7. I. S. Lyubutin, Sverkhprovodimost: Fiz. Khim. Tekh. **4**, 2349 (1991).
8. A. Segmuller, Mater. Sci. Forum **79–82**, 493 (1991).
9. E. Kaidashev, V. Dneprovski, D. Breus, *et al.*, J. Supercond. **13**, 407 (2000).
10. N. Kofanova, V. Kogan, and M. Kupriyanov, Supercond. Sci. Technol., No. 14, 448 (2001).
11. J. D. Jorgensen, B. D. Veal, A. P. Paulikas, *et al.*, Phys. Rev. B **41**, 1863 (1990).
12. I. É. Grabaĭ, I. V. Zubov, A. S. Ilyushin, *et al.*, Fiz. Tverd. Tela (Leningrad) **30**, 3436 (1988) [Sov. Phys. Solid State **30**, 1971 (1988)].
13. A. I. Gusev and A. A. Rempel', *Nanocrystalline Materials* (Fizmatlit, Moscow, 2000) [in Russian].
14. M. Ya. Gamarnik, Mater. Sci. Forum **133–136**, 927 (1993).
15. S. O'Brien, L. Brus, and B. Murray, J. Am. Chem. Soc. **123**, 12085 (2001).
16. S. Tsenekawa, K. Ishikawa, Z.-Q. Li, *et al.*, Phys. Rev. Lett. **85**, 3440 (2000).
17. V. R. Palkar, P. Ayyub, S. Chattopadhyay, *et al.*, Phys. Rev. B **53**, 2167 (1996).

Translated by P. Pozdeev

Technical Physics Letters, Vol. 30, No. 2, 2004, pp. 138–140. Translated from Pis'ma v Zhurnal Tekhnicheskoĭ Fiziki, Vol. 30, No. 4, 2004, pp. 20–24.

Sensitivity of the Thermocapillary Method of Thickness Determination for Transparent Liquid Films on Horizontal Absorbing Substrates

B. A. Bezuglyi* and O. A. Tarasov

Tyumen State University, Tyumen, Russia

** e-mail: bezuglyi@utmn.ru*

Received July 10, 2003

Abstract—We present data on the sensitivity of a new method of determining the thicknesses of thin films on flat horizontal substrates, based on the measurement of a stationary thermocapillary response. In the range of film thicknesses exceeding the thermocapillary rupture thickness by no more than 10 μm, the error of the film thickness determination is no greater than 1–2 μm. By increasing the power of the laser beam inducing the thermocapillary convection from 3.5 to 16.5 mW, it is possible to keep the relative error of measurement within 5% in the range of film thicknesses from 150 to 1000 μm for liquids with viscosities within 0.8–5.6 cSt.

Previously [1], we described a new method for determining the thicknesses of thin transparent liquid layers on absorbing flat substrates based on laser-induced thermocapillary (TC) convection and demonstrated the possibility of using this technique in the case of a wedge-shaped layer. The experiments were performed with a beam power of P = 1.2 mW, which restricted the range of thicknesses to within 300–440 μm. Now, we have studied the sensitivity of this technique for a laser beam power of up to 16.6 mW, which expands the range of measurable film thicknesses up to 1100 μm.

The measurements were performed for plane-parallel liquid layers at a temperature of 24 ± 1°C. The experimental setup was described elsewhere [2]. The layer of a liquid on a 40 × 40 × 4 mm carbolite resin substrate in a Petri dish was exposed to the beam of a He–Ne laser (LG-111, λ = 633 nm) focused in a spot of 3.5 ± 0.5 mm diameter on the substrate surface. The substrate surface was adjusted in a horizontal plane with the aid of a micrometric goniometer table. The liquid layer thickness was preset using a calibrated wire technique [2] with an error not exceeding 10 μm.

After a steady state of the TC response was achieved, its diameter D on the screen was measured with a slide gage. The optical pathlength from the sample surface to the screen was 160 cm. The measurements were performed for several values of the laser beam power P. The experiments were carried out with the layers of four liquids: octane, *o*-xylene, 1-butanol, and benzyl alcohol (viscosities at 20°C: 0.78, 0.92, 3.64, and 5.56 cSt, respectively) [3, 4]. The layer thicknesses h were varied in the range from a value corresponding to the onset of TC convection (whereby the response diameter began to differ from the value for the beam reflected from a flat liquid surface) to the critical value h^* corresponding to the TC rupture of the liquid film (Table 1).

The sensitivity of the proposed method is characterized by the ratio $\Delta D/\Delta h$, where ΔD is the increment of the TC response diameter corresponding to the layer thickness increment Δh. The minimum value of Δh was 12 μm. For the liquid layers with thicknesses close to the TC rupture thickness (i.e., for $h \cong h^* + 10$ μm), the $\Delta D/\Delta h$ ratio reaches 0.8–0.9 mm/μm; for thicknesses on the order of $h^* + 300$ μm, this ratio decreases to 0.06–0.10 mm/μm (data for octane layers probed at P = 5.5 mW, see Fig. 1). The coincidence of the values of sensitivities for the liquids possessing different viscos-

Table 1. Critical layer thicknesses h^* for some liquids probed at P = 5.5 mW

Liquid	Octane	*o*-Xylene	1-Butanol	Benzyl alcohol
h^*, μm	380	355	295	200

Table 2. TC response diameter D for benzyl alcohol layers with $h \cong h^* + 10$ μm probed at various laser beam powers P

P, mW	3.4	7.6	16.6
h, μm	155	235	340
D, mm	140	220	300

ities in this study, in contrast to the results reported in [1],[1] is related to the fact that we deal with sample thicknesses in the range above the TC rupture thickness rather than with thicknesses in a fixed interval. It should also be noted that plots of the sensitivity versus layer thickness for the same laser beam power are of the same shape and can be obtained by parallel translation along the ordinate axis.

It was found that the ratio $\Delta D/\Delta h$ in the region of the TC rupture thickness increases with the laser beam power. Indeed, for benzyl alcohol, this ratio is 0.8, 1.8, and 4.6 mm/μm for P = 3.4, 7.6, and 16.6 mW, respectively. The increase in the sensitivity is related to the fact that higher P corresponds to a greater diameter of the TC response (Table 2).

In the region of the TC rupture thickness, the TC response diameter reached D = 150–300 mm. As a result of blurring of the spot edge, the absolute error of measurement of the D value was 2–4 mm. For the above values of the ratio $\Delta D/\Delta h$, the error of determination of the layer thickness can be estimated at 1–2 μm. This accuracy is close to that provided by the interferometric techniques [5–7]. However, our method is advantageous in being much less sensitive to vibrations of the free liquid surface. We believe that a severalfold increase in accuracy of the proposed technique can be achieved by using automated determination of D at a preset brightness level.

Figure 1 shows a plot of the relative error of thickness determination versus thickness for octane layers, calculated assuming the absolute error of D measurements to be 1 μm.[2] In the range of layer thicknesses from h^* to h^* + 300 μm, the relative error falls within the interval from 0.3 to 2.5%. For the same laser beam power (5.5 mW), the plots of relative error versus thickness for three other liquids have similar shapes (with respect to h^*).

Since an increase in the laser beam power is accompanied by an almost linear growth in the TC response diameter [8], a decrease in D (related to an increase in the liquid layer thickness or viscosity) can be compensated by increasing P. For example, the relative error of thickness determination for a 580-μm-thick layer of benzyl alcohol probed by the laser beam with a power of 3.4, 7.6, and 16.6 mW is about 6.5, 2.0, and 0.8%, respectively (Fig. 2). The relative error of thickness determination in the range within 300–400 μm above the TC rupture thickness for liquids with a viscosity of 0.8–5.6 cSt probed by a 16.5-mW laser beam does not exceed 1–2%.

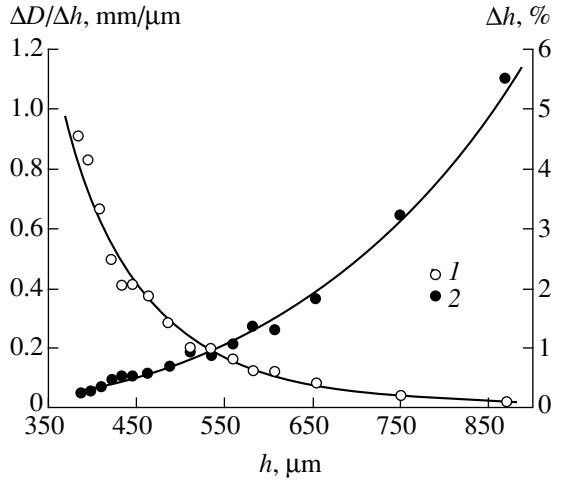

Fig. 1. The plots of (*1*) sensitivity and (*2*) relative error of the proposed method for octane layer with various thicknesses probed at a laser beam power of 5.5 mW.

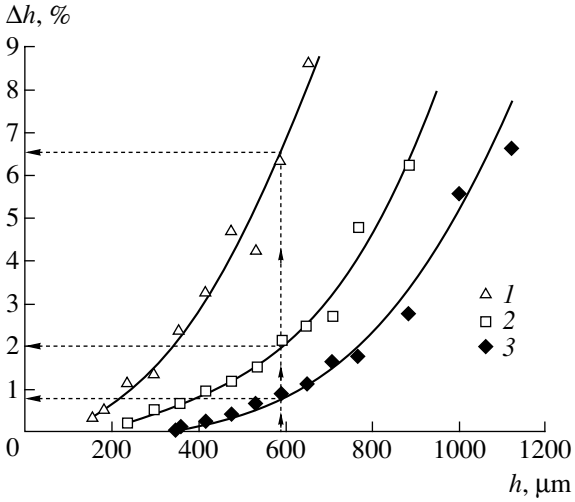

Fig. 2. Decrease of the relative error of thickness determination by the proposed method with increasing laser beam power. The data for benzene layers probed at P = 3.4 (*1*), 7.6 (*2*), and 16.6 mW (*3*).

The upper boundary of thicknesses measurable by the proposed method can be estimated at 3–4 mm [9] using the condition that TC forces predominate over thermogravitational forces. The lower boundary of measurable thicknesses corresponds to the TC rupture thickness: by decreasing the laser beam power, this boundary can be reduced to about 100 μm.

Acknowledgments. This study was supported in part by the Program of Grants for Young Scientists from the Governor of the Tyumen Oblast, project no. 118-01.

[1] Unfortunately, the media in [1, p. 360] are not listed in the order of decreasing viscosity: the correct sequence is Vaseline oil, benzyl alcohol, 1-butanol, and octane.

[2] The same absolute error was used for constructing the plots in Fig. 2.

REFERENCES

1. B. A. Bezuglyi and A. A. Fedorets, Pis'ma Zh. Tekh. Fiz. **27** (9), 20 (2001) [Tech. Phys. Lett. **27**, 359 (2001)].

2. B. A. Bezuglyi and O. A. Tarasov, Opt. Spektrosk. **92**, 665 (2002) [Opt. Spectrosc. **92**, 609 (2002)].

3. *A Handbook of Chemist*, 2nd ed. (Goskhimizdat, Moscow, 1962) [in Russian], Vol. 1.

4. N. B. Vargaftik, *Tables of Thermophysical Properties of Liquids and Gases* (Nauka, Moscow, 1972; Halsted Press, New York, 1975).

5. *Devices for Nondestructive Control of Materials and Products*, Ed. by V. V. Klyuev (Mashinostroenie, Moscow, 1986) [in Russian].

6. I. V. Skokov, *Multiple-Beam Interferometers for Measurement Techniques* (Mashinostroenie, Moscow, 1989) [in Russian].

7. E. A. Gusev, *Devices for Nondestructive Control in Machine Building* (Mashinostroenie, Moscow, 1993) [in Russian].

8. B. A. Bezuglyi, Candidate's Dissertation (Mosk. Gos. Univ., Moscow, 1983).

9. K. K. Tan and R. B. Thorpe, Chem. Eng. Sci. **54**, 775 (1999).

Translated by P. Pozdeev

Technical Physics Letters, Vol. 30, No. 2, 2004, pp. 141–143. Translated from Pis'ma v Zhurnal Tekhnicheskoĭ Fiziki, Vol. 30, No. 4, 2004, pp. 25–32.

Deterministic Stochastic Resonance in a Bistable Semiconductor System

I. K. Kamilov, K. M. Aliev, Kh. O. Ibragimov, and N. S. Abakarova

Institute of Physics, Dagestan Scientific Center, Russian Academy of Sciences, Makhachkala, Dagestan, Russia

e-mail: khmurat@iwt.ru

Received July 1, 2003

Abstract—The phenomenon of deterministic stochastic resonance has been experimentally observed and studied for the first time in a bistable semiconductor system with an S-shaped current–voltage characteristic exhibiting a transition to chaos via intermittency. Spectral regions featuring amplification of an external signal and phase locking are determined as dependent on the frequency and amplitude of the external signal and the control parameter. © *2004 MAIK "Nauka/Interperiodica".*

Previously [1–4], we demonstrated that *p*-Ge(Au) based structures, featuring the development of a recombination instability of current at 77 K, can operate in various regimes in the voltage–emission phase space, possess S-shaped current–voltage characteristics, and exhibit transitions to chaotic states via intermittency. Recently, Anishchenko *et al.* [5–7] theoretically predicted the possibility of a special resonance behavior for bistable systems with chaotic dynamics in the presence of several coexisting attractors and a weak internal noise. These investigations led to the discovery of a basically new effect called the deterministic stochastic resonance. The noise intensity in such systems is described by a parameter controlling large (slow) time scale and determining the spectral properties. A quasipotential (an analog of the free energy for nonequilibrium stationary states) depending only on the state variables and parameters of the system acquires a minimum value at an attractor. When a periodic external signal acts upon a system, it is possible to select the parameters so that the signal period will coincide with an average time of switching from one attractor to another. This situation is analogous to the stochastic resonance.

In order to experimentally verify the theory of deterministic stochastic resonance, we used a bistable *p*-Ge(Au) semiconductor system with double injection possessing an S-shaped current–voltage characteristic and exhibiting a chaotic behavior with intermittency in the region of switching [1–4]. The sample structures were prepared using *p*-type germanium doped with antimony and compensated with gold. The concentration of deep-level impurity was 2×10^{15} cm^{-3}, the background hole density was $p_0 = 4.33 \times 10^9$ cm^{-3}, the hole mobility was $\mu = 16500$ cm^2/(V s), and the resistivity at 77 K was $\rho = 8.7 \times 10^4$ Ω cm. Nonequilibrium carriers were injected from In–0.5% Ga and Sn–7% Sb contacts deposited onto opposite faces of a 0.8-mm-long sample with a ~4 mm^2 cross section area. In order to avoid Joule heating of the sample, the measurements were performed in a pulsed regime with a pulse duration not exceeding 1 ms. The time series of the voltage and current oscillations were digitized by a two-channel analog-to-digital converter with a master clock frequency of 200 MHz and fed to a computer for data processing. These data were used to construct the phase portraits, bifurcation diagrams, and power spectra and to determine dimensionality of the system. The system response was studied using a galvanically decoupled periodic external signal with the amplitude and frequency controlled within broad limits, applied via a pulse transformer.

When the applied pulsed voltage was selected so as to correspond to a switching threshold, the system exhibited an S-shaped current–voltage characteristic, as illustrated by the time series of voltage $U(t)$ and current $I(t)$ in Fig. 1a. The current pulse step prior to S-switching displays well-pronounced chaotic oscillations related to the domain formation in the sample [1–4]. If a load resistor connected in series with the structure studied is equal to the resistance on the S-shaped region of the current–voltage characteristic, the system exhibits an oscillatory behavior resembling intermittency, with a continuous noise band in the power spectrum (Fig. 1b) corresponding to a fractal dimension of $D = 2.23$.

When a small external harmonic signal of selected frequency is applied to the system, the power spectrum exhibits a sharp peak on the continuous noise background (Fig. 1c). By controlling the electric field parameter ε and selecting the external signal frequency, it is possible to provide for a resonance amplification of the applied signal. Figure 2a shows an example of such amplification on the current pulse background: the small applied signal can be seen near the base of the

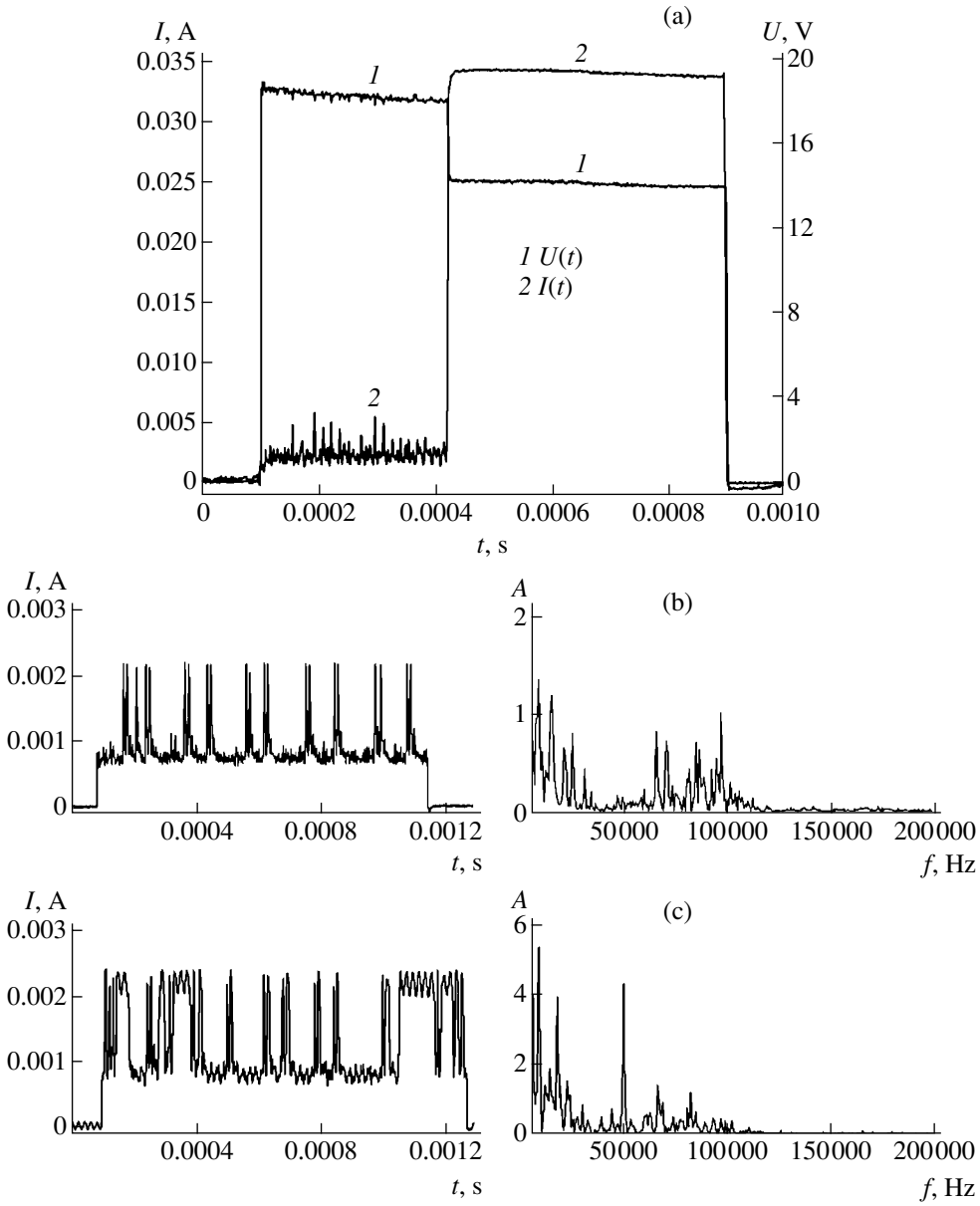

Fig. 1. Time series of (a) the voltage $U(t)$ and current $I(t)$ on the S-shaped part of the current-voltage characteristic and (b, c) current pulses $I(t)$ in the absence and in the presence of an external signal, respectively (right-hand panels show the corresponding power spectra).

current pulse, while the rectangular pulse is modulated by the amplified signal. In our experiments, the signal gain reached 40 dB. It should be noted that the resonance frequencies correspond with a high coherence to the double characteristic time of S-switching. This characteristic time, in turn, depends on the electric field parameter. The resonance amplification with a large modulation of the current pulse was also observed for a period of $2T$, but the coherence of the amplified signal was significantly lower. Figure 2b shows the spectrum of amplification coefficient for an external harmonic signal of constant amplitude with the frequency varied from 20 to 200 kHz (for an electric field parameter of 20 V).

In the absence of external noise, the phase trajectory of the system belongs to one or another attractor, depending on the electric field parameter and the initial conditions. Stable points of a bistable system may correspond to the lower and upper S-switching points. For sufficiently large amplitude of the external signal (in the absence of external noise), the process of switching is fundamentally nonlinear, with the statistics strongly dependent on the electric field parameter ε. According to the theory [5], the average frequency of switching monotonically increases with the value of ε in a certain region of this parameter. Figure 2c shows a plot of the amplification coefficient versus ε, illustrating the phenomenon of deterministic stochastic resonance. The

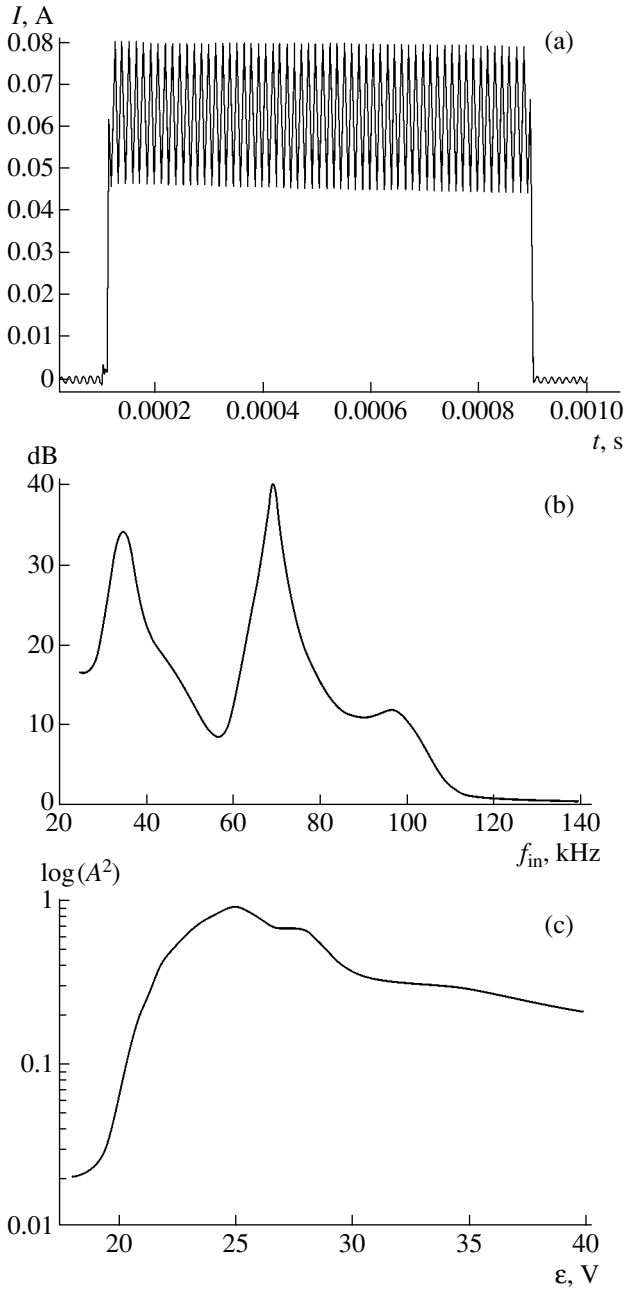

Fig. 2. Amplification of an external signal: (a) a current pulse modulated by the amplified signal; (b) frequency dependence of the amplification coefficient; (c) dependence of the amplification coefficient on the control parameter ε.

maximum gain is observed in the region where the Kramers frequency is close to the external signal frequency.

The phenomenon of phase locking is universal and can be observed in a broad class of dynamical systems. We have also observed locking of the average switching frequency by an external signal for various values of ε, as well as the phenomenon of induced synchronization manifested in locking of the switching frequency by a periodic signal on the plane of parameters "external signal amplitude–control parameter." As expected, the region of synchronization tends to increase with the external signal amplitude. Experiments showed the presence of an amplitude threshold for the synchronization.

It should be noted that threshold values of the parameters of electric field, frequency, and amplitude for the deterministic stochastic resonance exhibit a hysteresis behavior. If the parameters of electric field, amplitude, and resonance frequency of the external signal in the regime of resonance amplification remain constant and only the output frequency of the synchronization region is varied, the current amplitude exhibits an exponential decrease and stabilization on a level of 0.77% of the resonance value. Subsequent increase in the frequency leads to further decrease in the pulse amplitude, followed by the pulse decomposition into two, three, and more trains of pulses and by the passage to a chaotic state resembling intermittency. Thus, by varying the frequency, it is possible to control the pulse modulation amplitude and the number of pulses within a given time interval.

In conclusion, the experimental results presented above confirm most of the theoretical predictions concerning the possibility of deterministic stochastic resonance in real bistable semiconductor systems with intermittency.

Acknowledgments. This study was supported by the Russian Foundation for Basic Research, project no. 02-02-17817.

REFERENCES

1. I. K. Kamilov, N. S. Abakarova, Kh. O. Ibragimova, and K. M. Aliev, Pis'ma Zh. Tekh. Fiz. **27** (5), 24 (2001) [Tech. Phys. Lett. **27**, 183 (2001)].
2. Kh. O. Ibragimov, I. K. Kamilov, K. M. Aliev, and N. S. Abakarova, Pis'ma Zh. Tekh. Fiz. **29** (3), 82 (2003) [Tech. Phys. Lett. **29**, 122 (2003)].
3. N. S. Abakarova, Kh. O. Ibragimov, K. M. Aliev, *et al.*, Semicond. Sci. Technol. **16**, 11 (2001).
4. I. K. Kamilov, Kh. O. Ibragimov, K. M. Aliev, *et al.*, Semicond. Sci. Technol. **18**, 442 (2003).
5. V. S. Anishchenko, A. B. Neĭman, F. Moss, *et al.*, Usp. Fiz. Nauk **169**, 7 (1999) [Phys. Usp. **42**, 7 (1999)].
6. V. S. Anishenko, A. B. Neiman, and M. A. Safonova, J. Stat. Phys. **70**, 183 (1993).
7. V. S. Anishenko, M. A. Safonova, and L. O. Chua, Int. J. Bifurcation Chaos Appl. Sci. Eng. **2**, 397 (1992).

Translated by P. Pozdeev

Technical Physics Letters, Vol. 30, No. 2, 2004, pp. 144–147. Translated from Pis'ma v Zhurnal Tekhnicheskoĭ Fiziki, Vol. 30, No. 4, 2004, pp. 33–41.

High-Frequency Stabilization of a Magnetoplasmadynamic Thruster

K. P. Kirdyashev

Fryazino Branch, Institute of Radio Engineering and Electronics, Russian Academy of Sciences, Fryazino, Moscow oblast, Russia

Received June 30, 2003

Abstract—Experimental data on the high-frequency stabilization and the suppression of low-frequency oscillations in a magnetoplasmadynamic thruster are presented. Conditions for the stabilizing effect of a high-frequency magnetic field on the plasma jet produced by the thruster are determined, and the efficiency of this action is evaluated. © *2004 MAIK "Nauka/Interperiodica".*

As is known, electric discharges used for the acceleration of plasma are subject to large-scale low-frequency instabilities, reducing the efficiency of acceleration and leading to oscillations in the plasma density and to the scatter of ion velocities in the output plasma flow. In the limiting (high-voltage) operation regimes of magnetoplasmadynamic (MPD) thrusters, the development of such instabilities leads to the excitation of voltage oscillations comparable in magnitude with the applied voltage and leading to breakdown of the acceleration process [1–3]. When MPD thrusters are used as the elements of spacecraft engines, the low-frequency instabilities give rise to fluctuations of the amplitude and phase of radio waves scattered from oscillations in the plasma formations near a space vehicle. In this context, investigations of the applicability of the well-known methods of plasma stabilization for the suppression of oscillations in the accelerated plasma and the creation of low-turbulent plasma formations are of very large importance.

Methods developed previously for the high-frequency stabilization of plasmas are capable of effectively suppressing low-frequency instabilities, which are most dangerous from the standpoint of the formation of accelerating layers and the excitation of plasma density and potential perturbations extended along the magnetic field lines. During the tests of MPD thrusters, such instabilities are manifested by the formation of inhomogeneous plasma flows experimentally observed as azimuthal drift waves [2]. It was established [4, 5] that the stabilization of plasma jets with respect to the development of drift instabilities can be based on the notion of electron oscillations in a high-frequency electric field. These oscillations give rise to the effective electron temperature, increase the frequency of drift waves, and enhance their damping on thermal electrons.

During the acceleration of plasmas in electric and magnetic fields, the high-frequency stabilization can be provided by a method based on the action of a high-frequency magnetic field [6, 7]. This method of plasma stabilization can be implemented using conductors carrying a high-frequency current generating an alternating magnetic field in the region of plasma acceleration. This high-frequency magnetic field induces oscillations of the magnetic field lines in the MPD thruster field. Electrons moving with thermal velocities along the oscillating magnetic field lines decrease the electric field of low-frequency oscillations, thus reducing instability and suppressing oscillations in the output plasma flow. The possibility of applying this method of high-frequency stabilization to the plasma accelerated in MPDs was suggested by experiments [8].

Based on the results of ground tests for a stationary gas-discharge MPD thruster system [9], conditions were established for the stabilizing action of a high-frequency field on the accelerated plasma and the efficiency of this action was evaluated. The investigation was performed on a stationary thruster prototype with a coaxial electrode system comprising a heated central cathode and a ring anode (Fig. 1). In the working thruster regimes, a non-self-sustained electric discharge in a weakly divergent magnetic field is formed in the plasma acceleration region. The working gas (argon) supplied via the anode surface at the magnetic coil edge in the discharge region was ionized by electrons emitted from the cathode.

The thruster operation was studied in the regimes corresponding to a discharge voltage within 150–200 V, a discharge current of 1–2 A, and a longitudinal magnetic field strength of up to 4×10^4 A/m in the cathode region. The working gas supply rate was $(1–5) \times 10^{-2}$ g/s at a residual gas pressure in the vacuum chamber from 8.5×10^{-2} to 1.5×10^{-1} N/m^2. Under these conditions, the maximum electron density in the region of plasma acceleration was $(1.0–2.5) \times 10^{11}$ cm^{-3} and the electron temperature near the cathode was 5–10 eV. The results of measurements using movable electrical

1063-7850/04/3002-0144$26.00

probes showed that the plasma flow at the output of the acceleration region is characterized by inhomogeneous longitudinal and radial distributions of parameters. The initial plasma jet cross section is determined by the cathode radius. In the external region, the electron density and temperature at a distance of 1.0–1.5 cm from the jet axis decrease to 10^{10} cm^{-3} and 1 eV, respectively.

The probe potential measured in the thruster regimes indicated above exhibited oscillations in the frequency range of 30–50 kHz related to oscillations in the output plasma flow density. Special features of these oscillations were the presence of an excitation threshold with respect to the magnetic field strength and the intensity maximum in the peripheral region of the discharge characterized by the maximum electron density gradient. These peculiarities allow the drift instability in the plasma acceleration region to be considered as one of the factors responsible for the excitation of low-frequency oscillations in the plasma flow. Estimates of the frequency of drift oscillations, obtained taking into account the experimental data on the electron density gradient and temperature in the inhomogeneous plasma, are consistent with the frequencies of discrete spectral components observed in the spectra of electric potential oscillations (Fig. 2a). The amplitude of the plasma potential oscillations in the peripheral discharge region was 0.5–1.0 V. Assuming that the oscillations possess a potential character and taking into account the electron temperature (1–5 eV), this corresponds to the electron density oscillations within $\Delta n_e/n_e \le 0.2$–1.0 in the output plasma flow.

The effect of a stabilizing high-frequency field on the MPD thruster was studied at a frequency of 40 MHz. The field was generated by a helical coil positioned at the boundary of the output plasma jet. Effective stabilization of the plasma was provided by selecting the stabilizing generator frequency Ω so as to obey the conditions $\omega_{ei} < \Omega \ll \omega_{He}$ and $\Omega > \nu_e$, where ω_{ei} is the lower hybrid frequency, ω_{He} is the cyclotron frequency for electrons, and ν_e is the effective frequency of electron collisions (estimates show that, under the experimental conditions studied, electron collisions with working gas atoms are predominant). The depth of the stabilizing field penetration into the plasma was estimated as $\delta \approx c/\omega_{Pe}$, where ω_{Pe} is the Langmuir frequency for electrons in the inhomogeneous region of the plasma flow. Estimates yield δ = 2–3 cm, which implies the volume action of the field on the inhomogeneous plasma region featuring the drift instability. This is confirmed by weak variations of the high-frequency field strength in the plasma jet cross section measured using a movable electrical probe. The action of the stabilizing high-frequency field on the plasma flow was accompanied by nonlinear effects related to the excitation of harmonics of the main frequency (intensity of the second harmonic amounted to 0.3–0.4 of the main field).

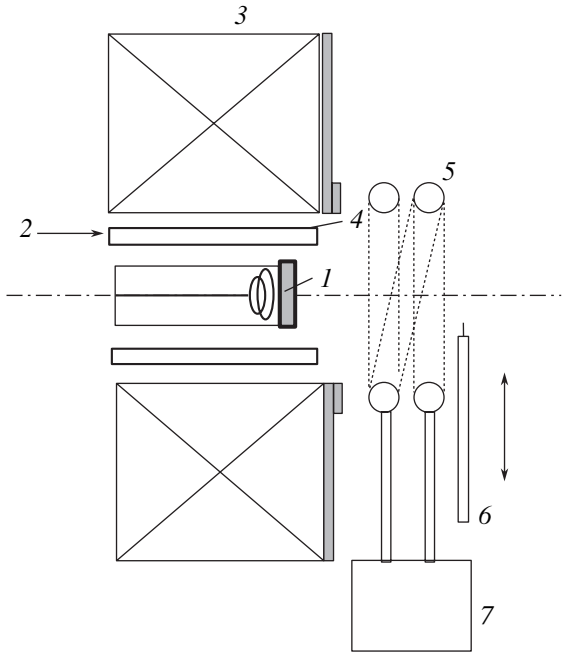

Fig. 1. Schematic diagram of the experimental stationary plasma thruster: (*1*) cathode unit (internal diameter, 2.1 cm); (*2*) working gas supply; (*3*) magnetic system; (*4*) anode (internal diameter, 4.9 cm); (*5*) stabilizing circuit; (*6*) movable electrical probe; (*7*) high-frequency generator.

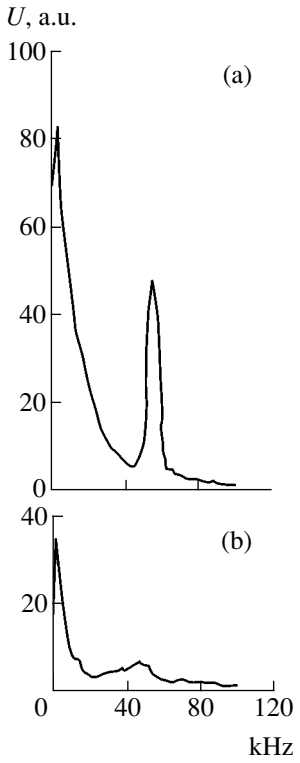

Fig. 2. The spectra of potential oscillations measured by an electrical probe in a plasma flow (a) without stabilization of the electric discharge and (b) in the presence of a stabilizing high-frequency field.

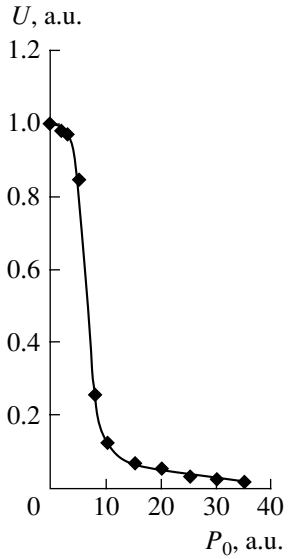

Fig. 3. The plot of intensity of the drift component of low-frequency oscillations in the plasma flow versus power of the stabilizing high-frequency generator (maximum power, 80 W).

The results of experiments showed effective (up to 15–20 dB) suppression of discrete components in the spectrum of low-frequency oscillations (Fig. 2b) related to the development of drift instability in the plasma acceleration region. The threshold power of the stabilizing high-frequency generator (Fig. 3), above which the low-frequency turbulence of the plasma flow was effectively suppressed, was 10–20 W (at a total thruster power of 400–800 W). The discrete component frequencies in the oscillation spectrum observed in the presence of the high-frequency field are independent of the stabilizing generator frequency. This fact excludes the stabilizing action of the electric component of the high-frequency field (observed in the experiments reported in [10]). The threshold magnetic field strength calculated from the threshold stabilizing generator power obeys the stabilization criterion [5–7]:

$$\tilde{H} \geq (\Omega/k_\perp v_{Te})H_0, \qquad (1)$$

where $\tilde{H}$ is the amplitude of the magnetic field generated by the high-frequency circuit, H_0 is the constant magnetic field producing plasma acceleration in the thruster, $k_\perp \approx m/R_{Pl}$ is the transverse (relative to the magnetic field direction) component of the wavevector of low-frequency perturbations, m is the oscillation mode, R_{Pl} is the plasma jet radius, and v_{Te} is the thermal velocity of electrons.

Depending on the electric discharge conditions in the MPD thruster, application of the high-frequency magnetic field produced either suppression or additional excitation of the low-frequency turbulence in the plasma flow. The transition from stabilizing action to excitation of the low-frequency oscillations was manifested by an increase in the working gas consumption and pressure in the vacuum chamber of the experimental setup. Under these conditions, it is necessary to consider the development of a drift-dissipative instability in the plasma acceleration region [5]. For this process, the stabilization threshold with respect to the magnetic field strength for $\nu_e \geq \Omega$ obeys the criterion

$$\tilde{H} \geq (\Omega/k_\perp v_{Te})(\nu_e/\Omega)^{1/2}H_0. \qquad (2)$$

Let us consider the main factors limiting the efficiency of plasma stabilization by the high-frequency magnetic field. These are the additional ionization of the working gas and an increase in the electron temperature under the action of the electric component of the high-frequency field generated by the stabilizing circuit. The presence of the electric component of the high-frequency field is confirmed by the results of electrical-probe measurements of the potential oscillations at the stabilizing generator frequency and its harmonics.

The transition of the plasma thruster to a regime of destabilizing action of the high-frequency field is most pronounced during the resonance excitation of plasma oscillations [11] at the stabilizing generator frequency $\Omega = \omega_-(\theta)$ given by the formula

$$\omega_-^2 = \omega_{Pe}^2\cos^2\theta/(1 + \omega_{Pe}^2/\omega_{He}^2). \qquad (3)$$

Here, $\omega_-(\theta)$ is the natural frequency of electron oscillations and θ is the angle between the wavevector of oscillations and the magnetic field. According to estimates obtained taking into account the known ω_{Pe} and ω_{He} values, the experimental conditions provide for a resonance between the external high-frequency field and the natural plasma oscillations at $\cos\vartheta \ll 1$ (the value of $\cos\vartheta = k_z/k$ can be estimated using the ratio of the longitudinal (ΔL_{Pl}) and transverse (ΔR_{Pl}) dimensions of inhomogeneity of the output plasma flow: $k_z \approx 1/\Delta L_{Pl}$, $k_\perp \approx 1/\Delta R_{Pl}$, and $k_z/k \approx 4 \times 10^{-2}$).

In the frequency range of the stabilizing generator, the system also exhibits a parametric instability [11] of the accelerated plasma, which is manifested by an increase in the electric field component observed during measurements of the high-frequency potential oscillations with the aid of an electrical probe. The maximum velocity of electron oscillations in the high-frequency electric field of amplitude $\tilde{E}$ under the experimental conditions studied was $v_E = e\tilde{E}/m_e\Omega \approx 2 \times 10^8$ cm/s. The thermal velocity of electrons in the region of inhomogeneous plasma flow is estimated at $v_{Te} = (6–9) \times 10^7$ cm/s. Under these conditions, the destabilizing action of the electric component of the high-frequency field is consistent with the notions of nonlinear absorption of the field energy and excitation

of experimentally observed broad spectrum of ion sound oscillations in the accelerated plasma.

Thus, the effect of a high-frequency field on the plasma accelerated in an MPD thruster is determined by the competition of two processes: (i) suppression of a drift instability by the magnetic field component and (ii) energy pumping from the intrinsic oscillations excited in the plasma by the external field to the ion sound waves. The effect of suppression of the drift instability of the plasma flow is observed for a relatively small power of the stabilizing generator, not exceeding 5–10% of the power of the plasma thruster. By selecting an optimum frequency of the stabilizing generator, it is possible to increase the efficiency of suppression of the low-frequency turbulence in the MPD thruster plasma jet. This is expected to improve both the propulsion characteristics of the thruster and conditions of radio wave propagation through plasma formations in the vicinity of space vehicles.

REFERENCES

1. K. P. Kirdyashev, *Microwave Wave Processes in Plasmadynamic Systems* (Énergoatomizdat, Moscow, 1982) [in Russian], p. 142.
2. N. N. Glotova, K. P. Kirdyashev, I. N. Ostretsov, and A. A. Porotnikov, Zh. Tekh. Fiz. **46**, 506 (1976) [Sov. Phys. Tech. Phys. **21**, 288 (1976)].
3. K. P. Kirdyashev and V. I. Brukhtia, Pis'ma Zh. Tekh. Fiz. **27** (11), 36 (2001) [Tech. Phys. Lett. **27**, 457 (2001)].
4. Ya. B. Faĭnberg and V. D. Shapiro, Zh. Éksp. Teor. Fiz. **52**, 293 (1967) [Sov. Phys. JETP **25**, 189 (1967)].
5. A. A. Ivanov, *Physics of Highly Nonequilibrium Plasma* (Atomizdat, Moscow, 1977) [in Russian], p. 352.
6. A. A. Ivanov, L. I. Rudakov, *et al.*, Zh. Éksp. Teor. Fiz. **54**, 1380 (1968) [Sov. Phys. JETP **27**, 739 (1968)].
7. S. I. Krasheninnikov and T. K. Soboleva, in *Proceedings of the 3rd All-Union Conference on Plasma Accelerators, Minsk, 1976*, pp. 214–215.
8. I. D. Bozhko, K. P. Kirdyashev, and A. V. Potapov, in *Proceedings of the 4th All-Union Conference on Plasma Accelerators and Ion Injectors, Moscow, 1978*, pp. 235–236.
9. K. P. Kirdyashev, A. V. Potapov, L. E. Tsvetkova, *et al.*, Fiz. Plazmy **2**, 542 (1976) [Sov. J. Plasma Phys. **2**, 296 (1976)].
10. R. A. Demirkhanov, G. L. Khorasanov, and I. K. Sidorova, in *Proceedings of the 3rd International Conference on Plasma Physics and Controlled Nuclear Fusion Research* (IAEA, Vienna, 1969), Vol. 2, pp. 449–459.
11. V. P. Silin, *Parametric Effect of High-Power Radiation on Plasma* (Nauka, Moscow, 1973) [in Russian], p. 288.

Translated by P. Pozdeev

Technical Physics Letters, Vol. 30, No. 2, 2004, pp. 148–150. Translated from Pis'ma v Zhurnal Tekhnicheskoĭ Fiziki, Vol. 30, No. 4, 2004, pp. 42–48.

Tribospectroscopy of Surfaces with Statistically Random Roughness

V. L. Popov[a,b] and O. K. Dudko[c]

[a] *Berlin Technical University, Berlin, Germany*

[b] *International Center for Investigations in Physical Mesomechanics of Materials, Tomsk, Russia*

[c] *Institute for Low Temperature Physics and Engineering, National Academy of Sciences of Ukraine, Kharkov, Ukraine*

Received August 18, 2003

Abstract—The static force of friction between two bodies moving in a random potential and coupled by a randomly oscillating bond is studied as a function of the oscillation amplitude. It is shown that this dependence can be used for reconstructing the spectral density of the random potential. These results provide a basis for the experimental determination of the characteristic scale of friction processes from the law of friction of oscillating tribosystems. © *2004 MAIK "Nauka/Interperiodica".*

In order to formulate adequate models of the friction and wear processes, it is necessary to know the characteristic scale of phenomena responsible for the formation of friction forces. Determining this scale is frequently a nontrivial problem because significant contributions to the friction force are related to processes simultaneously occurring on various levels. In particular, technical surfaces usually possess microroughnesses on different scales. Experimental investigations show that the surface of rails and asphalt road coatings, as well as many natural fracture surfaces, are self-similar in a broad range of wave vectors and can be classified as fractals [1–3].[1]

The aim of this paper was to study whether the observed macroscopic friction force can be used to reconstruct the microscopic interaction potential responsible for the friction force formation. The friction process will be considered within the framework of the generalized Tomlinson model [4], which, despite its simplicity, adequately describes many important features of the dry friction process. In numerous variants, this model has been extensively used in the physics of friction (see, e.g., [5–8]).

Let us consider the one-dimensional motion of a body in a periodic potential with viscous damping. The equation of motion in such a potential can be written as

$$m\ddot{x} = F - \eta\dot{x} - N\sin(2\pi x/a), \qquad (1)$$

where x is the coordinate, m is the mass of the body, F is the force acting upon the body, η is the damping factor, N is the amplitude of the periodic force, and a is the wavelength of the periodic potential. As was noted above, the Tomlinson model correctly describes many significant features of the dry friction process. Indeed, application of a sufficiently small force will lead only to a small displacement of the body from a potential energy minimum, after which the motion ceases. The force of counteraction is considered as the macroscopic static friction force. Evidently, equilibrium in a periodic potential in the presence of a constant tangential force cannot take place when this force exceeds a certain critical level that is considered as the macroscopic kinetic friction force: exceeding this threshold leads to macroscopic sliding of the body.[2] In model (1), the critical value of the force is N.

It can be shown that the dependence of the applied force F on the average sliding velocity, considered by a macroscopic observer as the "law of friction" in the system, is weakly sensitive to the period of the potential. For example, in the case of a large viscosity, the law of friction can be analytically calculated as

$$F = \sqrt{N^2 + (\eta\langle\dot{x}\rangle)^2}. \qquad (2)$$

As can be seen, this expression is independent of the spatial period of the potential. Therefore, reconstruction of the microscopic potential from the stationary friction force is principally impossible.

However, the situation changes substantially when a rapidly oscillating force is applied to the body together with the constant component or when a constant force is applied to a rapidly oscillating pair of bodies. Let us consider a model of such an oscillating tribosystem

[1] The surface of railway wheels and rails exhibit a fractal structure in a wavelength interval from 0.3 mm to 1 cm [2].

[2] By macroscopic behavior is implied the motion on a spatial scale significantly exceeding the period of the potential, while the scale determined by this period is referred to as microscopic.

1063-7850/04/3002-0148$26.00 © 2004 MAIK "Nauka/Interperiodica"

comprising two point masses coupled by a rapidly oscillating bond of length

$$l = l_0 + \Delta l \sin(\omega t) \tag{3}$$

and moving in a random potential $U = U(x)$ defined by the spectral expansion

$$U(x) = \int_0^\infty c(k)\cos(kx + \varphi_k)dk \tag{4}$$

in the presence of a constant external force F (see figure). Here, φ_k is the random phase assumed to be δ-correlated (white noise), so that

$$\langle \sin\varphi_k \sin\varphi_{k'}\rangle = \Phi\delta(k - k'). \tag{5}$$

The equation of motion for the center of mass of the two bodies can be written as

$$2m\ddot{x} = F - 2\eta\dot{x} - \frac{\partial U(x - l/2)}{\partial x} - \frac{\partial U(x + l/2)}{\partial x}. \tag{6}$$

Assuming that the bond oscillation frequency is much greater than the characteristic frequency of natural oscillations of the system in the potential $U(x)$, we may average Eq. (6) over the period of these rapid oscillations (this averaging will be indicated by the upper bar). Upon averaging, the "slow" motion component is described by the equation

$$2m\ddot{\bar{x}} = F - 2\eta\dot{\bar{x}} - \frac{\partial\overline{U(x - l(t)/2)}}{\partial x} - \frac{\partial\overline{U(x + l(t)/2)}}{\partial x}. \tag{7}$$

In the absence of a macroscopic motion, this yields

$$F = \frac{\partial\overline{U(x - l(t)/2)}}{\partial x} + \frac{\partial\overline{U(x + l(t)/2)}}{\partial x}. \tag{8}$$

This expression determines the macroscopically observed static friction force of the oscillating couple. Using expressions (3) and (4), we obtain

$$\overline{F(x)} = -\int_0^\infty c(k)k[\sin(k(x - l/2) + \varphi_k) + \sin(k(x + l/2) + \varphi_k)]dk = -2\int_0^\infty c(k)k\sin(kx + \varphi_k) \tag{9}$$

$$\times\left[\cos\frac{kl_0}{2}\cos\left(\frac{k\Delta l}{2}\sin\omega t\right) - \sin\frac{kl_0}{2}\sin\left(\frac{k\Delta l}{2}\sin\omega t\right)\right]dk.$$

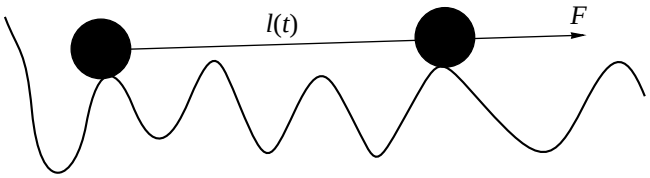

A model tribosystem of two bodies coupled by a bond of variable length $l(t)$ moving in a random potential.

Averaging this equation with respect to time and taking into account the well-known relations

$$\cos(\psi\sin\omega t) = J_0(\psi) + 2\sum_{k=1}^{\infty}(-1)^k J_{2k}(\psi)\cos(2k\omega t), \tag{10}$$

$$\sin(\psi\cos\omega t) = 2\sum_{k=0}^{\infty}(-1)^k J_{2k+1}(\psi)\cos((2k + 1)\omega t), \tag{11}$$

where $J_n(\psi)$ is the nth order Bessel function, we arrive at the formula

$$\overline{F(x)} = -2\int_0^\infty c(k)k\sin(kx + \varphi_k)\cos\frac{kl_0}{2}J_0\left(\frac{k\Delta l}{2}\right)dk. \tag{12}$$

For determining the maximum static friction force of the oscillating couple in the random potential, note that this force is a random function of the initial positions of the bodies. In other words, there is a certain function of distribution of the static friction force. This function can be determined only numerically. On the other hand, the average value of the static friction force is apparently of the same order of magnitude as the mean-square deviation of the force. Therefore, the main features of the dependence of the static friction force on the bond oscillation amplitude can be revealed by determining the average squared force acting upon the couple in the potential

$$\langle\overline{F(x)}^2\rangle = 2\int_0^\infty\int_0^\infty c(k)c(k')kk'\langle\sin(kx + \varphi_k)\sin(k'x + \varphi_{k'})\rangle \times\cos\frac{kl_0}{2}\cos\frac{k'l_0}{2}J_0\left(\frac{k\Delta l}{2}\right)J_0\left(\frac{k'\Delta l}{2}\right)dkdk', \tag{13}$$

where the angle brackets denote averaging over the ensemble. Taking in to account that, according to

Eq. (5), $\langle \sin(kx + \varphi_k)\sin(k'x + \varphi_{k'})\rangle = \Phi\delta(k - k')$, we obtain for the average squared force

$$\langle \overline{F(x)}^2 \rangle = \Phi \int_0^\infty c(k)^2 k^2 \cos^2 \frac{kl_0}{2} J_0^2\left(\frac{k\Delta l}{2}\right) dk. \qquad (14)$$

This expression can be further simplified in the case of a sufficiently large bond length l_0. If this bond length is "macroscopically large" (that is, exceeds any characteristic microscopic scale), the function $\cos^2\frac{kl_0}{2}$ in the integrand of Eq. (14) varies much faster than all other terms and can be replaced by the average value 1/2:

$$\langle \overline{F(x)}^2 \rangle = \frac{\Phi}{2} \int_{k_1}^{k_2} c(k)^2 k^2 J_0^2\left(\frac{k\Delta l}{2}\right) dk. \qquad (15)$$

Note that, in this case, the friction force is independent of the average bond length.

Now, let us consider how to use the dependence of the friction force on the oscillation amplitude Δl for reconstructing the spectral density $c(k)^2$ of the interaction potential. Here, the approach to solving this inverse problem will be considered on a qualitative level.

Note that, for large values of the argument, the Bessel function has the following asymptotic expression:

$$J_0(z) \approx \sqrt{\frac{2}{\pi z}} \cos\left(z - \frac{\pi}{4}\right).$$

Substituting this asymptotic expression into formula (15), we obtain

$$\begin{aligned} \langle \overline{F(x)}^2 \rangle &= \frac{2\Phi}{\pi\Delta l} \int_{k_1}^{k_2} c(k)^2 k \cos^2\left(\frac{k\Delta l}{2} - \frac{\pi}{4}\right) dk \\ &= \frac{\Phi}{\pi\Delta l} \int_{k1}^{k_2} c(k)^2 k[1 + \sin(k\Delta l)]dk. \end{aligned} \qquad (16)$$

Multiplying this equation by Δl and performing the inverse Fourier transform, we obtain the relation

$$\int_0^\infty \langle \overline{F(x)}^2 \rangle \Delta l \sin(k\Delta l) d(\Delta l) = \frac{\Phi}{2\pi^2} c(k)^2 k$$

from which the spectral density of the interaction potential can be determined as

$$c(k)^2 = \frac{1}{k} \frac{2\pi^2}{\Phi} \int_0^\infty \langle \overline{F(x)}^2 \rangle \Delta l \sin(k\Delta l) d(\Delta l). \qquad (17)$$

Thus, we have considered modification of the law of friction in the presence of a high-frequency excitation. The system under consideration can be experimentally realized as a pair of bodies coupled via a piezocrystal performing high-frequency oscillations. It was shown that, by measuring the static friction force as a function of the oscillation amplitude, it is possible to determine the spectral density of the interaction potential responsible for the friction force formation and, hence, to estimate the relative contributions to the friction related to processes on various scales of the system. These results provide a basis for the experimental determination of the characteristic scale of friction processes from the law of friction of oscillating tribosystems.

REFERENCES

1. B. N. J. Persson, F. Bucher, and B. Chiaia, Phys. Rev. B **65**, 184106 (2002).
2. F. Bucher, PhD Thesis (Tech. Univ., Berlin, 2002).
3. V. L. Popov, S. G. Psakh'e, E. V. Shil'ko, *et al.*, Fiz. Mezomekh. **5** (3), 17 (2002).
4. G. A. Tomlinson, Philos. Mag. **7**, 905 (1929).
5. B. N. J. Persson, *Sliding Friction: Physical Principles and Applications*, 2nd ed. (Springer-Verlag, New York, 2000).
6. V. Zaloj, M. Urbakh, and J. Klafter, Phys. Rev. Lett. **81**, 1227 (1998).
7. V. Zaloj, M. Urbakh, and J. Klafter, Phys. Rev. Lett. **82**, 4823 (1999).
8. V. L. Popov, Solid State Commun. **115**, 369 (2000).
9. A. Barone and G. Paterno, *Physics and Applications of the Josephson Effect* (Wiley, New York, 1982; Mir, Moscow, 1984).

Translated by P. Pozdeev

Technical Physics Letters, Vol. 30, No. 2, 2004, pp. 151–153. Translated from Pis'ma v Zhurnal Tekhnicheskoĭ Fiziki, Vol. 30, No. 4, 2004, pp. 49–54.

Synthesis and Magnetic Properties of Nickel Nanoparticles in Magnesium Fluoride Matrix

A. L. Stepanov[a,b,*], R. I. Khaibullin[b,c], B. Z. Rameev[b,c], A. Reinholdt[a], and U. Kreibig[a]

[a] *Institute of Physics 1A, Aachen Technical University, 52056 Aachen, Germany*

[b] *Kazan Physicotechnical Institute, Russian Academy of Sciences, Kazan, 420029 Tatarstan, Russia*

[c] *Gebze Technological Institute, 41400 Gebze, Turkey*

* *e-mail: anstep@kfti.knc.ru*

Received July 24, 2003

Abstract—A new composite material, comprising a diamagnetic matrix (magnesium fluoride) containing metal nanoparticles (nickel), has been synthesized in a high-vacuum laser-based universal cluster ablation system. The structure and magnetic properties of the composite were studied by transmission electron microscopy (TEM) and ferromagnetic resonance (FMR). According to TEM data, the nickel nanoparticles have a spherical shape and their dimensions are described by a narrow distribution function with an average value of 3.2 nm. An analysis of the FMR spectra reveals strong interaction between nickel nanoparticles in the composite, which accounts for an out-of-plane magnetic anisotropy and suggests the formation of granular magnetic films. © *2004 MAIK "Nauka/Interperiodica".*

Composite systems representing a homogeneous diamagnetic matrix containing dispersed magnetic nanoparticles are promising materials for magnetoelectronics, data storage systems, and other applications. The magnetic properties of such composites can be controlled within broad limits by varying the average nanoparticle size, distribution function, packing factor, and composition of the magnetic inclusions and surrounding diamagnetic medium. The search for new and development of the existing technologies of obtaining composite materials with controlled structural and magnetic characteristics is a currently important task.

Below, we describe a new method for the synthesis of nanostructured composite materials. The method was used to obtain Ni/MgF_2 composites comprising nickel nanoparticles with a narrow size distribution dispersed in a diamagnetic matrix of magnesium fluoride. Besides, we present preliminary data on the structure and magnetic properties of this system.

The nanoparticles of nickel in a MgF_2 matrix were synthesized in a high-vacuum laser-based universal cluster ablation system (LUCAS) described in detail elsewhere [1, 2]. The vacuum chamber of LUCAS, originally intended for the formation of cluster beams of low-melting metals such as silver [3], was upgraded and equipped with a pulsed Nd:YAG laser (Lumonics JK 702H with a wavelength of 1.064 μm in the IR range) to operate with high-melting metals. Using this high-power laser, atomic nickel vapor was obtained by laser ablation of a bulk chemically pure Ni target in the working chamber filled with argon to a pressure of 0.6 bar. The target was ablated by 500 identical laser pulses with an energy density of ~4.7 J/cm^2, a pulse duration of 1 ms, and a repetition frequency of 80 Hz.

A mixture of the laser-generated metal vapor with Ar molecules was ejected from a narrow (1.2 mm in diameter) nozzle into the deposition chamber. The beam was driven by an adiabatic pressure difference created by a turbomolecular pump. The pressure in the deposition chamber was maintained at a level of ~10^{-7} mbar, which provided for a stable flow of the vapor–gas mixture through the nozzle. Adiabatic expansion of the mixture led to the rapid cooling of nickel vapor and the nucleation of Ni nanoparticles, the beam of which could be directed to and deposited onto substrates. In our experiments, the samples were prepared on quartz substrates preliminarily covered with a 50-nm-thick layer of MgF_2. The layer of deposited Ni nanoparticles was coated with a protective film of MgF_2 deposited by electron beam sputtering of a bulk target. The magnesium fluoride film prevented nickel nanoparticles from oxidation upon extraction of the samples from vacuum chamber into the atmosphere.

For the investigation of samples by transmission electron microscopy (TEM), the beam of nickel nanoparticles was deposited onto a thin carbon film supported on a copper grid. The TEM measurements were performed in a Philips EM 400T instrument. The magnetic properties of Ni/MgF_2 composites were studied by room-temperature ferromagnetic resonance (FMR) spectroscopy. The FMR spectra were obtained using an X-band (9.5 GHz) EPR spectrometer (Bruker EMX). The measurements were performed for various orientation of the sample plane relative to the direction of the static magnetic field (H). The spectra were recorded in

1063-7850/04/3002-0151$26.00 © 2004 MAIK "Nauka/Interperiodica"

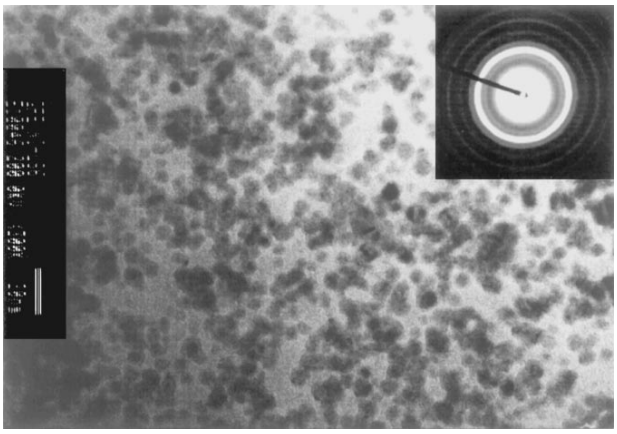

Fig. 1. TEM micrograph and the electron microdiffraction pattern of Ni nanoparticles synthesized in the LUCAS setup.

the conventional form of the first derivative of the absorbed RF power (dP/dH) as a function of the applied magnetic field, and the resonance field H_0 was determined at the point of intersection of the dP/dH curve with the zero line.

Figure 1 shows the typical TEM micrograph of Ni nanoparticles (dark spots on bright background) synthesized in the LUCAS setup by method of laser ablation followed by adiabatic expansion of the metal vapor. As can be seen from this figure, the proposed method allows spherical crystalline metal nanoparticles of nearly the same size to be deposited on various substrates. A histogram of the particle size distribution (not presented here) shows that the average particle size is 3.2 nm. The size distribution function is close to the normal Gaussian distribution with a halfwidth of σ = 2.2 nm. It should be noted that the particle size dispersion σ is significantly smaller as compared to that observed for the nickel nanoparticles formed by different methods, for example, by the sol–gel method in glass or by chemical deposition from a nanocolloidal solution on various substrates [4].

The FMR measurements of Ni/MgF_2 composites revealed an intense response at room temperature. Figure 2 presents the FMR spectra measured for various values of the polar angle θ between the normal to the sample plane and the direction of the applied magnetic field. As can be seen from these data, an increase in θ leads to a monotonic shift of the resonance signal from the high- to low-field region of the spectrum, which is accompanied by changes in the signal width and shape. As expected for the given geometry of deposition, the signal parameters were independent of the azimuthal angle; that is, thin films of Ni/MgF_2 exhibit only an out-of-plane anisotropy of the "easy plane" type.

The observed FMR spectra and the angular dependences of the signal parameters (Fig. 3) are characteristic of the FMR spectra of thin granular magnetic films [5]. Thus, the results of our magnetic measurements confirm the presence of magnetic Ni nanoparticles dispersed in a thin layer of MgF_2. The angular anisotropy is indicative of a strong dipole–dipole interaction between the nanoparticles. The FMR data can be interpreted using an approximation of effective magnetic medium [4–7]. According to this, the Ni/MgF_2 composite is considered as a continuous magnetic medium with a homogeneous "effective" magnetization (M_{eff}) and an "effective" g value (g_{eff}). The best fit of the theory to the experimental resonance field values for various sample orientations (defined by polar angle θ) was obtained

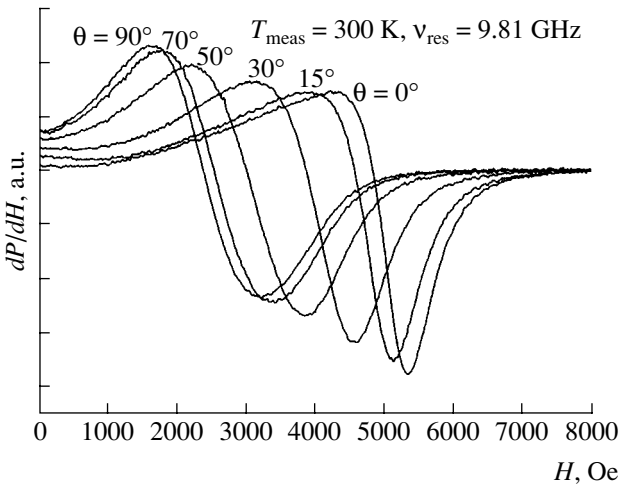

Fig. 2. FMR spectra of a Ni/MgF_2 composite film measured for various polar angles θ (measured at T = 300 K; ν_{res} = 9.81 GHz).

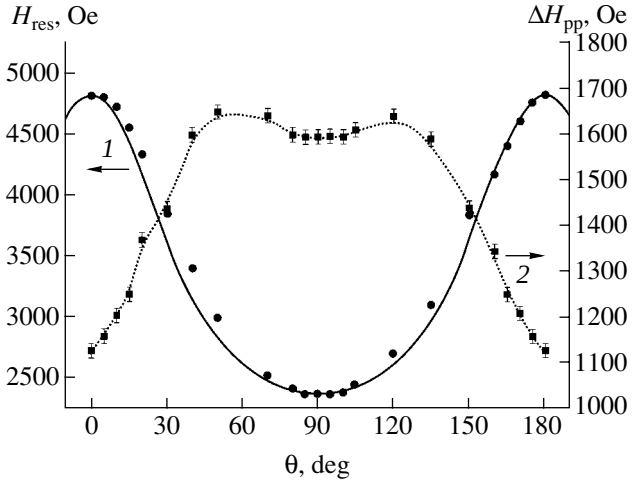

Fig. 3. Plots of (*1*) the FMR field H_{res} and (*2*) peak-to-peak FMR signal width ΔH_{pp} versus polar angle θ for a Ni/MgF_2 composite film. Solid curve is a fit obtained in a model of effective medium [5] with the parameters M_{eff} = 136 G and g_{eff} = 2.25.

for a model with the parameters M_{eff} = 136 G and g_{eff} = 2.25.

To summarize, laser ablation of a nickel target followed by adiabatic expansion of the metal vapor in a narrow nozzle was used to synthesize nickel nanoparticles with close dimensions and to obtain for the first time a thin-film Ni/MgF_2 composite. The FMR spectra of this composite were measured and the room-temperature effective magnetization, *g*-factor values, and magnetic anisotropy were determined.

Acknowledgments. A.L.S. is grateful to the Alexander Humboldt Foundation for the financial support of his work in Germany. R.I.K. acknowledges support by NATO-TUBITAK PC-B Fellowship Programme (Turkey).

This study was sponsored in part by the Federal Program for Support of the Leading Scientific Schools of Russia (project no. NSh-1904.2003.2) and Deutsche Forschungsgemeinschaft.

REFERENCES

1. A. L. Stepanov, G. Bour, M. Gartz, *et al.*, Vacuum **64**, 9 (2001).
2. A. L. Stepanov, M. Gartz, G. Bour, *et al.*, Vacuum **67**, 223 (2002).
3. A. Hilger, M. Tenfelde, and U. Kreibig, Appl. Phys. B **73**, 361 (2001).
4. F. C. Fonseca, G. F. Goya, R. F. Jardim, *et al.*, Appl. Phys. A **76**, 621 (2003).
5. S. H. Wu and D. H. Chen, J. Colloid Interface Sci. **259**, 282 (2003).
6. G. N. Kakazei, A. F. Kravets, N. A. Lesnik, *et al.*, J. Appl. Phys. **85**, 5654 (1999).
7. D. L. Griscom, J. J. Krebs, A. Perez, and M. Treilleux, Nucl. Instrum. Methods Phys. Res. B **32**, 272 (1988).

Translated by P. Pozdeev

Technical Physics Letters, Vol. 30, No. 2, 2004, pp. 154–156. Translated from Pis'ma v Zhurnal Tekhnicheskoĭ Fiziki, Vol. 30, No. 4, 2004, pp. 55–61.

The Axial Propagation of Plasma upon Radial Injection in a Current Interrupter

B. M. Koval'chuk and A. A. Zherlitsyn*

Institute of High-Current Electronics, Siberian Division, Russian Academy of Sciences, Tomsk, Russia

** e-mail: andzh@oit.hcei.tsc.ru*

Received July 22, 2003

Abstract—The axial propagation of plasma in a current interrupter with radial injection guns has been experimentally studied. In the absence of a generator current passing through the injected plasma, the plasma front with a density of no less than 10^{11} cm^{-3} moves in the axial direction at a velocity of ~(1–1.5) × 10^7 cm/s. At a distance of 20 cm from the injection plane, a plasma density of ~10^{13} cm^{-3} is attained 5–6 μs after the current switch on in the guns; at a distance of 50 cm, the plasma density reaches ~(2–5) × 10^{12} cm^{-3}. © *2004 MAIK "Nauka/Interperiodica".*

When plasma is injected into a coaxial current interrupter of the plasma-opening switch (POS) type from the side of the outer conductor, the plasma front propagates in both radial and axial directions from the site of injection. Plasma guns of the cable type [1] produce a high-density plasma in the central channel of the cable, and it is the axial propagation of the plasma front that can determine both the POS size and the plasma density gradient in the axial direction. These parameters influence the current interrupter functioning both in the conduction stage and in the high-voltage state.

In order to study the axial propagation of plasma upon radial injection, we performed experiments on the GIT-4 generator [1] using a system with radial injection cable guns and a cone-shaped central conductor. Current interrupters of this type can be used both as switches in a system with the load connected prior to POS [2, 3] and as plasma-filled diodes for current switching along the system axis.

Methods for monitoring plasma propagation and evaluating the plasma density. The plasma propagation was monitored by measuring the current in the circuit of a negatively-biased collector placed in the POS region. By applying a dc voltage, it is possible to evaluate the axial propagation velocity and estimate the plasma density at the moment the plasma front reaches the collector. A pulsed voltage applied to the collector allows the plasma density to be determined at the given site at an arbitrary moment by varying the delay time between the voltage pulse application and the plasma gun shot moment.

If the collector potential provides for the surface screening from electrons of the plasma and there is no emission from the collector, the current in the collector circuit is determined only by the ion component,

$$I_c = keZnSv_p, \quad (1)$$

where Z is the ion charge, S is the collector, v_p is the velocity of the ion flux toward the collector, and k is a factor taking into account the ion-induced electron emission. For approximate calculations, the ion-induced electron emission coefficient can be taken equal to ~1, which yields $k = 2$.

The interaction of plasma with the collector may lead to the formation of cathode spots. In the approximation of unlimited emission from the collector, the electron and ion current components in the layer obey the Langmuir relation and the total current can be expressed as

$$I_c \approx eZnSv_p\sqrt{\frac{M_i}{Zm_e}}. \quad (2)$$

Relations (1) and (2) can be used for evaluation of the plasma density from the measured current I_c, assuming the plasma to consist predominantly of H^+ and C^{2+} ions.

Experimental. The experimental arrangement is illustrated in Fig. 1. The external conductor *1* with a diameter of 208 mm bears 32 polyethylene cable guns *2* injecting plasma in the radial direction. The central conductor *3* has a cone shape with a diameter of 76 mm in the plasma injection region. Collector *4* with a diameter D is placed at a distance L from the gun section. The plasma guns were power supplied from a pair of capacitors (IK 50-3). The gun discharge current has a periodic shape with the first half-period amplitude of about 8 kA and a duration of ~2.3 μs. The system was evacuated with turbomolecular pumps to a residual pressure of ~3 × 10^{-5} Torr.

Measurements with a dc bias voltage on the collector. In this series of experiments, a negative dc voltage from a capacitor with $C_0 = 2$ μF was applied to the

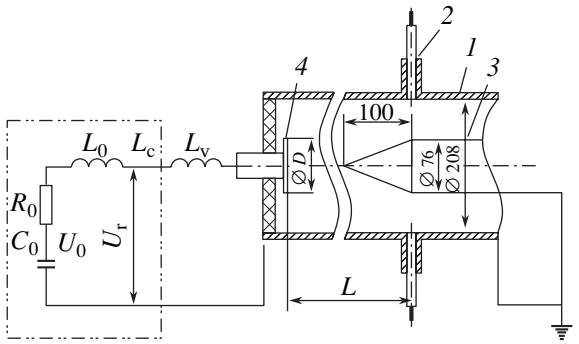

Fig. 1. Experimental arrangement for the investigation of axial propagation of plasma upon radial injection in a plasma-opening switch (see the text for explanations).

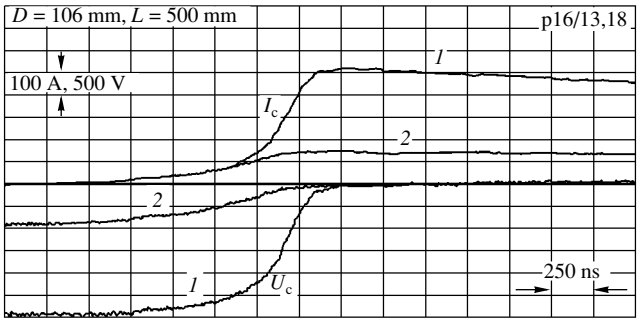

Fig. 2. Typical oscillograms of the collector current I_c and voltage U_c measured with dc bias from a capacitor charged to (*1*) 3 kV and (*2*) 1 kV.

collector. The bias voltage was varied from 0.5 to 4 kV and the discharge current I_c in the shunted collector circuit was measured. In the short-circuit regime, the time to maximum current in the circuit with a ballast resistor $R_0 = 5.5\ \Omega$ was ~160 ns.

For $L = 200$ mm, the current in the collector circuit appeared ~1 μs after switching on the plasma gun current and rapidly, in ~1.5 μs, reached an amplitude corresponding to the short-circuit regime. When the distance L was increased to 500 mm, the collector current I_c appeared with a 3.8 μs delay. Using the time to appearance of the collector current I_c at a given distance to collector, the average velocity of the axial motion of the plasma front can be estimated as $\sim 1.5 \times 10^7$ cm/s. The time to appearance of the collector current remained unchanged for an eightfold variation of the bias voltage (0.5 to 4 kV). Therefore, the electric field of the collector did not significantly influence the axial motion of the plasma.

Figure 2 shows oscillograms of the collector current I_c and the calculated curves of the collector voltage U_c for a collector with $D = 106$ mm positioned at $L = 500$ mm and biased by the capacitor charged to 3 and 1 kV. The current oscillograms exhibit two characteristic regions. The initial low-sloping portion is apparently related to the ion component. In this region, the current is weakly dependent on the applied voltage in the entire range from 0.5 to 4 kV and is determined by the ion concentration. This behavior is described by Eq. (1), which allows the plasma density to be estimated as $\sim 2 \times 10^{11}$ cm^{-3} for the hydrogen plasma and $\sim 10^{11}$ cm^{-3} for the carbon plasma.

The subsequent sharp increase in the current reflects the emission of electrons from cathode plasma. At a maximum current I_c, the collector voltage U_c is close to zero and the current amplitude is determined by the ballast resistor in the bias circuit rather than by the ion flux to collector. When the collector diameter was decreased to 20 mm, the initial low-sloping portion disappeared, but the current amplitude was still determined by the ballast resistor. For the maximum current, Eq. (2) gives a plasma density at the collector of no less than $\sim 1.5 \times 10^{12}$ cm^{-3} and 3×10^{11} cm^{-3} for the hydrogen and carbon plasma, respectively.

Measurements with a pulsed bias voltage on the collector. In order to provide for the regime of ion current saturation and completely exclude the influence of the electric field on the plasma propagation, the collector was biased in pulsed regime using a GIT-4 generator. The generator was switched on with a certain delay t_d relative to the plasma gun operation time. The parameters of the GIT-4 were as follows: the primary store capacitance, $C_0 = 4.8$ μF; the intrinsic inductance, $L_0 = 109$ nH; the output voltage, $U_0 = -480$ kV. The discharge current was measured using the Rogovsky coil, and the output voltage U_r was measured using an active voltage divider. The inductance between generator and collector was $L_v \sim 120$ nH. The measurements in the pulsed bias regime were performed for a collector with the diameter $D = 160$ mm, located 200 and 500 mm from the injection plane.

For the collector at $L = 200$ mm and a delay time below $t_d = 2.8$ μs, the generator almost immediately started operating in the free-running mode and the initial portion of the current profile was virtually absent. The current measured in this regime was ~25 kA, for

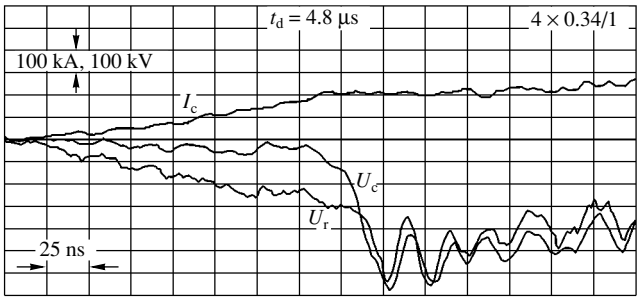

Fig. 3. Typical oscillograms of the collector current I_c and voltage U_c and the generator output voltage U_r measured with a pulsed bias for a pulse delay time of $t_d = 4.8$ μs.

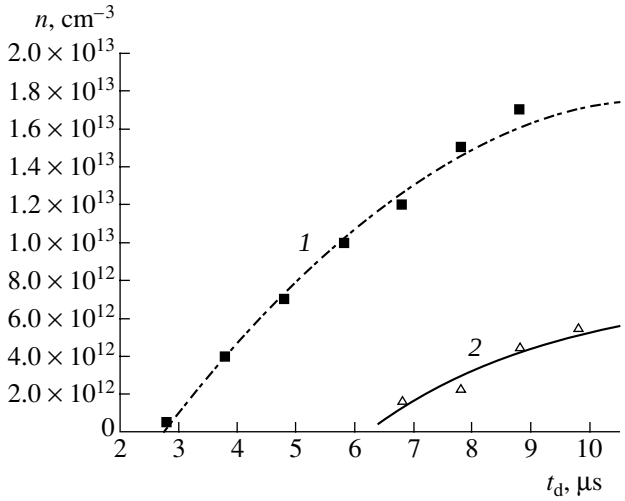

Fig. 4. The plots of plasma density n versus pulse delay time t_d calculated (for C^{2+} ions) using the results of measurements with the collector spaced by L = (*1*) 200 and (*2*) 500 mm from the plasma injection plane.

which Eq. (2) yields a plasma density of ~10^{12} cm^{-3} at a velocity of 5×10^6 cm/s. Therefore, we may ascertain that, for t_d = 2.8 μs, the plasma density at the collector does not exceed ~10^{12} cm^{-3}. Figure 3 shows oscillograms of the discharge current I_c, the output generator voltage U_r, and the calculated collector voltage $U_c = U_r - L_v(dI_c/dt)$ for a gun shot with t_d = 4.8 μs and the collector at L = 200 mm. For this delay, the generator is loaded on a plasma-filled diode. As the current grows to 200 kA, the ion component exhibits saturation that is accompanied by a sharp drop of U_c. The plasma density for C^{2+} ions estimated from relation (2) is ~0.7 × 10^{13} cm^{-3}; for a plasma consisting predominantly of hydrogen ions, the density is about five times as high. Allowance for the intrinsic magnetic field of electrons leads to even higher estimates of the plasma density. Figure 4 shows the plots of plasma density versus delay time calculated (for C^{2+} ions) using the results of measurements with the collector spaced L = 200 and 500 mm from the injection plane. Note that removal of the central cone-shaped conductor from the plasma injection zone did not change the behavior of $n(t_d)$.

Conclusions. The results of our experiments show that, in the absence of the generator current through the injected plasma, the plasma front with a density of no less than 10^{11} cm^{-3} moves in the axial direction at a velocity of ~$(1–1.5) \times 10^7$ cm/s. The time of appearance of the plasma with a concentration above 5×10^{12} cm^{-3} corresponds to an average plasma propagation velocity of ~5×10^6 cm/s. At a distance of 20 cm from the injection plane, a plasma density of ~10^{13} cm^{-3} is attained 5–6 μs after the current switch on in the guns; at a distance of 50 cm, the plasma density reaches ~$(2–5) \times 10^{12}$ cm^{-3}.

REFERENCES

1. S. P. Bugaev, A. M. Volkov, A. M. Iskol'dsky, *et al.*, IEEE Trans. Plasma Sci. **18** (5), 115 (1990).
2. A. N. Bastrikov, A. A. Kim, B. M. Kovalchuk, *et al.*, in *Proceedings of the 12th IEEE Pulsed Power Conference, Monterey, 1999*, pp. 1191–1194.
3. A. N. Bastrikov, A. A. Zherlitsyn, A. A. Kim, *et al.*, Izv. Vyssh. Uchebn. Zaved. Fiz., No. 12, 31 (1999).

Translated by P. Pozdeev

Technical Physics Letters, Vol. 30, No. 2, 2004, pp. 157–160. Translated from Pis'ma v Zhurnal Tekhnicheskoĭ Fiziki, Vol. 30, No. 4, 2004, pp. 62–70.

An Effective Compact Analyzer of Electron Spin Polarization

V. N. Petrov*, V. V. Grebenshikov, B. D. Grachev, A. S. Kamochkin, and M. K. Yarmarkin

St. Petersburg State Technical University, St. Petersburg, 195251 Russia

** e-mail: Petrov@tuexph.stu.neva.ru*

Received June 5, 2003

Abstract—A compact electron polarimeter employing the classical Mott scheme has been developed and tested. The device has an efficiency of about 5.6×10^{-4}, a maximum count rate of 5×10^5 cps, dimensions 15 cm (diameter) × 25 cm (length), and a working voltage of 40 kV. The polarimeter can operate for a long time under arbitrary vacuum conditions without maintenance, exhibiting no changes in the main working characteristics, and obeys all requirements to the electron spin polarization studies on the modern level. © *2004 MAIK "Nauka/Interperiodica".*

Introduction. The electron beam spin polarization is most frequently measured using the phenomenon of Mott scattering [1–9]. Below, we describe a new classical electron spin polarimeter employing this scheme, developed by the Surface Magnetism Group at St. Petersburg State Technical University.

Using the Mott polarimeter, the electron beam polarization is determined by measuring the asymmetry of electron backscattering from a gold foil,

$$A = (N_L - N_R)/(N_L + N_R), \quad (1)$$

with an absolute statistical error of

$$\Delta A = 1/\sqrt{N_L + N_R}. \quad (2)$$

Here, N_L and N_R are the numbers of electrons counted in the left and right detector channels, respectively (see Fig. 1). The electron beam polarization is defined as

$$P = A/S_{eff}, \quad (3)$$

where S_{eff} is the effective Sherman function representing the asymmetry measured for a completely polarized beam (100% electron polarization). The absolute statistical error of the polarization determination is calculated as

$$\Delta P = 1/S_{eff}\sqrt{N_L + N_R} = 1/\sqrt{\varepsilon N_0}, \quad (4)$$

where N_0 is the number of electrons at the polarimeter entrance and ε is the Mott polarimeter efficiency given by the formula

$$\varepsilon = S_{eff}^2(N_L + N_R)/N_0. \quad (5)$$

The new Mott polarimeter was designed so as to meet the following requirements:

(i) The device must possess maximum possible efficiency.

(ii) The measured value of polarization has to correspond to the "true" electron polarization and must be independent of the beam shape and position (i.e., of the factors leading to the so-called spurious asymmetry).

(iii) The polarimeter has to be ready to operate within a few minutes after switching on, requiring nei-

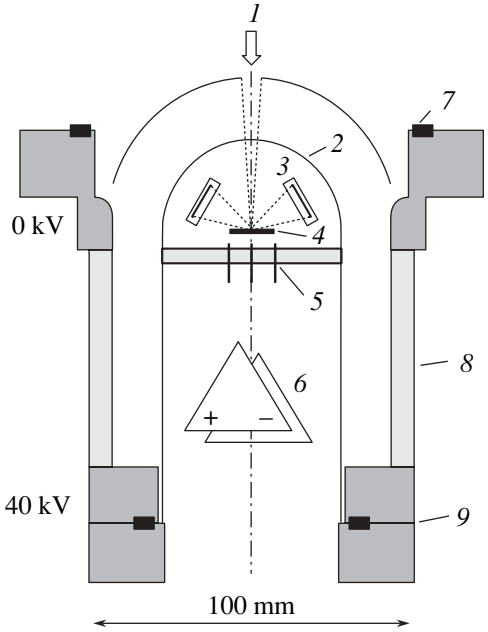

Fig. 1. Schematic diagram of the Mott polarimeter: (*1*) primary electron beam; (*2*) hemispheres; (*3*) four PIPS detectors; (*4*) gold foil; (*5*) vacuum feedthrough; (*6*) four preamplifiers; (*7*) 100-mm flange (CF 100); (*8*) ceramic insulator; (*9*) 63–mm flange (CF 63).

1063-7850/04/3002-0157$26.00 © 2004 MAIK "Nauka/Interperiodica"

ther start-up procedures nor any adjustments during operation. The instrument should be capable of operating for many years under arbitrary vacuum conditions, including ultrahigh vacuum (UHV), exhibiting no changes in the main working characteristics.

(iv) The device has to be sufficiently compact for mounting on a standard 100-mm flange (CF 100).

In order to satisfy all these conditions, we selected the classical Mott polarimeter scheme. A special feature of the classical scheme is that backscattered electrons travel in a field-free space, in contrast to some other Mott polarimeters where the scattered electrons move in a retarding potential. Previously [10], we showed that the Mott polarimeters with retarding fields are much more sensitive to variations in the beam parameters and only the classical scheme provides for the required stability and ensures that the results of polarization measurements are independent of changes in the beam parameters.

As is known, electrons scattered from a gold film in the classical Mott polarimeter have to be selected by energy-sensitive detectors. Previously used large-area surface barrier detectors with preamplifiers were characterized by a low resolution and a high noise level. This hindered separation of the useful signal from noisy background at an electron energy significantly below 100 keV. For this reason, the classical Mott polarimeters of the previous generations operated at a high voltage (on the order of 100 kV) and, accordingly, had large dimensions. At present, so-called passivated implanted planar silicon (PIPS) detectors with small reverse currents are available. Using these detectors and new low-noise transistors, we have developed more effective electronic circuitry that allowed the working voltage to be reduced down to 40 keV and the whole device to be arranged in a compact case.

Detector design. For developing the new device, a good basis was provided by our classical Mott polarimeter, which was created about five years ago and proved to be an effective, reliable, and stable instrument [11–13]. The new system design essentially reproduces the old solution on a smaller scale with a single ceramic insulator.

Figure 1 shows a schematic diagram of the new Mott polarimeter. The main device components are two concentric polished metal hemispheres with the radii of 30 and 50 mm. The outer hemisphere occurs at the ground (or close) potential, while the inner hemisphere is biased to 40 kV. The inner hemisphere is mounted on a ceramic insulator with a rated breakdown voltage of 60 kV. An electron beam to be studied with respect to polarization passes via a round hole in the outer electrode and enters the space between hemispheres, where electrons are accelerated in a strong electric field between the concentric electrodes to reach the entrance hole in the inner hemisphere. Calculations of the electron trajectories showed that the field between hemispheres ensures good focusing of the primary beam. Under the inner hemisphere, there are four PIPS detectors (each with a working area as large as ~1 cm^2) and a scattering foil comprising an 800-Å-thick gold film deposited onto a thin Formvar substrate. Electrons scattered from the foil move in a field-free space to strike the PIPS detectors.

An analysis of the asymmetry of electron backscattering is combined with energy selection of the secondary electrons, since the maximum asymmetry is known to be reached in the case of elastic scattering. This is related to the fact that inelastic scattering leads to the loss of information about the electron spin and, hence, to a decrease in the measured asymmetry. In the proposed Mott polarimeter, the energy selection is performed using the PIPS detectors with the output pulse amplitude proportional to the incident electron energy. After the amplification and discrimination of pulses on a certain preset level, the pulse count rate can be considered as proportional to the number of electrons elastically scattered per unit time.

As was noted above, special preamplifiers have been developed for the operation with PIPS detectors so as to provide for the high counting rate. Each preamplifier includes a charge-sensitive circuit, a voltage amplifier, a quasi-Gaussian signal shaper, and the output circuit representing an active low-frequency filter with the Bessel transmission function characteristic [14]. All circuits occur at a high voltage (~40 kV). On the side of atmospheric pressure, the Mott polarimeter is connected to an aluminum case (also occurring at a high voltage) containing discriminators, a transformer, and ±5- and +50-V voltage sources. These voltages are formed from an ac signal of ~7 V amplitude supplied via two high-voltage cables in a common sheath from the 40-kV voltage source. The Mott polarimeter is 25 cm long and 15 cm in diameter. By means of a special fiber-optic system, the output signals are transmitted to the input of an optical signal receiver (occurring at a ground potential) for subsequent processing.

Mott polarimeter testing. In the first stage, the new Mott polarimeter was tested with respect to high-voltage breakdown. Preliminary calculations showed that the breakdown can be expected at a voltage of ~60 kV. During this test, the device was kept for several hours at an applied voltage of 55 kV. No high-voltage breakdowns were observed. Subsequent working tests were performed at a voltage of 40 kV.

In the second stage, the electronic circuitry was tested with respect to the signal-to-noise ratio. For this purpose, the electron count rate in each channel was measured as a function of the discrimination level and then this function was differentiated. The derivative plot showed clear separation of noise from the useful signal. Selection of the proper discrimination level ensured a 100% efficiency of the collection of electrons elastically scattered from gold. The intrinsic noise of the electronic circuitry corresponded to a count rate of about 1 count per second (cps).

In the third stage, the Mott polarimeter was calibrated so as to determine the effective Sherman function and the electron scattering coefficient $(N_L + N_R)/N_0$. Previously [11], it was shown that the classical Mott polarimeter can be calibrated in the first approximation by extrapolating signal to a high discrimination level. This calibration method is based on the fact that the measured amplitude spectrum is determined by a convolution of the real electron spectrum with the instrumental transmission (the energy resolution of the polarimeter–preamplifier complex). Therefore, the asymmetry on a high discrimination level is determined only by the elastically scattered electrons. This approach is analogous to that used in the Mott polarimeters with retarding field, where the extrapolation is performed to the level of zero electron energy losses [15].

The calibration procedure requires that the source of polarized electrons be highly stable, even at the expense of small and unknown polarization. We employed a polarized electron source based on the scattering of a nonpolarized electron beam from the (110) surface of an $FeNi_3$ magnetic single crystal. According to the scheme of this experiment described in [10], the scattering single crystal was irradiated by a beam of 500-eV nonpolarized electrons from a gun oriented at an angle of 90° relative to the Mott polarimeter axis, while the scattering plane was horizontal. The crystal had the shape of a square frame with the sides oriented along the easy axes. Using a coil of seven turns wound around one side, the working side of the frame was magnetized in the vertical direction perpendicular to the scattering plane. The secondary electrons were directed without any energy selection to the Mott polarimeter entrance with the aid of a simple two-electrode optics.

It was found that clean $FeNi_3$ crystal surface is sensitive to contamination, but contaminated surface of the crystal produced a beam of secondary electrons with small but highly stable polarization, which remained constant over a time period of several tens of hours. In order to exclude the possible errors related to the asymmetry caused by the spin–orbit interaction and the instrumental asymmetry, the calibration cycle was always performed so as to measure the hysteresis loop (Fig. 2). The hysteresis loop with a zero coercive force was evidence of magnetic origin of the asymmetry. The time required for recording a loop presented in Fig. 2 (with the indicated statistical error at a count rate of 400 kHz) was about 12 min.

In order to determine the effective Sherman function by this calibration procedure [11], we have studied the asymmetry of scattering as a function of the discrimination level. For the working discrimination level, the asymmetry was 0.21%. As the discrimination level was increased, the asymmetry exhibited a growth with saturation on a level of 0.45%. As was noted above, this variation is related to a decrease in the number of inelastically scattered electrons. At a sufficiently high

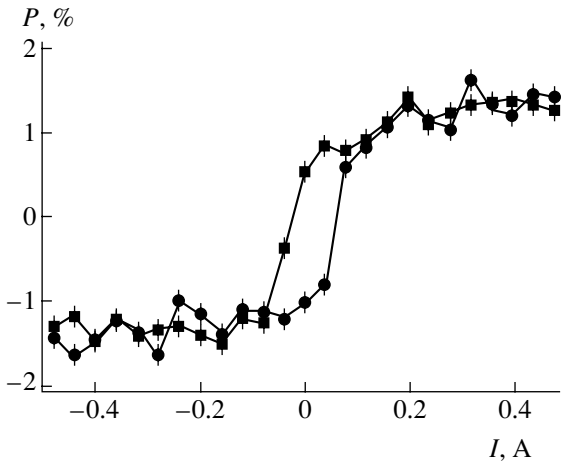

Fig. 2. Plots of the polarization P with a hysteresis loop obtained by the spin polarization analysis of secondary electrons scattered from an $FeNi_3(110)$ single crystal magnetized by the field of a coil with a current I.

discrimination level, only elastically scattered electrons are detected. Since the primary electron beam polarization remained unchanged, the observed variation of the scattering asymmetry was proportional to a change in the Sherman function. The effective Sherman function S_{eff} corresponding to the asymmetry of elastically scattered fully polarized electron beam was calculated using the atomic data. For the given experimental geometry, we obtained $S_{eff} = 0.32$ [16]. For the working discrimination level, the effective Sherman function was estimated as $S_{eff} = 0.32 \times 0.21/0.45 = 0.15$.

For determining the electron scattering coefficient $(N_L + N_R)/N_0$, the polarimeter unit comprising four PIPS detectors and the gold foil was replaced by an analogous unit containing only an electron detector mounted on the foil site. This procedure involves air admission but, since it only requires changing units on the standard 63-mm flange (CF 63), the total time of replacement and evacuation to a high vacuum (10^{-7} Pa) is relatively short. This experiment was multiply repeated and the count rates in the units with the polarimeter or detector were determined for the identical parameters of the electron gun. The value of $(N_L + N_R)/N_0$ on the working discrimination level (50 rel. units) was ~0.025, and the polarimeter efficiency determined by formula (5) was $\varepsilon = 5.6 \times 10^{-4}$. At present, this is a record value for the Mott polarimeters.

Conclusions. A new, compact and highly effective electron spin polarization analyzer was created based on the classical field-free Mott polarimeter scheme. The device meets all requirements to the electron spin polarization studies on the modern level. The polarimeter can operate under arbitrary vacuum conditions and is UHV compatible. The working parameters of the device are stable during long-term operation, requiring no control or maintenance. The polarimeter operates at

a working voltage of 40 kV and has an efficiency of 5.6×10^{-4}.

Acknowledgments. This study was supported by the INTAS Foundation, grant no. 01-0386.

REFERENCES

1. N. F. Mott and H. S. W. Massey, *The Theory of Atomic Collisions*, 3rd ed. (Clarendon Press, Oxford, 1965; Mir, Moscow, 1969).
2. J. Kessler, *Polarized Electrons*, 2nd ed. (Springer-Verlag, Berlin, 1985; Mir, Moscow, 1988).
3. D. F. Nelson and R. W. Pidd, Phys. Rev. **114**, 728 (1959).
4. M. Kalisvaart, M. R. O'Neill, T. W. Riddle, *et al.*, Phys. Rev. B **17**, 1570 (1978).
5. L. G. Gray, M. W. Hart, F. B. Dunning, and G. K. Walters, Rev. Sci. Instrum. **55**, 88 (1984).
6. M. Landolt, R. D. Allenspach, and D. Mauri, J. Appl. Phys. **57**, 3626 (1985).
7. F. B. Danning, L. G. Gray, J. M. Ratliff, *et al.*, Rev. Sci. Instrum. **58**, 1706 (1987).
8. M. Getzlaff, J. Bansmann, and G. Schoenhense, J. Magn. Magn. Mater. **131**, 304 (1994).
9. S. Qiao, A. Kimura, A. Harasawa, *et al.*, Rev. Sci. Instrum. **68**, 4390 (1997).
10. V. N. Petrov, M. S. Galaktionov, and A. S. Kamochkin, Rev. Sci. Instrum. **72**, 3728 (2001).
11. V. N. Petrov, M. Landolt, M. S. Galaktionov, and B. V. Yushenkov, Rev. Sci. Instrum. **68**, 4385 (1997).
12. C. Stamm, F. Marty, A. Vaterlaus, *et al.*, Science **282**, 449 (1998).
13. M. Hoesch, T. Greber, V. N. Petrov, *et al.*, J. Electron Spectrosc. Relat. Phenom. **124**, 263 (2002).
14. P. Horowitz and W. Hill, *The Art of Electronics*, 2nd ed. (Cambridge Univ. Press, New York, 1989; Mir, Moscow, 1984), Vol. 1, p. 259.
15. T. J. Gay, M. A. Kahkoo, J. A. Brand, *et al.*, Rev. Sci. Instrum. **63**, 114 (1992).
16. G. Holswarth and H. J. Meister, Nucl. Phys. **59**, 56 (1964).

Translated by P. Pozdeev

Technical Physics Letters, Vol. 30, No. 2, 2004, pp. 161–163. Translated from Pis'ma v Zhurnal Tekhnicheskoĭ Fiziki, Vol. 30, No. 4, 2004, pp. 71–77.

Macrolocalization of Plastic Flow in Zinc Single Crystals Oriented for Basal Glide

V. I. Danilov, K. V. Gonchikov, and L. B. Zuev

Institute of Strength Physics and Materials Science, Siberian Division, Russian Academy of Sciences, Tomsk, 634055 Russia

e-mail: dvi@ms.tsc.ru

Received August 20, 2003

Abstract—The pattern of plastic flow macrolocalization in actively loaded zinc single crystals has been studied. The character of localization consistently varies in accordance with the stage of plastic flow. The results are compared to the analogous data for single crystals with an fcc lattice. The common features and individual peculiarities in evolution of the patterns of plastic flow localization in materials with different crystal structures are revealed. © *2004 MAIK "Nauka/Interperiodica".*

Quantitative investigations of the macrolocalization of plastic strain in single crystals of metals have been extensively performed since the mid-1990s [1–4]. The results of these studies allowed the spatial and kinetic characteristics of this process to be determined and showed that these characteristics are determined to a considerable extent by the type of the stress–strain curve of a given material. In was shown [1–4] that the pattern of macrolocalization of the plastic strain always possess an ordered character. On the yield plateau, where the straining proceeds by propagation of Lüders bands, a single localization front propagates at a constant velocity along the loaded sample. In the stage of easy glide, several fronts may appear and move either in the same or in opposite directions so that every element in the sample is passed only once. The stage of linear hardening features synchronous motion of a series of equidistant deformation fronts traveling over the sample several times in both directions. In the parabolic stage, a system of stationary spatially periodic localization zones appears upon chaotization of the strain field.

The above systematic pattern was established for single crystals of pure face-centered cubic (fcc) metals and doped fcc alloys and then confirmed for body-centered cubic (bcc) materials. Hexagonal close packed (hcp) single crystals were previously not studied in this respect. It is known that, despite an apparently similar sequence of stages on the stress–strain curves, the microscopic mechanisms of plastic flow in hcp materials are substantially different from those operative in fcc and bcc single crystals [5–7].

The experiments were performed with single crystal plates of zinc (99.997% Zn) with the working part dimensions 25 × 4 × 2.5 mm. The long crystal axis coincided with the $[\bar{1}2\bar{1}4]$ direction, and the wide sample face coincided with the $(0\bar{4}43)$ crystal plane. These crystallographic parameters ensure the basal glide in $(0001)[\bar{1}2\bar{1}0]$ and $(0001)[1\bar{2}10]$ systems with the Schmid factors ±0.48, respectively. These systems provide for the traces of gliding on the $[\bar{2}110]$ sample face, making an angle of 90° with the axis of tension.

The samples were tensile tested at a rate of $\dot{\varepsilon} = 6.7 \times 10^{-5}$ s^{-1} at room temperature. As expected [5], we obtained a stress–strain curve with clearly pronounced three stages (A, B, and C) of basal glide in hcp single crystals. The critical shear stress was $\tau_0 = 2.4$ MPa, the total linear strain at break was $\varepsilon_{tot} = 270\%$, and the lengths of stages were determined by $\gamma_A = 0.48$ (stage A), $\gamma_B = 0.6$ (stage B), and γ_C from 1.6 to fracture (stage C). Stage A was preceded and stages A and B were separated by extended transition regions: $\gamma_{e-A} = 0.28$ and $\gamma_{A-B} = 0.24$. The transition between stages B and C was smooth. Stages A and B were described by straight lines with the hardening coefficients $\theta_A = 3.26$ MPa and $\theta_B = 3.74$ MPa, respectively ($\theta = d\tau/d\gamma$). In stage C, the hardening coefficient exhibited a monotonic decrease indicative of the parabolic behavior.

In each stage, the sample was studied by two-exposure speckle interferometry for tracing evolution of the fields of displacement vectors of the points on the working surface and for determining the distributions of local elongations ε_{xx} [1, 3].

After the transition from elasticity to developed plastic flow (the onset of stage A), the sample features three strain localization zones in which the rate of strain accumulation is one order of magnitude greater than the $\Delta\varepsilon_{tot}$ increment (Fig. 1a and 1b). These zones are oriented perpendicularly to the axis of tension and represent the sites of preferential emergence of the basal dislocations. Previously, we observed this situation for the

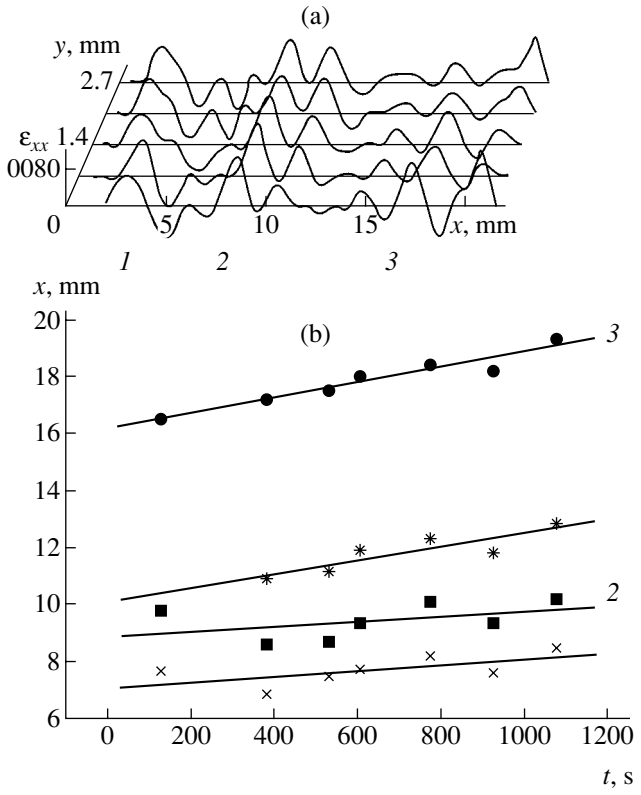

Fig. 1. Patterns of (a) the strain localization zones *1–3* and (b) the motion of deformation fronts in stage A for Zn single crystal loaded to $\gamma_{tot} = 0.3$.

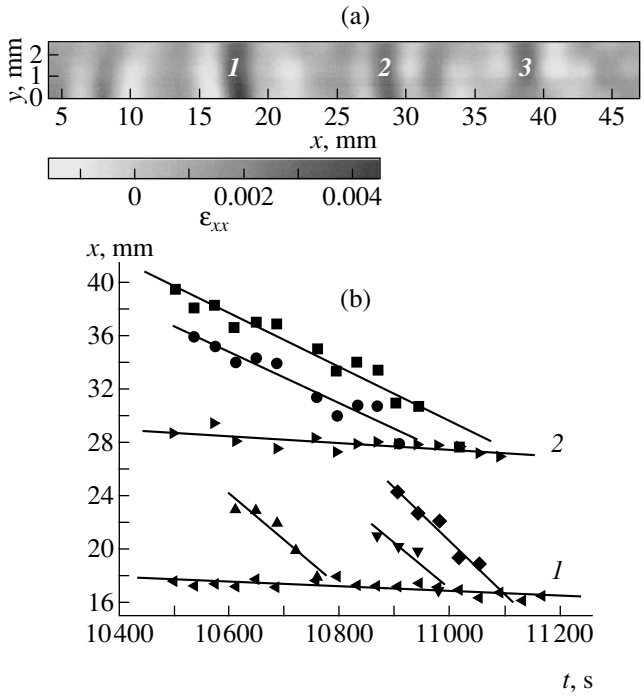

Fig. 2. Patterns of (a) the stationary strain localization zones *1–3* and mobile local strain foci and (b) the kinetics of local strain foci motion in the region of zones *2* and *3* in stage B for Zn single crystal loaded to $\gamma_{tot} = 1.168$.

easy glide stage in fcc single crystals, for example, in copper and nickel [2], where the localization zones were oriented in the direction of traces of the primary system glide.

As can be seen from the data in Fig. 1a, the zones under consideration are situated near the grips (*1* and *3*) and in the middle of the sample (*2*). Note the complicated structure of the middle localization zone *2*. This zone exhibits three interrelated peaks spaced slightly more than 2 mm from each other. In the course of straining, this central zone tends to expand due to a shift of the peak closest to the movable grip of the test machine. The localization zone situated at the movable grip also exhibited a shift. We failed to detect any shift of the strain localization zone situated at the fixed grip.

Figure 1b shows positions of the strain localization zones plotted as functions of the loading time. Using these data, the velocity of propagation of the localization zones were estimated as $v_3 = 2.6 \times 10^{-6}$ m/s and $v_2 = 2.3 \times 10^{-6}$ m/s for the zones at the movable grip (*3*) and in the middle of the sample (*2*), respectively. This motion cannot be simply explained as being due to elongation of the sample, since the velocity of the movable grip of the test machine was maintained constant ($v_m = 1.67 \times 10^{-6}$ m/s). The true velocity of propagation of the deformation fronts can be estimated as $v_{fr} = v_n - \varepsilon X_n$, where X_n is the position of the corresponding front at the beginning of stage A (where the sample can be considered as undeformed) and v_n is the velocity evaluated from Fig. 1b. Then, the velocities of propagation of both strain localization zones are the same: $v_{fr} = 1.5 \times 10^{-6}$ m/s. Taking into account that the duration of stage A was about 4500 s, we infer that both fronts travel a distance of about 7 mm. This implies that, by the end of stage A, the mobile edge of the middle zone *2* will reach the initial position of zone *3*, while the latter zone will reach the end of the working part of the sample.

The passage to the linear stage B changes the character of strain distribution. The pattern of sample straining in this stage comprises three distinct strain localization zones (Fig. 2a). These zones remain stationary during the entire stage B. However, there are intermediate small-amplitude local elongation maxima which move with time at an average velocity of 2.7×10^{-5} m/s toward the three main zones (Fig. 2b). By the end of stage B, this motion ceases, whereas the initially stationary zones lose their stability.

In the parabolic hardening stage C, the stationary strain localization zones *1*, *2*, and *3* (existing in stage B) lose their spatial periodicity and gradually shift toward the movable grip. The greater the distance from the zone to the grip, the higher the velocity of this motion. The maximum velocity of accumulation of the plastic strain was observed in zone *3*. It is the maximum local elongation in this zone that resulted in the sample fracture after a 2-h loading. Small-amplitude local strain

localization foci appearing randomly in various parts of the sample during the loading cycle were superimposed on the above main trends in evolution of the strain localization zones.

A comparative analysis of the whole body of our experimental results and the analogous data on the plastic flow localization in fcc single crystals leads to the following conclusions. Stage A in the hcp single crystals studied could be considered as analogous to stage I of easy glide in fcc materials. Stage B is analogous to the linear hardening stage II, and stage C, to the parabolic hardening stage III [5]. Should it be the case, we might expected the evolution of the patterns of strain macrolocalization in the corresponding stages to be similar, the more so as there is a strict correspondence between the strain localization type and the law of plastic flow irrespective of the crystal structure (see, e.g., [1]).

However, there is no complete agreement between the behavior observed in stage A and the laws established previously. Indeed, three strain localization zones had already been formed before the onset of stage A (and observed during this stage) in loaded Zn single crystal. The leading fronts of the localization zones, rather that the whole bands, were seen to move. However, these fronts in the sample studied (as well as in other materials) moved at the same constant velocity and passed along the sample only once during the stage under consideration. Large extension of stage A accounted for very small velocities of the fronts, but a comparable kinetics of the strain localization zones was previously observed in single crystals of a high-manganese austenite steel oriented for single twinning [4].

In stage B, peculiarities in the evolution of the patterns of strain localization in Zn single crystals are even more pronounced. This stage reveals stationary straining zones dividing the sample into three regions. However, all regions feature synchronous motion of small-amplitude local elongation maxima at the same constant velocity. This motion is restricted to within said sample regions formed by the stationary zones. The boundaries of these zones probably represent the stress release bands originally observed by Regel and Govorkov (see, e.g., [8]). The velocities of mobile strain localization foci are comparable with those reported in fcc single crystals [1–4].

Finally, the parabolic hardening stage C could be expected to display stationary spatially periodic strain localization zones [3]. In contrast, Zn single crystals loaded in this stage show the motion of (previously stationary) localization zones toward the future fracture site. However, as was previously demonstrated for the parabolic hardening stage in polycrystalline hcp alloy Zr–1% Nb [9], a stationary systems of deformation fronts is observed only for a parabola index of $n \geq 0.5$. For $n < 0.5$, the strain localization maxima initially move so as to remain equidistant. At smaller values of the parabola index ($n < 0.3$), the motion loses synchronism and the strain localization maxims merge in a single focus determining the future fracture site. Apparently, this behavior is not a peculiarity of hcp materials: a similar situation controlled by the parabola index was observed in the parabolic hardening stage in bcc samples.

REFERENCES

1. L. B. Zuev, V. I. Danilov, and B. S. Semukhin, Usp. Fiz. Met. **3**, 237 (2002).
2. V. I. Danilov, K. V. Gonchikov, L. B. Zuev, and S. A. Barannikova, Kristallografiya **47**, 730 (2002) [Crystallogr. Rep. **47**, 672 (2002)].
3. L. B. Zuev and V. I. Danilov, Philos. Mag. A **79**, 43 (1999).
4. V. I. Danilov, S. A. Barannikova, and L. B. Zuev, Zh. Tekh. Fiz. **73** (11), 69 (2003) [Tech. Phys. **48**, 1429 (2003)].
5. R. Berner and H. Kronmüller, *Plastische Verformung von Einkristallen* (Springer, Berlin, 1965; Mir, Moscow, 1969), translated from German.
6. R. W. K. Honeycombe, *The Plastic Deformation of Metals* (Cambridge Univ. Press, Cambridge, 1968; Mir, Moscow, 1972).
7. V. I. Startsev, V. Ya. Il'ichev, and V. V. Pustovalov, *Low-Temperature Plasticity and Strength of Metals and Alloys* (Metallurgiya, Moscow, 1975) [in Russian].
8. A. A. Urusovskaya, *Some Problems in the Physics of Plasticity of Crystals* (Izd. Akad. Nauk SSSR, Moscow, 1960) [in Russian], pp. 75–116.
9. T. M. Poletika, V. I. Danilov, L. B. Zuev, *et al.*, Zh. Tekh. Fiz. **72** (9), 57 (2002) [Tech. Phys. **47**, 1125 (2002)].

Translated by P. Pozdeev

Technical Physics Letters, Vol. 30, No. 2, 2004, pp. 164–167. Translated from Pis'ma v Zhurnal Tekhnicheskoĭ Fiziki, Vol. 30, No. 4, 2004, pp. 78–86.

The Effect of Electron Beam Fusion on the Structure and Properties of Plasma Jet Sprayed Nickel Alloy Coatings

A. D. Pogrebnyak[a], V. V. Vasilyuk[a], D. L. Alontseva[b], Yu. A. Kravchenko[b], Sh. M. Ruzimov[c], and Yu. N. Tyurin[d]

[a] *Institute of Surface Modification, Sumy, Ukraine*
[b] *East-Kazakhstan State University, Ust'-Kamenogorsk, Kazakhstan*
[c] *National University, Tashkent, Uzbekistan*
[d] *Paton Institute of Electric Welding, National Academy of Sciences of Ukraine, Kiev, Ukraine*

Received June 26, 2003

Abstract—Nickel-based alloy coatings were obtained on carbon steel (steel 3) samples by means of high-velocity pulsed plasma jet spraying of PG-10N-01 and PGAN-33 commercial powders, followed by electron beam fusion of the coating and substrate. The coated samples were studied by methods of X-ray diffraction, scanning electron microscopy, and electron-beam microprobe (energy-dispersive X-ray spectroscopy) and tested for hardness, friction wear, corrosion resistance, and adhesion. It was found that the electron beam processing leads to an almost tenfold increase in the friction wear resistance, a threefold growth in microhardness (relative to that of the substrate), and a significant increase in the resistance to corrosion in acid media. The observed increase in the working characteristics is related to changes in the phase composition, grain structure refinement, and redistribution of alloy components in the substrate and film and a decrease in porosity of the coating material. © *2004 MAIK "Nauka/Interperiodica".*

Development of the existing technologies and the creation of new machines operating at ultrahigh speeds under the conditions of high temperatures and pressures pose increasing requirements on construction materials. One of the modern approaches to obtaining advanced materials meeting such requirements is based on combined (duplex, triplex) methods of alloy processing [1–3]. Nickel-based alloys are still among very promising materials [4]. In recent years, the refractory coatings of ceramics and metal–ceramic composites are frequently deposited by means of high-velocity pulsed plasma jet spraying [5–9].

Plasma jet spraying technology, while providing for the formation of good coatings with high efficiency [7–10], still encounters some problems, such as an excess porosity (0.5–1.5%) of the deposit and the oxidation of both the upper surface and the coating–substrate interface. These problems can be solved, for example, by processing coated articles with high-current electron, ion, and plasma beams. These beams cause fusion of the coating material and enhance mass transfer processes that lead to healing of the pores and modification of the elemental composition.

The aim of this study was to obtain nickel-based coatings on a carbon steel by plasma jet spraying of commercial powdered alloys and to study the structure and properties of samples before and after electron-beam-induced total fusion of the coating and substrate. The powdered alloys were PG-10N-01 (B, 2.8–3.4; C, 0.6–1; Si, 4.0–4.5; Cr, 19–20; Fe, 4.0–4.5 wt %; Ni to balance) and iron-free PGAN-33 (Cr, ~24; Mo, ~4; Si, ~2; W, 1; B ~ 1.5 wt %; Ni to balance).

The samples of a carbon steel (steel 3) with dimensions $100 \times 20 \times 3.4$ mm were sand-blasted and coated by pulsed plasma jet spraying from both sides to a total thickness of 45–50 μm in a single run on an Impuls-5 setup operating at a pulse duration of 3 ms and a pulse repetition rate of 4 Hz. The eroded (evaporated) electrode was made of a Mo alloy or Ta (regimes 1 and 2, respectively). The power density per pulse reached $(5.8–6) \times 10^6$ W/cm^2. Then, the coated samples were electron beam processed on a U-212 setup (Paton Institute of Electric Welding, Kiev) operating at an accelerating voltage of 30 kV, electron beam current density of up to 30 mA/cm^2, and a beam oscillation amplitude of 15 or 30 mm. The treatment was performed in a total fusion regime, whereby an energy density is selected so as to provide total fusion of the coating and partial fusion of the substrate. The samples after plasma jet spray coating and electron beam fusion were cut into parts and studied by various analytical and testing methods.

The samples were studied in a REMMA 102 (SELMI, Sumy, Ukraine) scanning electron microscope (SEM) with a Si(Li) detector. The qualitative and quantitative surface analyses were performed using a WDS-2 wavelength dispersive X-ray (WDX) spectrometer. The phase composition of coatings was studied by X-ray diffraction in a DRON-2 diffractometer using CoK_α radiation. The hardness was tested using a

PMT-3 device with a diamond Vickers pyramid indenter at a 20, 50, or 100 g load. The microhardness measurements were performed in the coating, transition layer, and substrate material in an oblique lapped section of a sample. The wear was studied in a rod-on-disk configuration using a friction test machine with a 5-mm rod of ShH-15 steel. The corrosion tests were performed in a 0.5 M aqueous sulfuric acid solution at temperatures in the 200–400°C interval [8].

Figure 1 shows a fragment of the X-ray diffraction pattern of a sample after the double (coating plus fusion) treatment. An analysis of this diffractogram showed evidence of a multiphase composition of the coating, including FeCr (weight fraction, about 15%), surface intermetallic compounds Fe_7Mo_6 and FeMo (12 and 4% of the total composition, respectively), and Ni as the base element (65%). However, the lattice of the base component was strongly extended so that the lattice parameter was 3.55 Å. The coating contained oxide phases of Ni_2O_3 (9%) and, probably, NiO (about 4%). The surface composition of the samples upon electron beam fusion included Cr (65%), α-Fe (about 6%), and Fe_2O_3 (about 9%). Note that molybdenum (absent in the initial powdered alloy composition) appeared as a result of erosion of the consumable electrode made of a Mo-containing alloy.

Figure 2 shows an SEM micrograph of the coating surface in the region of a "triple" point of a sample after the double processing. As can be seen, the surface roughness is decreased over the entire electron-irradiated area; nevertheless, there are regions of considerable roughness related to the fusion. Some regions contain incompletely dissolved particles of the initial powder (probably, refractory elements and their carbides). An analysis of the oblique section of a coating after the double processing showed that the average grain size decreased from hundreds to a few microns (hundreds of nanometers) in a subsurface layer of at least 9–15 μm thickness (depending on the electron beam energy density).

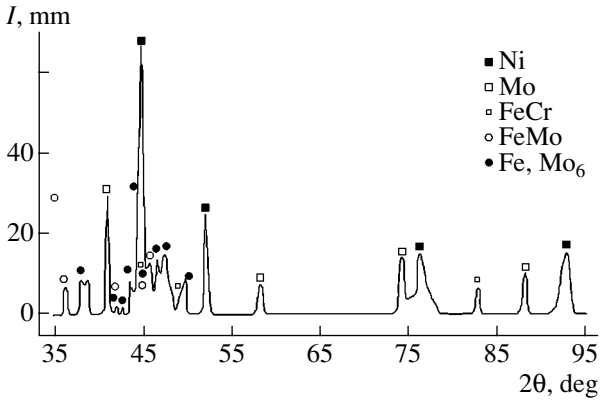

Fig. 1. A fragment of the X-ray diffraction pattern of a Ni-based alloy coating obtained upon plasma jet spraying and electron beam fusion.

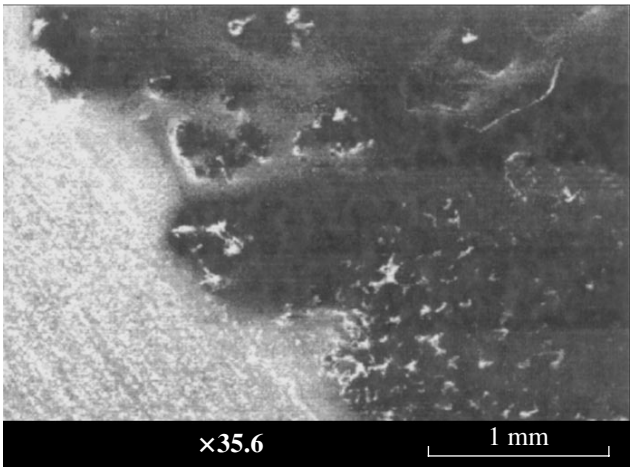

Fig. 2. SEM image in the region of a "triple" point in the oblique lapped section of a Ni-based alloy coating obtained upon plasma jet spraying and electron beam fusion.

Figure 3a presents a general view of the surface morphology of a PG-10N-01 coating upon electron beam processing (total fusion of the coating and partial

Table 1. Surface elemental composition determined at various sites of a nickel alloy coating on steel after pulsed plasma jet spraying (regime 1, Mo alloy electrode) and electron beam fusion

Site of analysis	Al	Si	K	Ca	Cr	Fe	Ti	Ni	Mo
Obr4_1	0.000	4.510	0.000	0.000	13.551	3.924	0.000	77.807	0.207
Obr4_2	0.000	7.337	0.000	0.000	13.611	3.792	0.000	75.259	0.000
Obr4_3	0.000	14.073	0.903	2.918	8.043	45.557	0.000	22.929	5.577
Obr4_4	0.000	2.827	0.016	0.085	17.968	2.818	0.000	76.286	0.000
Obr4_5	24.076	5.576	0	0.292	6.852	32.925	1.257	21.644	7.377
Obr4_6	0.000	3.273	0.039	0.059	16.117	3.788	0.000	76.700	0.023
Obr4_7	0.458	6.153	0.089	0.102	16.538	4.998	0.000	70.905	0.758
Obr4_8	0.000	0.677	0.000	0.080	0.692	21.206	0.000	9.015	68.331
Obr4_9	0.429	4.551	0.142	0.175	14.151	10.319	0.000	60.884	9.349

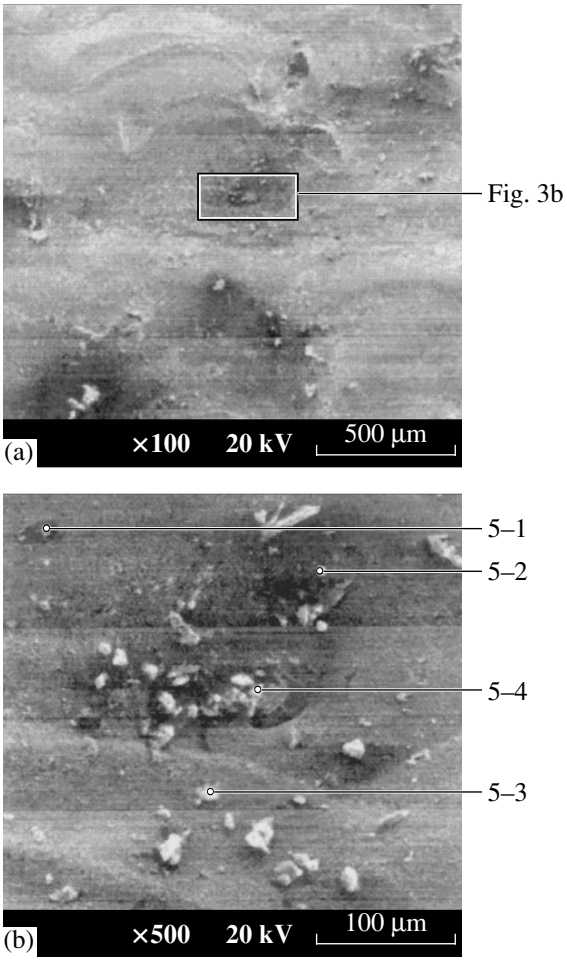

Fig. 3. SEM images of a Ni-based alloy coating obtained by plasma jet spraying of a PG-10N-01 powder and electron beam processing (total fusion of the coating and partial fusion of the steel substrate): (a) general view; (b) image of the surface relief in the region of a shallow depression indicated in (a). Points indicate the sites of elemental analyses summarized in Table 2 (one site from (a) and four sites from (b)).

fusion of the substrate). The electron beam treatment leads to the formation of a wavy surface relief. Some regions of the surface exhibit shallow depressions (Figs. 3a and 3b), which act as the centers of accumulation of small inclusions. The surface of the coating also contains nonuniformly distributed dark regions in which the main component is iron.

Figure 4 shows the WDX spectra of elemental composition measured for two inclusions of different shape and appearance at the sites indicated on the SEM images. As can be seen from these data, the coating is characterized by a high content of Ni (up to 40%), Fe, Cr, and Si and contains a small amount of Al and Ta (for the samples processed in regime 2). Tables 1 and 2 present data on the concentrations of these elements measured in nine and five probing sites of two samples. It should be noted that the results of analyses are absolutely different from the initial compositions of powdered alloys, while Ta appears as a result of erosion (evaporation) of the internal electrode used in regime 2.

The results of microhardness measurements on the surface of samples before and after coating and subsequent electron beam processing are 150 kgf/mm^2 for the initial substrate, 750–800 kgf/mm^2 for the plasma jet sprayed coating, and 500 kgf/mm^2 for the samples after double processing (plasma spray coating and electron beam fusion). The decrease in the microhardness after the last treatment is explained by the surface segregation of iron (in some sites, up to 94%) due to the electron-beam-induce mixing of the melt. Simultaneously, some elements penetrate from the coating into the substrate (down to a depth of 35–40 μm), which provides for improved adhesion of the coating to the substrate. The increase in the resistance to wear could be related to the formation of oxides (Fe_2O_3, Ni_2O_3, NiO, etc.) and considerable changes in the coating structure as a result of the double processing.

In conclusion, we have demonstrated that the electron beam processing of Ni-based coatings obtained by plasma jet spraying of PG-10N-01 and PGAN-33 powdered alloys leads to mixing of the coating and substrate, the formation of new phases (FeCr, Fe_7Mo_6, FeMo, Ni, and Ni_2O_3), grain refinement, and pore healing. This results in a significant increase in the working characteristics of the coated material, such as hardness,

Table 2. Surface elemental composition determined at various sites of a nickel alloy coating on steel after pulsed plasma jet spraying (regime 2, Ta electrode) and electron beam fusion

Site of analysis	Al	Si	S	Ca	Cr	Mn	Fe	Ni	Ta
Pogr5_1	0.980	0.000	0.132	0.202	0.822	15.042	94.601	0.822	1.677
Pogr5_2	0.325	0.000	0.139	0.020	17.779	0.000	38.655	37.122	5.961
Pogr5_3	4.097	19.371	0.331	1.820	7.932	0.000	47.504	18.943	0.000
Pogr5_4	8.266	0.000	0.000	3.876	15.763	0.000	28.459	36.134	7.502
Pogr5_5	1.980	0.000	0.211	0.365	15.042	0.000	28.459	40.415	9.107

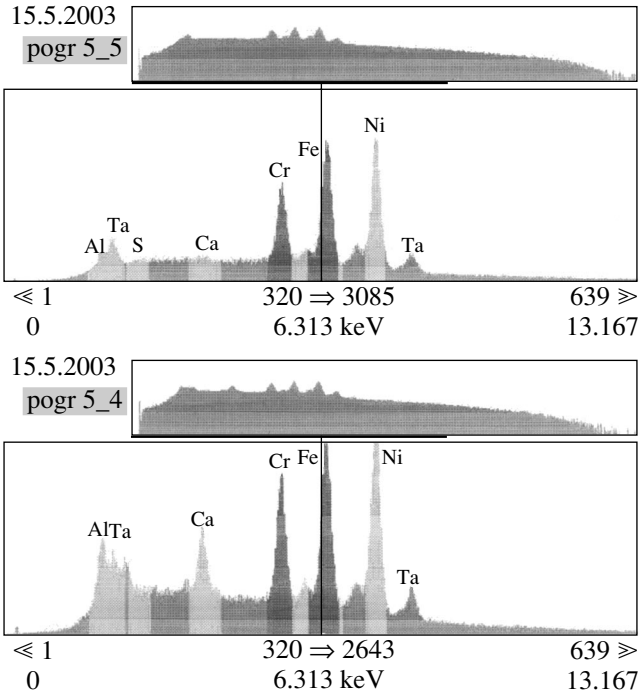

Fig. 4. WDX spectra of the elemental composition at two sites of a Ni-based alloy coating obtained by plasma jet spraying and electron beam processing (see the sites indicated in Figs 3a and 3b). The top panels show the wide-range spectra; the bottom panels show the results of high-resolution elemental analysis.

resistance to wear and corrosion, and the coating adhesion to substrate.

Acknowledgments. The authors are grateful to A.A. Bondarev, O.P. Kul'ment'eva, O.V. Kolisnichenko, and V.S. Kshnyakin for their help in conducting experiments.

This study was supported in part by the Ministry of Education and Science of Ukraine (project no. 2M/0145-2001) and by the National Research Institute for Materials (Tsukuba, Ibaraki, Japan).

REFERENCES

1. A. D. Pogrebnjak and N. I. Shumakova, Surf. Coat. Technol. **122**, 163 (1999).
2. A. D. Pogrebnjak, S. N. Bratushka, V. I. Boyko, *et al.*, Nucl. Instrum. Methods **145**, 373 (1998).
3. A. D. Pogrebnjak, A. P. Kobzev, B. P. Critsentko, *et al.*, J. Appl. Phys. **87**, 2142 (2000).
4. A. D. Pogrebnyak, O. P. Kul'ment'eva, V. S. Kshnyakin, *et al.*, Poverkhnost **6**, 36 (2003).
5. S. Kuroda, in *Proceedings of the 15th International Thermal Spray Conference, Nice, 1998*, p. 539.
6. A. I. Zverev, S. Yu. Sharivker, and E. A. Astakhov, *Detonation Deposition of Coatings* (Sudostroenie, Leningrad, 1979) [in Russian].
7. A. D. Pogrebnyak, Yu. N. Tyurin, and Yu. F. Ivanov, Pis'ma Zh. Tekh. Fiz. **26** (21), 53 (2000) [Tech. Phys. Lett. **26**, 960 (2000)].
8. A. D. Pogrebnyak, M. V. Il'yashenko, V. S. Kshnyakin, *et al.*, Zh. Tekh. Fiz. **71** (7), 111 (2001) [Tech. Phys. **46**, 897 (2001)].
9. Yu. N. Tyurin and A. D. Pogrebniak, Surf. Coat. Technol. **111**, 269 (1999).
10. P. Misaelides, A. D. Pogrebnjak, A. Hatzidimitrioun, *et al.*, in *Proceedings of European Materials Research Society, Strasbourg, 2003* (in press).

Translated by P. Pozdeev

Technical Physics Letters, Vol. 30, No. 2, 2004, pp. 168–171. Translated from Pis'ma v Zhurnal Tekhnicheskoĭ Fiziki, Vol. 30, No. 4, 2004, pp. 87–94.

The Frequency Spectrum of a Voltage Measured in an Amorphous Wire Magnetized in Alternating Magnetic Field

N. A. Buznikov[a], A. S. Antonov[a], A. A. Rakhmanov[a], A. B. Granovsky[b], M. A. Kartashov[b], and N. S. Perov[b]

[a] *Institute of Theoretical and Applied Electrodynamics, Russian Academy of Sciences, Moscow, Russia*

[b] *Moscow State University, Moscow, 119899 Russia*

Received August 4, 2003

Abstract—We have studied the process of magnetization reversal in amorphous microwires under the action of a longitudinal (axial) high-frequency magnetic field. The amplitudes of harmonics in the frequency spectrum of the response voltage between the wire ends were measured as functions of the high-frequency field amplitude and a dc axial magnetic field strength. For relatively large amplitudes of the high-frequency field, the first several harmonics in the frequency spectrum of the response voltage are highly sensitive with respect to the dc magnetic field. The experimental results are interpreted within the framework of a simple electrodynamic model. © *2004 MAIK "Nauka/Interperiodica".*

Investigation into the high-frequency properties of magnetically soft amorphous materials is among the most important directions of research in the physics of magnetic phenomena. These investigations are mostly devoted to the phenomenon of giant magnetoimpedance, whereby the impedance of a magnetically soft conductor strongly changes in a weak applied magnetic field (see, e.g., reviews [1, 2]). The giant magnetoimpedance effect is observed for small ac current amplitudes, that is, when the sample magnetization is a linear function of the exciting field.

In recent years, considerable interest of researchers has been also devoted to nonlinear phenomena in magnetically soft conductors [3–12], which involve the magnetization reversal under the action of magnetic fields generated by ac currents of high amplitude. Use of the nonlinear voltage response may offer more promising applications [4, 7, 9, 12] than the giant magnetoimpedance effect.

This paper reports on the results of investigation of the frequency spectrum of an ac voltage between the ends of an amorphous microwire exhibiting magnetization reversal under the action of an ac longitudinal (axial) magnetic field.

The experiments were performed with amorphous microwires of the composition $Co_{68}Fe_{4.5}Si_{15}B_{12.5}$ available from Unitika Ltd. (Japan). The samples were prepared using wires with a diameter of 30 μm and a length of 6.6 mm. A sample was exposed to a high-frequency magnetic field generated by a coil oriented along the wire axis. The ac field amplitude H_0 could be varied from 0.2 to 25 Oe, and the frequency f, from 0.5 to 2 MHz. The measurements were performed in the presence of a homogeneous dc axial magnetic field H_{DC} with a strength varying within ±4 Oe. The amplitudes of harmonics of the ac response voltage between the ends of the sample were measured using an HP4395A spectrum analyzer.

For small ac excitation field amplitude H_0, the main component in the frequency spectrum of the response voltage is the first harmonic, while the contribution of all other harmonics is negligibly small. In this case, the voltage between the sample ends is related to a nondiagonal component of the impedance tensor [13–15]. As the ac field amplitude H_0 grows, the contribution of higher harmonics to the sample response increases. Figure 1 shows plots of the amplitudes V_k of the kth harmonics of the response voltage versus the dc axial magnetic field strength H_{DC} measured for two values of the ac field amplitude. The $V_k(H_{DC})$ curves exhibit no hysteresis and are symmetric relative to $H = 0$ (the harmonic amplitudes are independent of the direction of the dc magnetic field). As can be seen, the field dependences of the amplitudes of even and odd harmonics exhibit substantially different shapes (Fig. 1): in a zero dc field, the even harmonics are negligibly small, while odd harmonics possess maximum amplitudes. All harmonics exhibit additional maxima in a nonzero dc axial field. The values of H_{DC} corresponding to these maxima increase as linear functions of the high-frequency axial magnetic field amplitude H_0.

The experimental data will be considered within the framework of a simple electrodynamic model that provides adequate description of the main features of the

observed frequency spectrum of the ac response voltage. For the sake of simplicity, we assume that the microwires possess no domain structure and restrict the consideration to frequencies at which the skin effect can be ignored. Then, the ac axial magnetic field is homogeneously distributed in the wire cross section. This field induces variations in the sample magnetization with time, thus giving rise to the response voltage V between the sample ends that can be expressed as

$$V = \frac{2\pi Dl}{c}\frac{dM_C}{dt}, \tag{1}$$

where D is the wire diameter, l is the sample length, c is the velocity of light in vacuum, and M_C is the circular magnetization component.

Let us assume that the wire possesses a helicoidal anisotropy, with the anisotropy axis making a constant angle ψ with the circular direction and the anisotropy field H_a being constant over the entire sample [15]. The variation of magnetization of the wire under the action of the ac axial magnetic field can be determined proceeding from the condition of minimum of the free energy of the sample [4, 6, 9, 11, 16]. Under the above assumptions, the free energy density U is a sum of the energy densities due to the magnetic anisotropy and the Zeeman interaction:

$$\begin{aligned} U &= (MH_a/2)\sin^2(\theta - \psi) \\ &- M\{H_0\sin(2\pi ft) + H_{\mathrm{DC}}\}\sin\theta, \end{aligned} \tag{2}$$

where M is the saturation magnetization and θ is the angle of deviation of the magnetization vector from the circular direction. Minimization of the free energy functional (2) leads to the following equations for the longitudinal ($M_L = M\sin\theta$) and circular ($M_C = M\cos\theta$) magnetization components:

$$\begin{aligned} &H_a^2\cos^2(2\psi)M_C^2(M^2 - M_C^2) \\ &= M^2[\{H_{\mathrm{DC}} + H_0\sin(2\pi ft)\}MM_C \\ &+ H_a\sin(2\psi)(M_C^2 - M^2/2)]^2, \\ &M_L^2 = M^2 - M_C^2. \end{aligned} \tag{3}$$

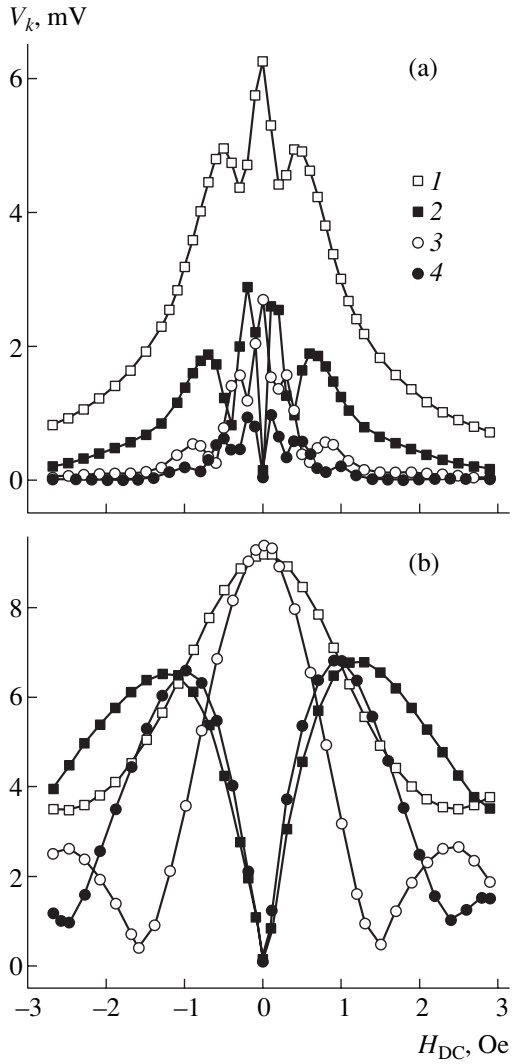

Fig. 1. Experimental amplitudes of the response voltage harmonics V_k versus dc axial magnetic field strength H_{DC} measured at a frequency of $f = 500$ kHz and an ac axial magnetic field amplitude of $H_0 = 4.6$ Oe (a) and 23.2 Oe (b): $k = 1$ (*1*), 2 (*2*), 3 (*3*), and 4 (*4*).

Using relations (1) and (3), we obtain an expression for the response voltage,

$$V/V_0 = -\frac{M_L^2 H_0\cos(2\pi ft)}{H_a\cos(2\psi)(M_L^2 - M_C^2) - 2H_a\sin(2\psi)M_L M_C - \{H_{\mathrm{DC}} + H_0\sin(2\pi ft)\}MM_L}, \tag{4}$$

where $V_0 = 4\pi^2 DlfM/c$ and the magnetization components M_L and M_C satisfy Eqs. (3). The frequency spectrum of the response voltage between the wire ends can be determined by calculating the Fourier transform of Eq. (4). The results of calculations show that, for small amplitudes H_0 of the ac axial field, the magnetization vector performs small oscillations about the equilibrium position, so that the first harmonic is dominating in the frequency spectrum [15]. When H_0 exceeds a certain threshold value, the magnetization components

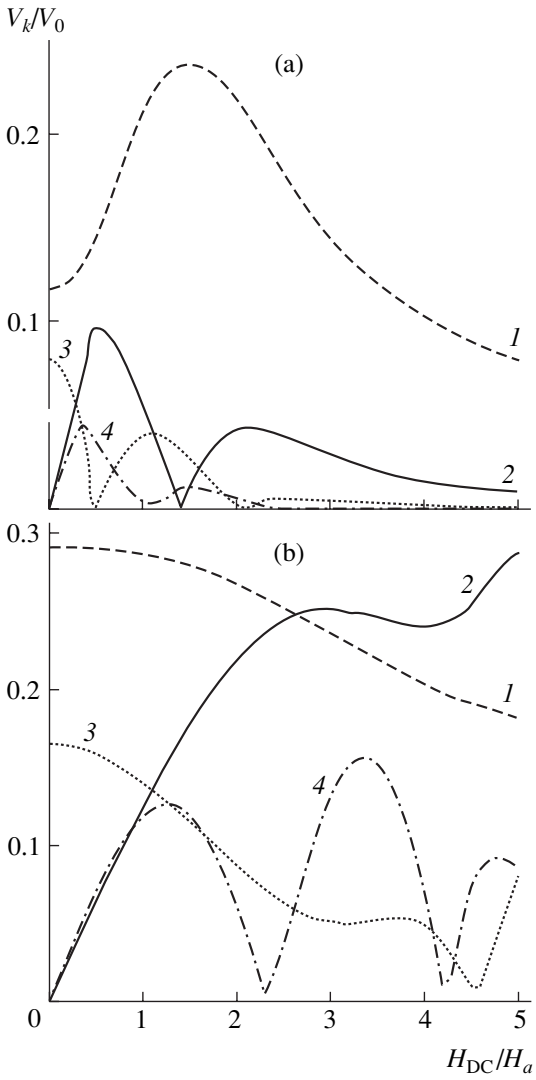

Fig. 2. The amplitudes V_k of the response voltage harmonics as functions of the dc axial magnetic field strength H_{DC} calculated for $\psi = 0.1\pi$ and $H_0/H_a = 1$ (a) and 5 (b): $k = 1$ (*1*), 2 (*2*), 3 (*3*), and 4 (*4*).

exhibit a jumplike change in each half-cycle of the high-frequency field. This is accompanied by the growth of higher harmonics in the frequency spectrum of the response signal [4, 9].

Figure 2 shows the amplitudes V_k of the response voltage harmonics as functions of the dc magnetic field strength H_{DC}, calculated using Eqs. (3) and (4). The data are presented only for the positive values of H_{DC}, because the harmonic amplitude in the model under consideration are symmetric with respect to the change of the dc field direction. The calculated curves of $V_k(H_{DC})$ behave in qualitative agreement with the experimental data. However, estimates obtained using a typical value of the saturation magnetization of a cobalt-based wire, $M = 600$ G, show that the calculated values of V_k are about ten times the measured ones. This discrepancy can be primarily related to the skin effect ignored in the model adopted. In addition, correct quantitative description of the experimental data requires making allowance of the domain structure of the sample and taking into account the inhomogeneous distribution of the anisotropy field across and along the wire [17].

Thus, we have studied the process of magnetization reversal in a cobalt-based amorphous microwire under the action of a high-frequency axial magnetic field. The sample magnetization reversal gives rise to higher harmonics in the frequency spectrum of the response voltage measured between the sample ends. In contrast to the case of a sample exposed to the field of a high-frequency current studied in [4, 7, 9, 11], both even and odd harmonics of the response voltage of our sample magnetized in a high-frequency axial field are highly sensitive with respect to the dc axial magnetic field strength. In particular, for an ac field amplitude of $H_0 = 23.2$ Oe, the sensitivity of the response voltage to the dc field strength amounts to about 5 mV/Oe. This estimate coincides in the order of magnitude with the maximum sensitivity reported for the giant magnetoimpedance effect. The high sensitivity of the harmonic amplitudes to the dc axial field strength and the absence of hysteresis in this dependence allow the nonlinear magnetization behavior to be used for the development of sensors for monitoring weak magnetic field.

Acknowledgments. This study was supported by the Russian Foundation for Basic Research (project no. 02-02-16707) and the Presidential Program for Support of the Leading Scientific Schools (project NSh-1694.2003.2). One of the authors (N.A.B.) gratefully acknowledges the support from the Foundation for Promotion of Science in Russia.

REFERENCES

1. M. Vazquez, J. Magn. Magn. Mater. **226**–**230**, 693 (2001).
2. M. Knobel and K. R. Pirota, J. Magn. Magn. Mater. **242**–**245**, Part 1, 33 (2002).
3. R. S. Beach, N. Smith, C. L. Platt, *et al.*, Appl. Phys. Lett. **68**, 2753 (1996).
4. A. S. Antonov, N. A. Buznikov, I. T. Iakubov, *et al.*, J. Phys. D: Appl. Phys. **34**, 752 (2001).
5. C. Gomez-Polo, M. Vazquez, and M. Knobel, Appl. Phys. Lett. **78**, 246 (2001).
6. C. Gomez-Polo, M. Knobel, K. R. Pirota, and M. Vazquez, Physica B **299**, 322 (2001).
7. G. V. Kurlyandskaya, H. Yakabchuk, E. Kisker, *et al.*, J. Appl. Phys. **90**, 6280 (2001).

8. G. V. Kurlyandskaya, E. Kisker, H. Yakabchuk, and N. G. Bebenin, J. Magn. Magn. Mater. **240**, 206 (2002).
9. A. S. Antonov, N. A. Buznikov, A. B. Granovsky, *et al.*, J. Magn. Magn. Mater. **249**, 315 (2002).
10. J. G. S. Duque, A. E. P. de Araujo, M. Knobel, *et al.*, Appl. Phys. Lett. **83**, 99 (2003).
11. A. S. Antonov, N. A. Buznikov, A. B. Granovsky, *et al.*, Sensors & Actuators A **106**, 213 (2003).
12. G. V. Kurlyandskaya, A. Garcia-Arribas, and J. M. Barandiaran, Sensors & Actuators A **106**, 239 (2003).
13. N. A. Usov, A. S. Antonov, and A. N. Lagarkov, J. Magn. Magn. Mater. **185**, 159 (1998).
14. A. S. Antonov, I. T. Iakubov, and A. N. Lagarkov, J. Magn. Magn. Mater. **187**, 252 (1998).
15. D. P. Makhnovskiy, L. V. Panina, and D. J. Mapps, Phys. Rev. B **63**, 144424 (2001).
16. A. S. Antonov, N. A. Buznikov, and A. L. Rakhmanov, Pis'ma Zh. Tekh. Fiz. **26** (16), 1 (2000) [Tech. Phys. Lett. **26**, 698 (2000)].
17. M. Vazquez and A. Hernando, J. Phys. D: Appl. Phys. **29**, 939 (1996).

Translated by P. Pozdeev

Technical Physics Letters, Vol. 30, No. 2, 2004, pp. 85–87. Translated from Pis'ma v Zhurnal Tekhnicheskoĭ Fiziki, Vol. 30, No. 3, 2004, pp. 1–6.

The Effect of Annealing on the Electroluminescence of SiO_2 Layers with Excess Silicon

A. P. Baraban, D. V. Egorov, Yu. V. Petrov, and L. V. Miloglyadova

Institute of Physics, St. Petersburg State University, St. Petersburg, Russia

Received July 25, 2003

Abstract—We have studied the effect of annealing on the electroluminescence (EL) spectrum of Si–SiO_2 structures containing excess ion-implanted silicon in the oxide layer. The implantation of 150-keV silicon ions to doses in the range from 5×10^{16} to 3×10^{17} cm^{-2} leads to the appearance of an intense emission band at 2.7 eV in the EL spectrum. The postimplantation annealing leads to a decrease in the intensity of this band and to the appearance of a new EL band at 1.6 eV assigned to radiative transitions in defect centers formed at the boundaries between silicon nanoclusters and silicon dioxide. © *2004 MAIK "Nauka/Interperiodica".*

One of the main problems in modern optoelectronics is related to obtaining silicon-based structures exhibiting stable luminescence. Promising systems are porous silicon [1–3] and Si–SiO_2 structures with silicon nanoclusters introduced into the volume of the oxide layer [4–6]. The latter structures can be obtained by ion implantation of silicon into a silicon oxide layer followed by annealing [5, 6].

Below, we report on the results of investigation of the electroluminescence (EL) of annealed Si–SiO_2 structures with the oxide layer containing excess silicon introduced by ion implantation.

The SiO_2 layers with a thickness of 800 nm on *p*-Si substrates were obtained by thermal oxidation in humid oxygen atmosphere at 1100°C. Then, the oxide layer was implanted with 150-keV silicon ions to a dose in the range from 5×10^{16} to 3×10^{17} cm^{-2}. This range corresponds to an additional silicon content from 5 to 30% in the region of implant localization, with a maximum of the excess silicon content occurring at a depth of ~200 nm from the oxide layer surface. The postimplantation annealing of samples was performed for 16 h at 1000°C in dry nitrogen (N_2).

The EL spectra were measured in the electrolyte–dielectric–semiconductor system using a method described in detail elsewhere [7]. An advantage of studying the EL in this system is the ability to provide for the electron injection and acceleration in SiO_2 layers in a broad range of the electric field strength (the field is a necessary condition for the EL excitation). The EL spectra were measured at 273 K under the conditions excluding impact ionization in the silicon oxide volume [8].

The ion implantation of silicon into the oxide resulted in the appearance of an intense EL band with the maximum at ~2.7 eV. Subsequent annealing of the implanted structures led to a decrease in the intensity of this band and to the appearance of a new long-wavelength EL band in the region of 1.6 eV (Fig. 1). Figure 2 shows the EL spectra of the ion-implanted Si–SiO_2 structures with various concentrations of excess silicon in the oxide layer. The observed EL bands are well described by the Gaussian profiles (i) centered at 2.7 ± 0.06 eV with a full width at half maximum (FWHM) of 0.32 ± 0.06 eV and (ii) centered at 1.64 ± 0.08 eV with an FWHM of 0.16 ± 0.08 eV. It should be noted that the EL band at 1.6 eV exhibits a small (~0.05 eV) shift toward longer wavelengths when the excess silicon content in the oxide layer increases from 5–10 to 20–30%.

As can be seen from Fig. 2, the EL spectra of the samples containing 5–10% excess silicon display the

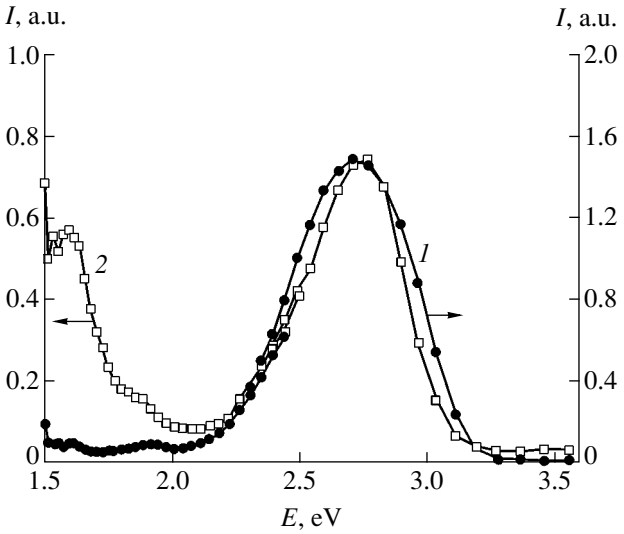

Fig. 1. The EL spectra of a Si–SiO_2 structure with 30% excess silicon implanted into the oxide layer, measured (*1*) before and (*2*) after annealing.

1063-7850/04/3002-0085$26.00 © 2004 MAIK "Nauka/Interperiodica"

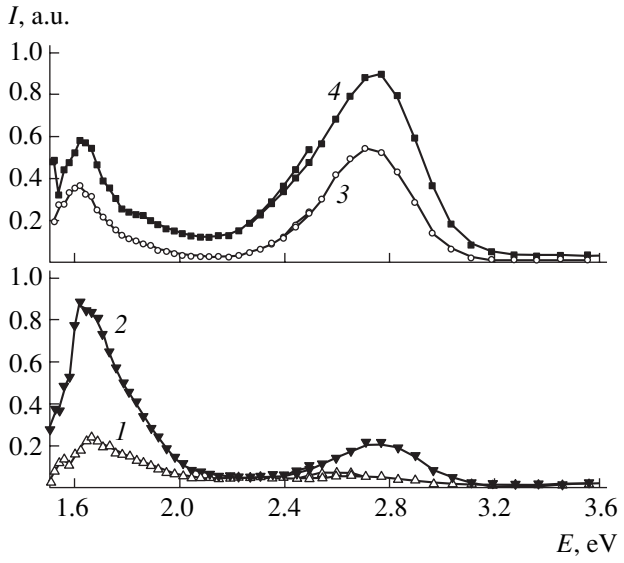

Fig. 2. The EL spectra of annealed Si–SiO_2 structures with the oxide layers containing various amounts of implanted excess silicon: (*1*) 5; (*2*) 10; (*3*) 20; (*4*) 30%.

most intense emission band at 1.6 eV, while the spectra of the structures with 20–30% excess silicon exhibit the maximum emission at 2.7 eV. The EL bands at 1.6 and 2.7 eV in the structures implanted with different doses were observed for various applied voltages (i.e., various average electric field strengths in the oxide). The threshold field strength decreased from 7.6 MV/cm to 5.6 MV/cm as the amount of excess silicon increased from 5 to 20% but then somewhat increased (to 6 MV/cm) for the samples with an excess silicon content of 30%. The intensities of both the 1.6 and 2.7 eV bands increased exponentially with the electric field strength in the oxide and exhibited a superlinear dependence on the current density in the structure.

As is known, ion implantation into a silicon oxide layer is accompanied by the intense formation of defects, including those responsible for the EL at 2.7 eV [9]. We believe that the latter defects are the so-called silylene centers representing oxygen atoms doubly coordinated to silicon [10]. Subsequent high-temperature annealing leads to a decrease in the concentration of defects, including silylene centers, which is manifested by a decrease in intensity of the EL band at 2.7 eV. It should be noted that annealing of the Si–SiO_2 structures implanted with argon ions also resulted in a decrease in intensity of the EL band at 2.7 eV appearing upon irradiation [11]. This effect of annealing was attributed to the decrease in the concentration of silylene centers in the course of restoration of silicon–oxygen bonds broken by ion bombardment.

In the case under consideration, the decrease in the concentration of silylene centers under the conditions of oxygen deficiency can be related to the formation of silicon nanoclusters during annealing. This possibility was suggested in [6], where annealing of the structures with various amounts of excess silicon led to the formation of nanoclusters of different sizes: 3, 3.8, and 5.3 nm for the samples containing 10, 20, and 30% excess silicon.

The energy position of the EL band at 1.6 eV exhibits virtually no variation (to within the experimental uncertainty) in all Si–SiO_2 structures studied. This fact does not allow this band to be attributed to radiative transitions in silicon nanoclusters, as was done in [4, 5], where the spectral positions of the long-wavelength EL and photoluminescence bands changed depending on the excess silicon content and, hence, on the size of silicon nanoclusters.

In our opinion, the EL band at 1.6 eV is related to defects at the boundary between Si nanoclusters and SiO_2, appearing during the formation of nanoclusters in the course of postimplantation annealing. These emission centers can be defects of the triply coordinated silicon type ($Si_3{=}Si^{\bullet}$), the particular properties of which are determined by the local environment (i.e., by the structure of nanoclusters) [12]. The density of such defects depends in a rather complicated manner on the content of excess silicon in the oxide, being influenced both by the size and geometry (surface area) of the clusters and by the number of silicon atoms per cluster. These EL centers are excited due to interaction with hot electrons formed when the oxide is exposed to a strong electric field, which is suggested by the dependence of the intensity of the EL band at 1.6 eV on the electric field strength in the oxide and on the electric current density in the Si–SiO_2 structure.

In conclusion, the postimplantation annealing of Si–SiO_2 structures containing excess silicon implanted into the oxide layer leads to the appearance of a new emission band at 1.6 eV in the EL spectrum. The spectral position of this band is, to the first approximation, independent of the concentration of excess silicon. The new EL band is attributed to the annealing-induced formation of $Si_3{=}Si^{\bullet}$ type defects at the boundaries between implanted silicon nanoparticles and silicon dioxide.

Acknowledgments. This study was supported by the Ministry of Defense of the Russian Federation, project no. PD02-1.2-356.

REFERENCES

1. L. T. Canham, Appl. Phys. Lett. **57**, 1046 (1990).
2. A. Richter, P. Steiner, F. Kozlowski, and W. Lang, IEEE Electron Device Lett. **12**, 691 (1991).
3. L. T. Canham, W. Y. Leong, M. I. J. Beale, *et al.*, Appl. Phys. Lett. **61**, 2563 (1992).

4. G. Franzo, A. Irrera, E. C. Moreira, *et al.*, Appl. Phys. A **74**, 1 (2002).
5. H. Z. Song, X. M. Bao, N. S. Li, and J. Y. Zhang, J. Appl. Phys. **82**, 4028 (1997).
6. B. Garrido, M. Lopez, O. Gonzales, *et al.*, Appl. Phys. Lett. **77** (20), 3143 (2000).
7. A. P. Baraban, V. V. Bulavinov, and P. P. Konorov, *Electronics of SiO_2 Layers on Silicon* (Leningr. Gos. Univ., Leningrad, 1988).
8. A. P. Baraban, I. V. Klimov, N. I. Tenoshvili, *et al.*, Pis'ma Zh. Tekh. Fiz. **15** (17), 44 (1989) [Sov. Tech. Phys. Lett. **15**, 680 (1989)].
9. A. P. Baraban and L. V. Miloglyadova, Zh. Tekh. Fiz. **72** (5), 56 (2002) [Tech. Phys. **47**, 569 (2002)].
10. L. N. Skuya, A. N. Streletskiĭ, and A. B. Pakovich, Fiz. Khim. Stekla **14**, 481 (1988).
11. A. P. Baraban, P. P. Konorov, L. V. Malyavka, and A. G. Troshikhin, Zh. Tekh. Fiz. **70** (8), 87 (2000) [Tech. Phys. **45**, 1042 (2000)].
12. C. T. White and K. L. Ngai, J. Vac. Sci. Technol. **16**, 1412 (1979).

Translated by P. Pozdeev

Technical Physics Letters, Vol. 30, No. 2, 2004, pp. 88–90. Translated from Pis'ma v Zhurnal Tekhnicheskoĭ Fiziki, Vol. 30, No. 3, 2004, pp. 7–13.

The Interface Mechanism of Photoluminescence in Carbonized Porous Silicon

B. M. Kostishko*, Yu. S. Nagornov, S. Ya. Salomatin, and Sh. R. Atazhanov

Ul'yanovsk State University, Ul'yanovsk, Russia

** e-mail: kost@sv.uven.ru*

Received July 3, 2003

Abstract—The interface mechanism of photoluminescence (PL) in carbonized porous silicon is considered. The model involves processes in a heterojunction between *p*-Si and *p*-SiC nanodimensional grains and the interfacial SiO_x and $Si_xO_yC_{1-x-y}$ layers, where the radiative annihilation of charge carriers takes place. Irrespective of the size of nanograins, the bandgap width in the interfacial layers remains constant, which accounts for the fixed positions of red (1.8 eV) and blue-green (2.4 eV) PL bands observed in the experiment. The dimensions of nanograins were determined using X-ray diffraction and scanning tunneling microscopy. © *2004 MAIK "Nauka/Interperiodica"*.

The unique properties of porous silicon (por-Si) are related to a considerable extent to the presence of microscopic crystalline particles and, especially, nanodimensional grains with a size not exceeding 12 nm. However, the photoluminescence (PL) of por-Si in the visible spectral range is explained by several factors [1–7]. The most significant of these are the quantum confinement effect [1] and the presence of passivating layers of atoms and/or molecules (H, O, C, F) [2–7] or silicon oxide [3, 4] on the surface of por-Si. Atoms adsorbed on the surface form the centers of radiative recombination of the electron–hole pairs. In the presence of silicon oxide, the radiative recombination takes place in the interfacial layer representing a thin transition region between Si and SiO_2.

It was shown [4] that oxidation of various por-Si samples with PL bands in the 1.4–1.9 eV range leads to fixation of the PL band peak in the region of 1.7 eV. Kanemitsu *et al.* [3] obtained direct evidence for the interface PL model by showing that, irrespective of their dimensions, oxide-coated silicon nanograins exhibit PL with a peak at 1.7 eV. The results of *ab initio* numerical calculations confirmed that the bandgap width in the interfacial layer of SiO_x ($0 < x < 2$) is independent of the size of a Si grain and has a minimum value of 1.7 eV [3, 8]. Therefore, the position of the emission intensity maximum in the PL spectrum of oxidized por-Si samples is determined by the bandgap width in the interfacial oxide layer.

We have experimentally studied the process of carbonization in por-Si that leads to the appearance of a blue-green emission line in the PL spectrum, related to the formation of nanograins of a cubic modification of silicon carbide (3C-SiC) [5, 6]. This material offers important advantages: stable PL (not degrading even under the action of electron bombardment in the kilo-electronvolt energy range [5, 7]) and the possibility of modifying the PL spectrum by changing dopants and carbonization conditions. The results of our previous experimental and theoretical investigations showed that the light-emitting properties of the new material are determined by the heterojunction between *p*-Si and *p*-SiC nanograins [6, 9].

The aim of this experimental study was to elucidate in more detail the interface PL mechanism in carbonized por-Si.

The experiments were performed with carbonized por-Si samples prepared from the initial (100)-oriented *n*-Si wafers with a resistivity of 4.5 Ω cm. The porous structure was formed using a standard procedure of electrochemical etching in a mixed HF–C_2H_5OH (1 : 1) electrolyte for 30 min at a current density of 20 mA/cm^2. Then, the wafers with a porous layer were placed into a reactor and subjected to carbonization by treatment for various times (2–60 min) in a range of temperatures from 800 to 1350°C in a mixture of carbon-containing (CCl_4 vapor) and carrier (hydrogen) gases. During the carbonization process, the samples were also doped with gallium atoms to a concentration of 5×10^{17} cm^{-3}. The doping led to inversion of the conductivity type as compared to that of the initial por-Si.

The phase structure of the carbonized por-Si samples was studied by X-ray diffraction at room temperature on a DRON-3M diffractometer using CuK_α radiation. The room-temperature PL spectra were measured on a DFS-52 spectrometer at an excitation wavelength of λ = 325 nm. The sample surface topology was studied by scanning tunneling microscopy (STM) using a Solver P47-SPM-MDT instrument (NT-MDT Company). The surface chemical composition of the samples was studied by Auger electron spectroscopy (AES) with an 09IOS-10-005 spectrometer (Russia). The

1063-7850/04/3002-0088$26.00

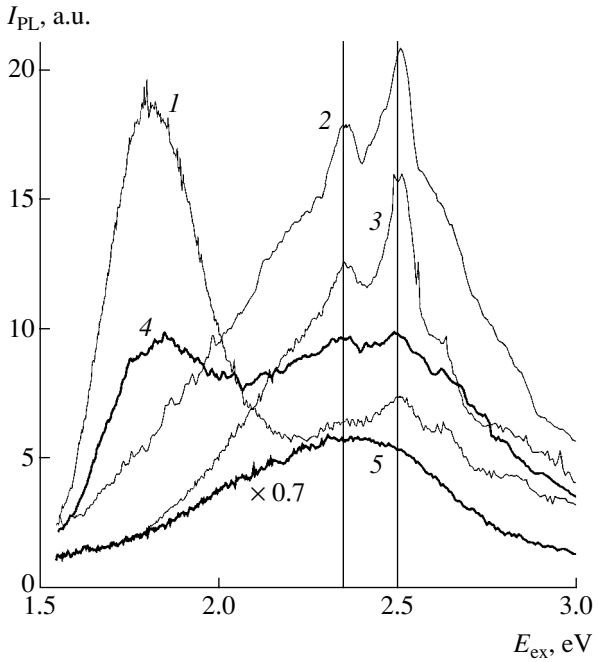

Fig. 1. The PL spectra of por-Si samples carbonized under various conditions: (*1*, *4*) 4 min at $T = 800$°C; (*2*) 60 min at $T = 1200$°C; (*3*) 2 min at $T = 1000$°C; (*5*) 60 min at $T = 1350$°C. Samples *1* and *2* were preliminarily oxidized for 48 h in water.

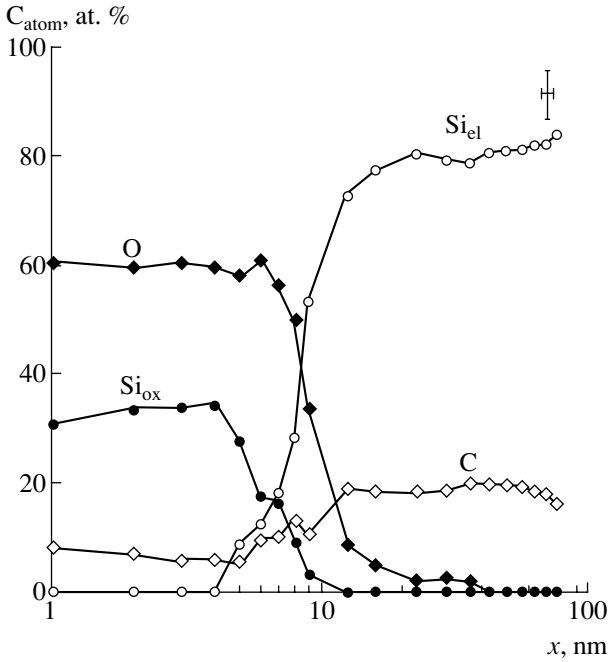

Fig. 2. The AES depth profiles of the atomic concentrations of elemental silicon (Si_{el}), oxidized silicon (Si_{ox}), carbon (C), and oxygen (O) in a carbonized single crystal silicon sample. In a small interfacial region, the x axis is presented on the logarithmic scale.

depth–composition profiles were obtained using AES in combination with etching by 4-keV argon ions. The ion etching rate, calibrated using samples with a thin SiO_2 film obtained by thermal oxidation, was about 0.3 nm/min.

The X-ray diffraction patterns of carbonized por-Si showed two peaks, with $2\theta = 41.3°$ and 90.2°, corresponding to the (200) and (400) reflections of the cubic modification of silicon carbide. The STM surface profile of a por-Si sample upon a short-time (4 min) carbonization treatment exhibits inhomogeneities having the form of characteristic grain-like protrusions with dimensions not exceeding 120 nm. The Raman scattering data allowed the average 3C-SiC grain size to be estimated at 5–6 nm [5–7].

Figure 1 shows the PL spectra of gallium-doped carbonized por-Si samples prepared under various conditions. The spectra display two emission bands: red (1.7–1.9 eV) and blue-green (22–2.7 eV). The former band vanishes in the samples upon carbonization for a prolonged time or at temperatures above 900°C (Fig. 1). This PL band is due to emission from the initial por-Si layer [5–7]. The blue-green emission band reproduces the PL spectrum of bulk silicon carbide [10] but is shifted by ~0.4 eV toward higher energies. The vertical lines in Fig. 1 indicate the positions of emission components due to LO, TO, and LA phonons and donor–acceptor (D–A) pairs considered previously [10]. The most remarkable fact is that carbonized por-Si samples treated for significantly different times (from 2 to 60 min) in a wide range of temperatures (800–1350°C) exhibit a PL peak fixed in the region of 2.4 eV (Fig. 1).

The obtained results can be explained proceeding from two alternative assumptions. According to the first model, the dimensions of SiC nanograins remain unchanged irrespective of the carbonization conditions. The quantum confinement effect leads to an increase in the bandgap width and to its rectification, which accounts for the observed fixed shift of the PL band. The second model suggests that the PL in carbonized por-Si, as well as that in the oxidized material, is determined by emission from the interfacial layer. The former assumption is inconsistent with the data of scanning tunneling microscopy and X-ray diffraction. Indeed, the STM profiles of a carbonized por-Si sample surface obtained from an area of 1.6×1.6 μm reveal SiC grains with various dimensions from 20 to 120 nm. The characteristic 3C-SiC grain size, estimated from a halfwidth of the X-ray diffraction peak, exhibited a 30% increase when the carbonization regime changed from 4 min at $T = 1200$°C to 60 min at $T = 1350$°C.

In order to verify the second model, which implies the existence of an interfacial layer, we performed the Auger depth profiling of a single crystal silicon sample carbonized for 40 min at $T = 1250$°C (Fig. 2). The concentrations of elements were calculated using the sensitivity factors preliminarily determined for the standard samples of SiC [11] and SiO_x [12]. The oxide stoichiometry was evaluated based on an analysis of the shape of the Auger electron peak of silicon. The region

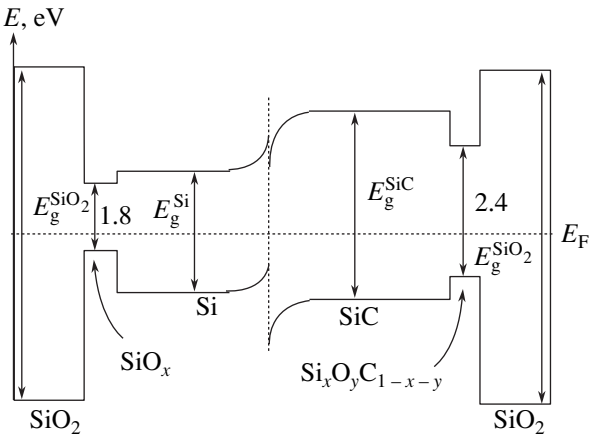

Fig. 3. The energy band diagram of a SiO_2–SiO_x–Si–(3C-SiC)–$Si_xO_yC_{1-x-y}$–SiO_2 heterostructure formed upon carbonization of porous silicon ($E_g^{SiO_2}$, E_g^{Si}, and E_g^{SiC} are the bandgap widths of silicon dioxide, silicon, and silicon carbide, respectively; E_F is the Fermi energy level).

of the depth–composition profile corresponding to the layer of adsorbed carbon and oxygen atoms is not depicted in Fig. 2.

As can be seen, the interfacial layer occurs at a depth from 6 to 10 nm and is characterized by the stoichiometric coefficient x varying from 1.8 to 0. Our results obtained for the carbonized single crystal silicon confirm the assumption of Gaily *et al.* [13] about $Si_xO_yC_{1-x-y}$ clusters covering silicon nanograins. An analysis of the depth-composition profiles showed that the coefficients x and y in the interfacial layer of $Si_xO_yC_{1-x-y}$ vary within x = 0.1–0.7 and y = 0.6–0.1 and the stoichiometric coefficient of carbon increases from 0.1 to 0.2.

Thus, the most adequate description of the whole body of our experimental results is provided by a model involving an interfacial layer between SiC and SiO_2 (Fig. 3). Based on this model, the mechanism of charge carrier generation and recombination in the system studied is as follows. Excitation leads to the generation of electron–hole pairs in Si and 3C-SiC nanograins. The minority carriers can be redistributed by the built-in electric field in the isotype heterojunction. The field strength depends on the bandgap widths E_g^{Si} and E_g^{SiC}. The role of the *p*-Si–*p*-SiC heterojunction, as determining the ratio of intensities of the red and blue-green PL lines, was previously considered in [9]. Then, the nonequilibrium carriers drift to the interfacial layer of SiO_x or $Si_xO_yC_{1-x-y}$ and exhibit radiative recombination. The bandgap widths of 1.8 and 2.4 eV for these interfacial layers correspond to the energies of maxima of the red and blue-green emission lines (Figs. 1 and 3).

Thus, we have demonstrated that the red and blue-green lines in the PL spectrum of carbonized porous silicon are fixed at 1.8 and 2.4 eV irrespective of the carbonization conditions (and, hence, of the dimensions of Si and 3C-SiC nanograins). A change in the size of these nanograins was confirmed by X-ray diffraction and STM data. An interface PL model for carbonized por-Si is proposed (Fig. 3) based on the SiO_2–SiO_x–Si–(3C-SiC)–$Si_xO_yC_{1-x-y}$–SiO_2 heterostructure involving a *p*-Si–*p*-SiC heterojunction and the interfacial layers of SiO_x or $Si_xO_yC_{1-x-y}$ featuring radiative recombination of charge carriers. The stoichiometry of the $Si_xO_yC_{1-x-y}$ interface was determined using the quantitative AES depth profiling of a carbonized silicon single crystal sample.

REFERENCES

1. A. G. Cullis, L. T. Canham, and P. D. J. Calcott, J. Appl. Phys. **82**, 909 (1997).
2. H. D. Fuchs, M. Stutzmann, M. S. Brandt, *et al.*, Phys. Rev. B **48**, 8172 (1993).
3. Y. Kanemitsu, T. Ogawa, K. Shiraishi, *et al.*, Phys. Rev. B **48**, 4883 (1993).
4. D. G. Qin, H. Z. Song, B. R. Zhang, *et al.*, Phys. Rev. B **54**, 2548 (1996).
5. B. M. Kostishko, Sh. R. Atazhanov, S. N. Mikov, *et al.*, Phys. Low-Dimens. Semicond. Struct., Nos. 7–8, 155 (1999).
6. B. M. Kostishko, Sh. R. Atazhanov, Yu. S. Nagornov, *et al.*, Phys. Low-Dimens. Semicond. Struct., Nos. 7–8, 47 (2000).
7. B. M. Kostishko, S. N. Mikov, Yu. S. Nagornov, *et al.*, Izv. Vyssh. Uchebn. Zaved., Élektronika **6**, 5 (1999).
8. P. Deak, M. Rosenbauer, M. Stutzmann, *et al.*, Phys. Rev. Lett. **69**, 2531 (1992).
9. B. M. Kostishko, Sh. R. Atazhanov, Yu. S. Nagornov, *et al.*, Phys. Low-Dimens. Semicond. Struct., Nos. 11–12, 1 (1999).
10. B. M. Kostishko, Yu. S. Nagornov, Sh. R. Atazhanov, and S. N. Mikov, Pis'ma Zh. Tekh. Fiz. **28**, 74 (2002) [Tech. Phys. Lett. **28**, 743 (2002)].
11. Sh. R. Atazhanov, B. M. Kostishko, and V. S. Gorelik, Kristallografiya **44**, 551 (1999) [Crystallogr. Rep. **44**, 509 (1999)].
12. B. M. Kostishko, S. V. Appolonov, A. E. Kostishko, *et al.*, Izv. Vyssh. Uchebn. Zaved., Mater. Élektron. Tekhn. **1**, 38 (2001).
13. P. V. Galiy, T. I. Lesiv, L. S. Monastyrskii, *et al.*, Thin Solid Films **318**, 113 (1998).

Translated by P. Pozdeev

Technical Physics Letters, Vol. 30, No. 2, 2004, pp. 91–93. Translated from Pis'ma v Zhurnal Tekhnicheskoĭ Fiziki, Vol. 30, No. 3, 2004, pp. 14–19.

The Acoustical Grüneisen Constants of Solids

V. N. Belomestnykh

Yurga Branch, Tomsk Polytechnical University, Yurga, Russia

e-mail: adm@ud.tpu.edu.ru

Received July 9, 2003

Abstract—An expression for the Grüneisen constants of solids is obtained involving only the velocities of propagation of the elastic waves. The new relation is applied for determining the Grüneisen constants of metals, ionic crystals, and ionic-molecular crystals. © *2004 MAIK "Nauka/Interperiodica".*

The elastic nonlinearity of condensed media is related to nonlinear acoustical properties via anharmonicity of interatomic (intermolecular) interactions. In solids, a measure of the anharmonicity of interactions between atoms and molecules is provided by the Grüneisen constant γ. This quantity controls a number of important physical processes (such as thermal expansion, thermal conductivity, absorption of acoustic waves, and the temperature dependence of elastic properties), enters into the equation of state, and reflects peculiarities of the phonon spectrum of a crystal [1].

In the Mie–Grüneisen equation of state for a crystal [1],

$$p = -\left(\frac{\partial E_0}{\partial V}\right)_T + \frac{\gamma}{V}(U - E), \tag{1}$$

the microscopic Grüneisen constant γ is given by the expression

$$\gamma = -\frac{d\ln\nu_j}{d\ln V} = -\frac{V}{\nu_j}\left(\frac{d\nu_j}{dV}\right)_T, \tag{2}$$

where p is the pressure, V is the volume, ν_j is the frequency of vibrations, $E_0 = U_0 + \sum_{j=1}^{3N} h\nu_j$, U_0 is the equilibrium potential energy of the crystal, and h is the Planck constant.

In the Debye theory, the frequencies ν_j are related to the acoustic wave velocity v by the expression

$$\frac{d\ln\nu_j}{d\ln V} = -\frac{1}{3} + \frac{d\ln v}{d\ln V}. \tag{3}$$

In solids, the velocities of propagation of the longitudinal and transverse waves (v_L and v_t, respectively) are different and, strictly speaking, the Debye equation of state should involve two Grüneisen constants, γ_L and γ_t. However, one quantity, γ_D, can be used in practice with sufficiently high precision by introducing the same truncation frequency ν_D for both longitudinal and transverse modes. The γ_D value is expressed via the coefficient of thermal expansion α, specific heat c_v, volume V, and compressibility χ by the Grüneisen relation [1]

$$\frac{\alpha}{\chi} = \gamma_D \rho c_v. \tag{4}$$

This relation is used for the experimental determination of γ_D, since all other values can be measured independently. In the physical acoustics of crystals, the most reliably measured quantity is the adiabatic bulk modulus B^S. In thermal physics, the most conveniently determined parameter is the molar heat capacity at constant pressure C_p. Using these values, the Grüneisen relation can be rewritten as

$$\gamma_D = \frac{\beta B^S \mu}{C_p \rho}, \tag{5}$$

where β is the temperature coefficient of volume expansion and μ is the molar mass. The value of γ_D determined from relation (5) is referred to as the thermodynamic Grüneisen constant.

The main idea in this study consists in that relation (5) can be represented in terms of the velocities of propagation of the acoustic waves, so that the Grüneisen constant would be determined using the acoustical data only. To this end, let us employ the well-known relation between the elastic and acoustical characteristics of crystals [2],

$$\rho v_L^2 = B^S + 4G/3, \quad \rho v_t^2 = G \tag{6}$$

(where G is the shear modulus), and a relationship between the deformation wave propagation velocity in solids and the ratio of the heat capacity to the temperature coefficient of thermal expansion [3],

$$v_1^2 = \frac{3}{2}\frac{C_p}{\beta\mu}, \tag{7}$$

where v_1 is the root-mean-square velocity calculated as

$$v_1 = \left(\frac{v_L^2 + 2v_t^2}{3}\right)^{1/2}.$$

Grüneisen constants of solids

Chemical elements and compounds	Velocity of sound, m/s		Grüneisen constants	
	υ_L	υ_t	γ_a	γ_D
Ag	3686	1677	2.30	2.4 [1]; 2.4; 2.5 [4]
Al	6422	3235	1.98	2.34 [1]; 2.43 [5]; 2.11 [6]
Au	3361	1239	2.90	3.0 [1]; 2.80 [6]
Cu	4726	2298	2.09	2.00 [1]; 1.96; 1.9 [4]; 2.06 [6]
Ni	5894	3219	1.70	1.88; 2.2 [4]; 1.73 [6]
Pd	4954	1977	2.47	2.23; 2.4 [4]
Pb	2158	860	2.69	2.92 [6]
W	5233	2860	1.70	1.62; 1.7 [4]
Be	13003	8967	0.84	0.83 [6]
Co	5827	3049	1.85	1.87; 2.1 [4]
Mg	5898	3276	1.64	1.41 [5]
Fe	6064	3325	1.68	1.60; 1.68 [4]; 1.66 [5]
Pt	3960	1670	2.53	2.54; 3.3 [4]
Ta	4147	2039	2.06	1.73
Th	2900	1583	1.70	1.54
Y	4106	2383	1.48	1.25
Zn	4117	2350	1.54	2.00
U	3422	2105	1.29	1.62
LiF	7323	4518	1.26	1.34; 1.75 [7]
NaF	5666	3330	1.44	1.72 [7]
KF	4641	2587	1.63	1.45; 1.73 [7]
RbF	3948	2132	1.74	1.41 [7]
LiCl	5260	3058	1.48	1.52; 1.78 [7]
NaCl	4666	2755	1.42	1.62; 1.74 [7]; 1.46
KCl	4090	2312	1.58	1.60 [7]
RbCl	3077	1658	1.75	1.53 [7]
LiBr	3621	2072	1.53	1.70; 2.02 [7]
NaBr	3284	1885	1.52	1.56; 1.81 [7]
KBr	3075	1695	1.67	1.68; 1.58 [7]
RbBr	2591	1403	1.73	1.37; 1.50 [7]
LiJ	2846	1608	1.58	2.22 [7]
NaJ	2889	1639	1.56	1.90 [7]
KJ	2623	1469	1.61	1.63; 1.72 [7]
RbJ	2245	1198	1.78	1.41; 1.73 [7]
AgCl	3145	1207	2.79	2.02
AgBr	2845	1159	2.63	2.33
TlCl	2265	1153	1.94	2.60
TlBr	2133	1085	1.94	2.47
NaCn	3600	960	3.57	
KCN	3340	1170	3.04	
NaN_3	3460	1350	2.75	4.25
$NaClO_3$	4240	2380	1.65	1.36
$NaClO_4$	3970	2200	1.65	
$NaNO_2$	3880	2400	1.25	
$NaNO_3$	4510	2580	1.53	
$KBrO_3$	3280	1780	1.16	
NH_4ClO_4	3800	2130	1.61	1.81

Notes: The values of velocities were taken from [2, 8–10]. The values of γ_D without reference were calculated by the author using the values of β, B^S, C_p, and ρ taken from [2, 11–13].

Using formulas (6) and (7), we obtain a relation between the Grüneisen constant and the velocities of acoustic waves:

$$\gamma_a = \frac{9(v_L^2 - 4v_t^2/3)}{2(v_L^2 + 2v_t^2)}. \quad (8)$$

The Grüneisen constant γ_a given by expression (8) will be referred to as acoustical. Now, let us compare the values of the acoustical and thermodynamic Grüneisen constants determined under standard temperature and pressure conditions ($T = 298.15$ K, $p = 1.013 \times 10^5$ Pa).

As can be seen from data presented in the table, there is a quite satisfactory agreement between γ_a and γ_D values for the given group of substances. There are certain points for special consideration. In particular, the values of Grüneisen constants for sodium azide (NaN_3) may appear at first glance to be rather high. However, it is known [14] that the standard conditions are critical for the given compound, in which a smeared structural transformation takes place at $T_c = 292.7$ K and atmospheric pressure. This transformation is manifested, in particular, by a λ peak in the $C_p(T)$ curve. For substances whose Grüneisen constants are reasonably described by formula (8), this relation makes it possible to employ purely acoustical measurements for studying the orientational dependence of γ, the influence of external energetic factors, and some other aspects.

On the other hand, it would be oversimplification to believe that relation (8) can be used to determine the Grüneisen constants for the whole variety of solids. Preliminary investigations revealed a significant difference between γ_a and γ_D values of some substances. For example, in rare earth elements, γ_a values are on the average two times greater than γ_D; for some other elements, including bismuth, cadmium, and zinc, γ_a are one and a half times smaller than γ_D. It should be noted, however, that there are large groups of substances in which the ratio γ_a/γ_D is constant. Rationalization of this pattern will require additional investigation.

REFERENCES

1. L. Zhirifal'ko, *Statistical Physics of Solid* (Mir, Moscow, 1975).
2. I. N. Frantsevich, F. F. Voronov, and S. A. Bakuta, *Elastic Constants and Elastic Moduli of Metals and Nonmetals: A Handbook* (Naukova Dumka, Kiev, 1982).
3. K. L. Leont'ev, Akust. Zh. **27**, 554 (1981) [Sov. Phys. Acoust. **27**, 309 (1981)].
4. C. Kittel, *Introduction to Solid State Physics* (Wiley, New York, 1976; Nauka, Moscow, 1978).
5. K. P. Rodionov, Fiz. Met. Metalloved. **26**, 1120 (1969).
6. S. R. Urzendowski and A. N. Guenther, in *Proceedings of the International Symposium on Thermal Expansion of Solids, 1974*, pp. 256–277.
7. K. G. Bansigir, J. Appl. Phys. **39**, 4024 (1968).
8. *Physical Acoustics: Principles and Methods*, Vol. 3, Part B: *Lattice Dynamics*, Ed. by W. P. Mason (Academic Press, New York, 1965; Mir, Moscow, 1973).
9. V. N. Belomestnykh, *Physicochemical Acoustics of Crystals* ("TROTs," Tomsk, 1998).
10. V. N. Belomestnykh, Yu. P. Pokholkov, V. L. Ul'yanov, *et al.*, *Elastic and Acoustic Properties of Ion Ceramic Insulators and High-Temperature Superconductors* (STT, Tomsk, 2001).
11. *Tables of Physical Quantities*, Ed. by I. K. Kikoin (Atomizdat, Moscow, 1976).
12. *Chemist's Handbook*, 3rd ed. (Khimiya, Leningrad, 1971), Vols. 1, 2.
13. V. A. Ryabin, M. A. Ostroumov, and T. F. Svit, *Thermodynamic Properties of Materials: A Handbook* (Khimiya, Leningrad, 1977).
14. V. N. Belomestnykh, M. N. Grineva, and S. R. Sharov, Zh. Fiz. Khim. **55**, 503 (1981).

Translated by P. Pozdeev

Technical Physics Letters, Vol. 30, No. 2, 2004, pp. 94–95. Translated from Pis'ma v Zhurnal Tekhnicheskoĭ Fiziki, Vol. 30, No. 3, 2004, pp. 20–23.

The Selective Effect of a Constant Magnetic Field on the Crystallization of Flexible-Chain Polymers

M. N. Levin*, V. V. Postnikov, and E. D. Kolesnikova

Voronezh State University, Voronezh, Russia

** e-mail: levin@lev.vsu.ru*

Received July 29, 2003

Abstract—A weak constant magnetic field produces a selective action upon crystallization of a high-molecular-mass poly(ethylene oxide) which is a model crystallizable flexible-chain polymer with polar units.

Previously [1–3], we observed changes in the kinetics of crystallization of high-molecular-mass organosiloxanes and poly(ethylene oxide) after pretreatment of their melts by exposure to a pulsed magnetic field. The effect was explained by crosslinking of the polymer chains as a result of the spin-dependent radical reactions of terminal units and/or groups with weak double bonds. It was believed that the pulsed regime of the magnetic field action was a necessary condition for realization of the proposed mechanisms.

In this Letter, we report on the effect of the melt pretreatment in a weak constant magnetic field on the crystallization of flexible-chain polymers.

The linear crystallizable flexible-chain polymer was represented by a high-molecular-mass poly(ethylene oxide) (PEO) with an average molecular mass of $M = 1 \times 10^5$ (PEO-100). The samples had the form of PEO-100 layers inside a ring with a diameter of $D = 2$ cm made of a 100-μm-thick polyimide film pressed between copper electrodes. The temperatures of PEO-100 crystallization (T_c) and melting (T_m) were determined indirectly as the positions of jumps in the temperature dependence of the active component of the permittivity $\varepsilon'(T)$. The sample permittivity was measured at a frequency of $\omega = 10^4$ Hz using a Tesla BM 484 bridge. The samples before and after treatment in the magnetic field were cooled and heated at a constant rate of $\beta = (5.00 \pm 0.02) \times 10^{-2}$ K/s.

The melt of PEO-100 heated to $T = 350$ K prior to crystallization was treated for 30 min in a constant magnetic field (CMF) with the induction B varied in the interval from 0.02 to 0.32 T. For the comparison, identical polymer samples were treated at the same temperature of the melt ($T = 350$ K) for 30 s by a pulsed magnetic field (PMF) representing a series of $N = 1500$ triangular pulses with a duration of $\tau = 20$ μs and a repetition rate of $f = 50$ Hz.

It was found that pretreatment of the melt of PEO-100 in the CMF and PMF leads to opposite changes in the temperatures of crystallization and melting of the polymer (Fig. 1). The PMF action leads to an increase in T_c and a decrease in T_m, whereas the CMF treatment reduced T_c and increased T_m. The behavior of changes in the crystallization and melting temperatures of PEO-100 as functions of the magnetic induction B was also different for the PMF and CMF treatments.

Figure 2 shows the plots of increment of the interval between the melting and crystallization temperatures, $\Delta T = (T_m - T_c) - (T_{m0} - T_{c0})$, versus the magnetic induction B. Here, T_{c0}, T_{m0} are the values of the crystallization and melting temperatures, respectively, before treatment of the melt in a magnetic field and T_c, T_m are the corresponding values after the treatment. In the case of PMF, B refers to the pulse amplitude value B_0.

As can be seen, an important peculiarity of the ΔT behavior in the case of pulsed magnetic fields was that the PMF effect was manifested in a narrow interval of the magnetic induction; that is, the polymer response was selective with respect to the field magnitude. Taking into account that the PMF-induced increase in T_c and decrease in T_m of PEO-100 are related to the crosslinking of polymer chains (see, e.g., [2]), we may

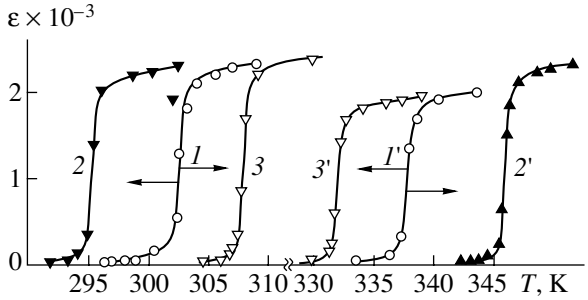

Fig. 1. Temperature dependences of the dielectric permittivity ε' during crystallization (*1*–*3*) and melting (*1*'–*3*') of PEO-100 samples: (*1*, *1*') in the initial state; (*2*, *2*') after CMF treatment of the melt; (*3*. *3*') after PMF treatment of the melt.

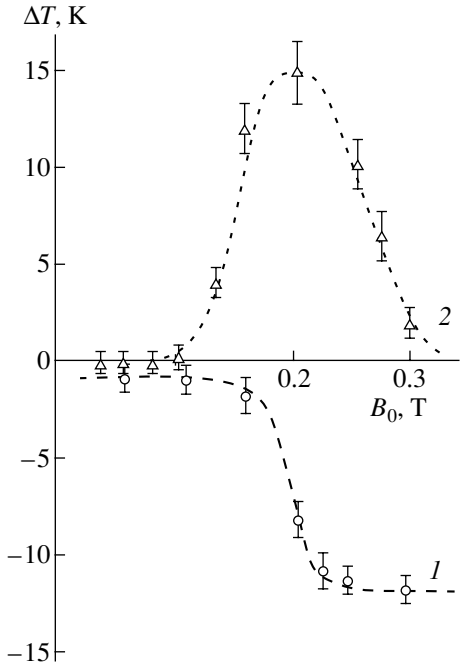

Fig. 2. The increment ΔT of the interval between the melting and crystallization temperatures as a function of the magnetic induction for PEO-100 melt pretreated in a (*1*) pulsed and (*2*) constant magnetic field.

suggest that the opposite behavior (a decrease in T_c and an increase in T_m) observed in the constant magnetic field are related to a decrease in the magnitude of interaction between the polymer chains. This assumption agrees with the notions about the CMF-induced breakage of "physical nodes," by which we imply the local regions of strong nonchemical interactions between atomic groups of the neighboring molecules and most close-packed regions of the adjacent molecular chains [4].

The mechanism of the CMF action on the intermolecular forces in polymer chains is unclear. However, the selective character of the observed effect with respect to the magnetic field magnitude suggests that this mechanisms differs from the usual orientation of the polymer chain units possessing anisotropic diamagnetic susceptibilities.

REFERENCES

1. M. N. Levin and N. N. Matveev, Zh. Fiz. Khim. **75**, 1886 (2001).
2. M. N. Levin, V. V. Postnikov, and N. N. Matveev, Vysokomol. Soedin., Ser. A **45**, 217 (2003).
3. M. N. Levin, V. V. Postnikov, and N. N. Matveev, Zh. Fiz. Khim. **77**, 758 (2003).
4. N. N. Peschanskaya, V. Yu. Surovova, and P. N. Yakushev, Fiz. Tverd. Tela (St. Petersburg) **34**, 2111 (1992) [Sov. Phys. Solid State **34**, 1127 (1992)].

Translated by P. Pozdeev

Technical Physics Letters, Vol. 30, No. 2, 2004, pp. 96–98. Translated from Pis'ma v Zhurnal Tekhnicheskoĭ Fiziki, Vol. 30, No. 3, 2004, pp. 24–30.

The Combustion of Benzene in a Supercritical Water

A. A. Vostrikov* and S. A. Psarov

Kutateladze Institute of Thermal Physics, Siberian Division, Russian Academy of Sciences, Novosibirsk, Russia

** e-mail: vostrikov@itp.nsc.ru*

Received August 4, 2003

Abstract—We have studied the kinetics of benzene combustion in an aqueous solution at supercritical temperatures (663 K ≤ T ≤ 1075 K) and pressures (28 MPa ≤ P ≤ 90 MPa). The oxidative combustion exhibits an explosive character and can develop according to either thermal or branched-chain mechanisms. The conditions for these mechanisms are established and the corresponding kinetic constants are determined. © *2004 MAIK "Nauka/Interperiodica".*

In recent years, basic principles have been extensively developed for use of the unique properties of water under supercritical pressures (P > 22.1 MPa) and temperatures (T > 647 K) in essentially new, ecologically safe technologies for the conversion of organic matter, low-grade fuel (heavy oil residue fractions, coals), and various wastes into valuable hydrocarbons, fuel, and thermal energy [1–8]. In particular, it was suggested [6] to use the process of combustion of a low-grade fuel directly in supercritical water (SCW), thus obtaining a high-enthalpy vapor-gas working body for thermal power plants.

The unique property of SCW consists in that it is a universal solvent for both organic matter (OM) and oxygen (O_2), while partly retaining the properties of liquid water. For example, SCW at T = 663 K and P = 30 MPa has a density of ρ = 0.47 g/cm^3 [9] and a static permittivity of ε = 12 [10]. The free radical mechanism of the OM conversion in SCW and relatively low temperatures (T < 1000 K) required for these reactions exclude the formation of oxygen-containing organic compounds and harmful oxides, while heteroatoms such as Cl, S, and P are converted into low-volatile inorganic substances [11].

In this study, we have measured for the first time the kinetics of the explosive oxidation (combustion) of benzene dissolved in SCW with O_2 and established the mechanisms and determined the kinetic constants of the oxidation process.

The experiments consisted in automated continuous monitoring of the solution pressure in a reactor before and after benzene injection into SCW or an SCW–O_2 mixture. Benzene was injected along the reactor axis via a plunger valve at a pressure of 90 MPa and a temperature of 500 K. The reactor channel had a diameter of 10 mm and a volume of 10.3 cm^3. The pressure was measured with a fast-response (10-kHz) membrane strain gauge [6]. After termination of the combustion process, the composition of reaction products was analyzed using a quadrupole mass spectrometer [11].

In preliminary experiments, we studied the rate of benzene dissolution after injection into the reactor with SCW. Figure 1a shows how the solution pressure P_s

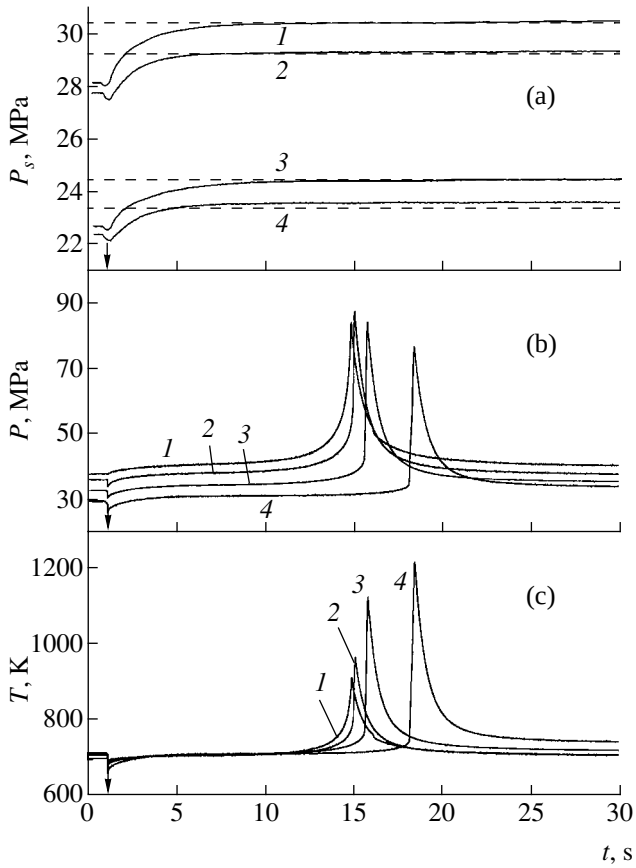

Fig. 1. Time variation of (a) the solution pressure P_s and the reaction mixture (b) pressure P and (c) temperature T for benzene combustion in SCW under various conditions (see the text). Arrows indicate the moment of cold benzene injection into the reactor with SCW.

1063-7850/04/3002-0096$26.00 © 2004 MAIK "Nauka/Interperiodica"

varies with the time t after injection. Curves *1–4* refer to the temperatures T = 673, 674, 654, and 651 K and the concentrations of benzene 0.6, 0.6, 0.37, and 0.27 mol/l and water 15.1, 13.5, 15.1, and 15.1 mol/l, respectively. As can be seen from these kinetic curves, the pressure P_s quite rapidly reaches a stationary level. The stationary pressure values are well described by the Redlich–Kwong equation written assuming the classical mixing rule [12] (dashed lines in Fig. 1a). It should be noted that the same equation adequately described the $P_s(T)$ curves for SCW mixtures with O_2 and CO_2 (oxidation product) in the range of oxidation parameters studied.

The reaction products predominantly (>97%) consisted of CO_2 and H_2O (the remainder included CH_4, CO, H_2, C_7H_8, and C_8H_{10}). This ensured reliable determination of the heat capacity of the mixture and of the thermal effect $H(T)$ of the oxidation reaction based on the tabulated data [13]. Under these conditions, the $P(T)$ curves measured in the course of oxidation could be used for determining the temperature in the reactor $T(t)$. The $P(t)$ and $T(t)$ curves depicted in Figs. 1b and 1c refer to the concentrations of benzene 0.183, 0.349, 0.360, and 0.360 mol/l; oxygen 0.838, 0.691, 0.591, and 0.607 mol/l; and water 13.49, 12.50, 8.35, and 6.79 mol/l, respectively. As can be seen, the content of O_2 corresponds to a partial oxidation of benzene.

Using the $T(t)$ curves, we also determined the amount of heat $Q(t)$ corresponding to the mixture temperature variations in the reactor. The heat losses $Q_r(T)$ through the reactor wall were determined using the right-hand branches of the $T(t)$ curves corresponding to cooling of the reaction mixture after termination of the combustion process. As a result, we determined the heat evolution with time $Q_c(t) = Q(t) + Q_r(T(t))$. Using the $Q_c(t)$ and $H(T)$ values, it is easy to calculate the rate of benzene oxidation in SCW as $W(t) = (dQ_c(t)/dt)/H(T)$. An analogous approach was previously used for the analysis of the combustion of naphthalene and heavy oil residue in SCW [6]. In this study, the $W(t)$ curves were calculated for 15 sets of initial conditions. Figure 2 presents the $W(t)$ curves *1–4* corresponding to the $P(t)$ and $T(t)$ kinetics depicted by curves with the same numbers in Figs. 1b and 1c.

Analysis showed that some of the $W(t)$ curves contain break points related to the jumps in W. The positions of the first jump are indicated by black circles in Fig. 2. These features in the behavior of $W(t)$ are related to a change in the mechanism of benzene oxidation in SCW, by analogy with the changes observed for the hydrocarbon oxidation in the gas phase [14, 15].

In the region of parameters of the reaction mixture observed for the time before the first jump in W, the behavior of $W(t)$ is determined primarily by the oxidation of C_6H_6 via the reaction with O_2 (stationary oxidation regime). In this regime, the oxidation rate $W(t)$ is described in terms of a global reaction equation in the

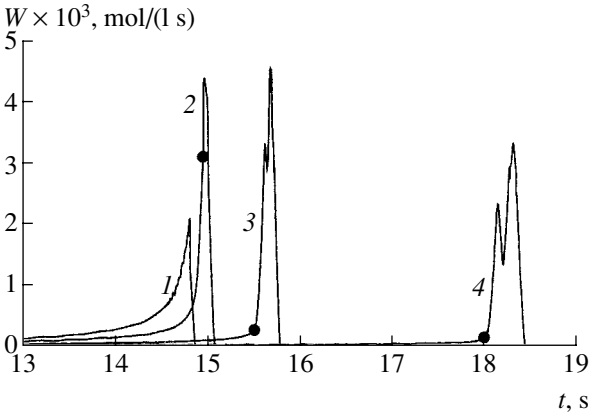

Fig. 2. The kinetic curves $W(t)$ of benzene oxidation in SCW with oxygen under the conditions corresponding to the $P(t)$ and $T(t)$ curves with the same numbers in Figs. 1b and 1c.

form [2] taking into account the influence of the nonideality of SCW on the reaction activation energy:

$$W = A\exp\left(-\frac{E_0 - E(\varepsilon)}{RT}\right)\prod_i [n_i]^{\Theta_i}. \qquad (1)$$

Here, $E_a = E_0 - E(\varepsilon)$ is the activation energy, $[n_i]$ is the concentration of the ith reagent, and Θ_i is the reaction order with respect to the ith reagent. The quantity $E(\varepsilon)$ allows for a change in the energy of the activated complex in the reaction of C_6H_6 oxidation by oxygen in SCW, which is related to manifestations of the polar properties of water. The $E(\varepsilon)$ value was determined by the formula [16]

$$E(\varepsilon) = \alpha\frac{\varepsilon - 1}{2\varepsilon + 1}, \qquad (2)$$

where $\alpha = \mu^2/r^3$, μ is the dipole moment of the activated complex, and r is the effective radius of the activated complex in solution. The coefficient α was used as a fitting parameter, and the values of ε for various T and ρ were taken from reference data [10].

The results of fitting by least squares showed that the experimental curves of $W(t)$ for the times corresponding to oxidation in the stationary regime are most adequately described by the following expression:

$$W = 10^{10.0\pm0.3}\exp\left(-\frac{205\pm4}{RT} + \frac{55\pm3}{RT}\frac{\varepsilon - 1}{2\varepsilon + 1}\right) \times [C_6H_6]^{0.16\pm0.03}[O_2]^{0.94\pm0.07}. \qquad (3)$$

In Eqs. (1)–(3), the oxidation rate W is expressed in [mol/(l s)], the concentrations $[C_6H_6]$ and $[O_2]$ in [mol/l], and the activation energy E_a in [kJ/mol].

The jumps in $W(t)$ indicated by the black circles in Fig. 2 is related to the transition to a faster, nonstation-

ary oxidation of C_6H_6 by active species in the reaction medium. These species, formed in the reactions of oxygen with intermediate oxidation products, are capable of initiating oxidation according to the branched-chain mechanism [14, 15]. A boundary condition for the passage from stationary to nonstationary regime of oxidation is the equality of the branching rate k_+ and the chain termination rate k_- [14].

Since the active species are formed in the reactions involving O_2 [15], with the excess of C_6H_6, we may assume that $k_+ = A_+\exp(-E_+/RT)[O_2]$. Then, taking into account that quenching of the active species is an activationless process ($E_a = 0$) determined by the pair collisions with H_2O molecules, we can assume that $k_- = A_-[H_2O]$. Taking the logarithms of these expressions and using the condition of their equality, we eventually obtain

$$\ln(A^*) - \frac{E_+}{RT^*} = \ln\left(\frac{[H_2O]}{[O_2]}\right), \qquad (4)$$

where $A^* = A_+/A_-$ and $T = T^*$ is the temperature of the transition from stationary to nonstationary oxidation regime.

Applying the least squares method to the experimental data corresponding to black circles on the $W(t)$ curves in Fig. 2, we obtained the following values of the kinetic constants: $A^* = 10^{(6.8 \pm 0.3)}$ and $E_+ = 80 \pm 3$ kJ/mol. It should be noted that the energy E_+ of the partial oxidation of C_6H_6 in SCW falls within the region of values reported previously, 90 kJ/mol [14] and 75–87 kJ/mol [15], for the gas phase oxidation of benzene under the conditions corresponding to the first jump in $W(t)$.

Substituting the above values of A^* and E_+ into Eq. (4), we may readily the dependence of T^* on the relative concentration $[H_2O]/[O_2]$ for the partial oxidation of benzene with oxygen in SCW. Using the kinetic constants determined in this study, it is possible to calculate the energy parameters of a stationary combustion process and to determine conditions for the passage to a nonstationary benzene combustion in SCW.

Acknowledgments. This study was supported by the Russian Foundation for Basic Research (project no. 01-02-17372) and the Ministry of Education of the Russian Federation (project no. TO2-9.1-2120 for Basic Research in Technical Sciences).

REFERENCES

1. T. D. Thornton and Ph. E. Savage, AIChE J. **38**, 321 (1992).
2. Ph. E. Savage, Chem. Rev. **99**, 603 (1999).
3. J. L. DiNaro, J. W. Tester, J. B. Howard, *et al.*, AIChE J. **46**, 2274 (2000).
4. A. A. Vostrikov, D. Yu. Dubov, and S. A. Psarov, Izv. Akad. Nauk, Ser. Khim. **8**, 1406 (2001).
5. A. A. Vostrikov, D. Yu. Dubov, and S. A. Psarov, Izv. Akad. Nauk, Ser. Khim. **8**, 1409 (2001).
6. A. A. Vostrikov and S. A. Psarov, Pis'ma Zh. Tekh. Fiz. **28** (18), 54 (2002) [Tech. Phys. Lett. **28**, 776 (2002)].
7. M. J. Antal, Jr., S. G. Allen, D. Schulman, *et al.*, Ind. Eng. Chem. Res. **39**, 4040 (2000).
8. C. Martino and Ph. E. Savage, Ind. Eng. Chem. Res. **38**, 1775 (1999).
9. *IAPWS Industrial Formulation 1997 for the Thermodynamic Properties of Water and Steam*, Ed. by R. B. Dooley (Electric Power Research Institute, Palo Alto, 1999), p. 48.
10. *Release of Static Dielectric Constant of Ordinary Water Substance for Temperatures from 238 K to 873 K and Pressures up to 1000 MPa*, Ed. by R. B. Dooley (International Association for the Properties of Water and Steam, Erlangen, 1997).
11. A. A. Vostrikov, D. Yu. Dubov, and S. A. Psarov, *Chemistry of Oil and Gas* (STT, Tomsk, 2000), Vol. 2, pp. 492–496.
12. N. Akinfiev and A. Zotov, Geochim. Cosmochim. Acta **63**, 2025 (1999).
13. *Physicochemical Properties of Individual Hydrocarbons*, Ed. by V. M. Tatevskiĭ (Gostoptekhizdat, Moscow, 1960).
14. N. N. Semenov, *Advancement of Theory of Chain Reactions and Thermal Ignition* (Znanie, Moscow, 1969).
15. A. S. Sokolik, *Spontaneous Ignition, Flame, and Detonation in Gases* (Izd. Akad. Nauk SSSR, Moscow, 1960).
16. K. A. Connors, *Chemical Kinetics: The Study of Reaction Rates in Solution* (VCH Publ., New York, 1990).

Translated by P. Pozdeev

Technical Physics Letters, Vol. 30, No. 2, 2004, pp. 99–101. Translated from Pis'ma v Zhurnal Tekhnicheskoĭ Fiziki, Vol. 30, No. 3, 2004, pp. 31–38.

The Temperature Dependence of the Strength of Adhesion between Epoxy-Rubber Glues and Steels

V. I. Vettegren[a,*], A. Ya. Bashkarev[b], and V. A. Sytov[c]

[a] *Ioffe Physicotechnical Institute, Russian Academy of Sciences, St. Petersburg, 194021 Russia*
[b] *St. Petersburg State Technical University, St. Petersburg, 195251 Russia*
[c] *Central Research Institute for Materials, St. Petersburg, Russia*
** e-mail: Victor.Vettegren@mail.ioffe.ru*

Received July 31, 2003

Abstract—We have studied the temperature dependence of the strength of adhesion between epoxy-rubber glues and steel 45 measured at a fixed loading rate. It is established that the adhesion strength σ exhibits a linear decrease with increasing temperature, predicted by the kinetic theory of fracture, only in the temperature interval between the characteristic values T_t and T_b. Below T_t, the adhesion strength is independent of the temperature, while at $T > T_b$, the slope of the $\sigma(T)$ curve decreases with increasing temperature. Deviations from the kinetic theory predictions are explained by a change in the fracture mechanism (with tunneling transitions being involved in the fracture at low temperatures) and by variation of the parameter γ (at elevated temperatures). The values of the activation energy and activation volume of the fracture are determined. © *2004 MAIK "Nauka/Interperiodica".*

Introduction. The adhesion strength σ is one of the main characteristics of glue joints. As is known [1–6], the strength of adhesion between metals, crystals, polymers, etc., is related to the temperature T and the time to fracture (lifetime) τ by the Zhurkov equation

$$\sigma = \frac{U_0}{\gamma} - \frac{k_B T}{\gamma} \ln \frac{\tau}{\tau_0}, \quad (1)$$

where $\tau_0 \approx 10^{-13}$ s, U_0 is the activation energy for the rupture of interatomic bonds, γ is a parameter related to the activation volume of bond rupture, and k_B is the Boltzmann constant. Literature devoted to the analysis of this equation for glue joints is very restricted and contradictory [7–12]. There are numerous and considerable deviations from this relationship in the range of normal and elevated temperatures, the nature of discrepancies being unknown. The lifetime of glue joints at negative temperatures (Celsius scale) was not studied.

According to Eq. (1), the adhesion strength at a fixed lifetime must exhibit a linear decrease with increasing temperature. The aim of this study was to verify this prediction for the adhesion between epoxy-rubber glue and steel 45.

Experimental. We have studied the temperature dependence of the adhesion strength between steel 45 and a series of glues [13, 14]: KDS-19 (a block copolymer of epoxidian resin, butadiene-nitrile carboxylated rubber, and *metha*-tri(carborane sebacate)glycide); KG-1m (a block copolymer of epoxidian resin, butadiene-nitrile carboxylated rubber, and a silicon-containing oligomer); K-300 (an organosilicon resin cured with a low-molecular-weight polymer); KVS-31 (a block copolymer of epoxidian resin, low-molecular-weight butadiene-nitrile rubber with terminal carboxy groups); Cryosil (epoxy-organosilicon glue).

The samples comprised pairs of steel cylinders with a diameter of 1 cm and a length of 2.5 cm glued together with their edge faces. Prior to gluing, the edge faces of the cylinders were mirror finished by polishing with a GOI paste. Then, a layer of glue was applied and the cylinders were placed into a special device ensuring matching of the cylinder axes and providing for the required pressing load. Until termination of the glue polymerization process, the samples were kept in this device for 24 h at room temperature and then for 5 h at 365 K. The glue layer thickness after thermal treatment was about 1 mm.

The glued samples were tensile tested at a loading rate of $d\sigma/dt = \dot{\sigma} \approx 5$ MPa/min in a special laboratory lever device. The time to fracture was within 5–15 min. No less than 5 samples were tested at each fixed temperature, after which the results were averaged. The scatter of adhesion strengths measured at each fixed temperature did not exceed 5%.

Experimental results. The typical temperature dependences of the adhesion strength (fracture stress) are illustrated in the figure for the joints of steel 45 with glues KVS-31 and K-300. The curves observed for the joints with other glues exhibit qualitatively the same behavior.

1063-7850/04/3002-0099$26.00 © 2004 MAIK "Nauka/Interperiodica"

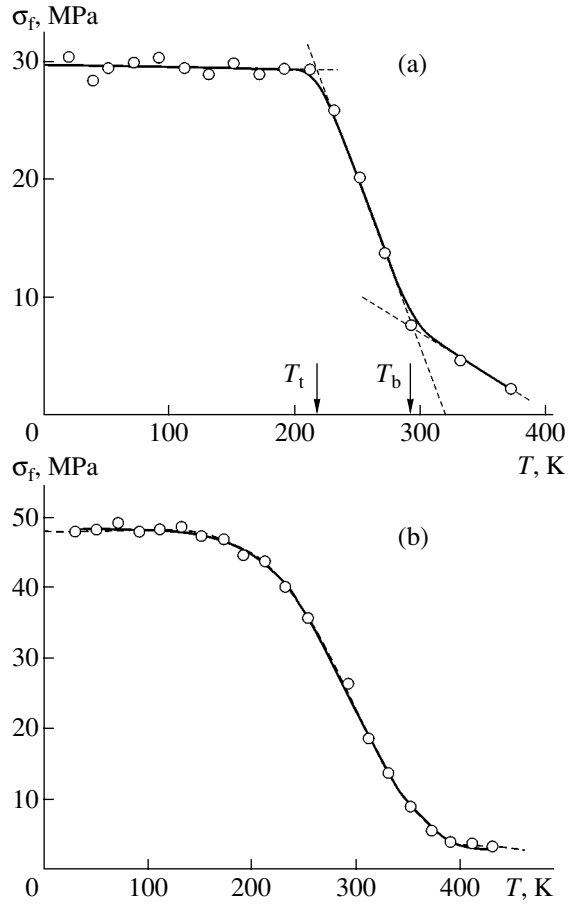

Temperature dependence of the strength of adhesion of glues (a) KVS-31 and (b) K-300 to steel 45.

As can be seen from the figure, the experimental curves can be divided into three regions. In the first region, extending from 20 K up to the first characteristic temperature T_t, the adhesion strength is independent of the temperature. In the second region, confined between the two characteristic temperatures T_t and T_b, the strength decreases linearly with increasing temperature. The third region, $T > T_b$, is characterized by the slope of the experimental curve gradually decreasing with an increase in the temperature. The values of characteristics temperatures T_t ad T_b for various glues are given in the table.

Characteristic temperatures (T_t and T_b) and parameters of fracture of the adhesion joints between steel and various epoxy-rubber glues

Glue	T_t, K	T_b, K	U_0, kJ/mol	γ_t, nm^3
K-300	220	360	110	1.8
KVS-31	220	295	150	1.7
Cryosil	265	>400	105	1.7
KDS-19	195	315	125	2.8
KG-1m	155	400	115	

Discussion of results. First, let us consider the temperature interval in which the strength of glue joints linearly decreases with increasing temperature. This region is of most interest for technical applications.

The temperature dependence of the adhesion strength under the conditions of a constant loading rate can be described using Eq. (1) and the Baily criterion of damage addition [5, 6]:

$$\int_0^{t_f} \frac{dt}{\tau[\sigma(t), T]} = 1, \qquad (2)$$

where t_f is the time to fracture. Since $\exp(\gamma\sigma_t/k_BT) \gg 1$, this condition can be rewritten as

$$\sigma_f(T) \approx \frac{U_0}{\gamma} + \left[\frac{k_B}{\gamma}\ln\left(\frac{\gamma\dot{\sigma}\tau_0}{k_BT}\right)\right]T, \qquad (3)$$

where σ_f is the fracture stress. For $\gamma\dot{\sigma}\tau_0/(k_BT) \ll 1$, we have $\ln[\gamma\dot{\sigma}\tau_0/(k_BT)] < 0$ and, hence, the adhesion strength decreases with increasing temperature.

The values of γ for the samples studied amount to a few cubic nanometers. As the temperature varies in the range 20–400 K, the value of $\ln[k_BT/(\gamma\dot{\sigma}\tau_0)]$ changes from ≈29 to ≈35, amounting on the average to $\approx 32 \pm 3$. Therefore, under the conditions studied, relation (3) is conveniently rewritten as

$$\sigma_f(T) \approx \frac{U_0}{\gamma} - 32\frac{k_B}{\gamma}T. \qquad (4)$$

According to this formula, the adhesion strength has to be approximately a linear function of the temperature, in agreement with what is observed in the interval between T_t and T_b. Let us use this expression for calculating the activation energy U_0 and the activation volume parameter γ.

The straight line intersects the temperature axis at the point T_* corresponding to zero strength. At this point, Eq. (4) yields

$$U_0 \approx 32k_BT_*. \qquad (5)$$

Upon determining the slope of the straight line, $\Delta\sigma_f/\Delta T$, we can calculate the parameter γ as

$$\gamma \approx -32k_B\left(\frac{\Delta\sigma_f}{\Delta T}\right)^{-1}. \qquad (6)$$

The values of U_0 and γ determined in this way are presented in the table. As can be seen from these data, the activation energy for the fracture of adhesion joints varies within 105–125 kJ/mol and the activation vol-

ume is $\gamma = 1.7–2.8$ nm^3, depending on the glue composition.

Deviations from the Zhurkov equation in the region of low temperatures were previously reported for a large number of polymers [15–22]. It was assumed that the discrepancy is related to a change in the mechanism of rupture of interatomic bonds, which are broken under the action of thermal fluctuations at high temperatures and as a result of tunneling transitions in the low-temperature range.

In order to take into account the role of tunneling transitions in the fracture kinetics, the temperature in Eq. (1) is replaced by the quantum function $F(\vartheta_D/T)$ [15–22], which yields

$$\sigma \approx \frac{U_0}{\gamma} - \frac{k_B F(\vartheta_D/T)}{\gamma} \ln\frac{\tau}{\tau_0}. \quad (7)$$

However, the quantum function is virtually independent of the temperature at $T < T_t$ and we can assume that $F(\vartheta_D/T) \approx$ const. Then, Eq. (7) can be rewritten as

$$\sigma_f \approx \frac{U_0}{\gamma} - 32\frac{k_B \text{const}}{\gamma}, \quad (8)$$

according to which the strength at low temperatures remains constant, in agreement with the experimental results for glue joints. Apparently, the fracture of these adhesion joints at low temperatures takes place with the participation of tunneling transitions.

Now, let us consider the region of temperatures above T_b. Previously [22], we demonstrated that the upper critical temperature approximately corresponds to the glass transition temperature of a polymer, $T_b \approx T_g$. As is known, polymers at $T > T_g$ exhibit a sharp increase in the pre-fracture deformation (elongation at break), so that the value of γ determined from fracture tests continuously decreases [23]. This is manifested by gradually decreasing slope of the temperature dependence of the polymer strength [23].

Thus, the strength of the adhesion of epoxy-rubber glues and steel exhibits a linear decrease with increasing temperature, as predicted by the Zhurkov equation, only in the temperature interval $T_t < T < T_b$. At $T < T_t$, the adhesion strength is independent of the temperature. At $T > T_b$, the slope of the temperature dependence of the adhesion strength decreases with increasing temperature. Deviations from the behavior described by the Zhurkov equation can be related to a change in the fracture mechanism at low temperatures and to variation of the parameter γ at elevated temperatures.

Acknowledgments. This study was supported by the Federal Targeted Program "Integration 2002" (project nos. B-0012 and I-0189).

REFERENCES

1. S. N. Zhurkov, Vestn. Akad. Nauk SSSR, No. 11, 78 (1957).
2. S. N. Zhurkov, J. Fract. Mech. **1**, 311 (1965).
3. V. R. Regel', A. I. Slutsker, and É. E. Tomashevskiĭ, Usp. Fiz. Nauk **106**, 193 (1972) [Sov. Phys. Usp. **15**, 593 (1972)].
4. S. N. Zhurkov, Vestn. Akad. Nauk SSSR, No. 3, 46 (1968).
5. V. R. Regel', A. L. Slutsker, and É. E. Tomashevskiĭ, *The Kinetic Nature of the Hardness of Solids* (Nauka, Moscow, 1974).
6. V. A. Petrov, A. Ya. Bashkarev, and V. I. Vettegren', *Physical Basis of Predicting the Working Life of Structural Materials* (Politekhnika, St. Petersburg, 1993).
7. A. S. Freĭdin, *Strength and Working Life of Cement Compounds* (Khimiya, Moscow, 1971).
8. A. D. Zimon, *Adhesion of Films and Coatings* (Khimiya, Moscow, 1977).
9. A. S. Freĭdin and Vu Ba Kiem, Vestn. Mashinostr. **48**, 49 (1968).
10. A. S. Freĭdin, P. P. Novokreshchenov, and V. N. Zigern-Korn, Plast. Massy **11**, 57 (1966).
11. A. T. Sanzharovskiĭ, M. S. Dyl'kov, and P. I. Zubov, Lakokras. Mater. Ikh Primenen., No. 6, 17 (1964).
12. A. A. Berlin and V. E. Basin, *Principles of Polymer Adhesion* (Khimiya, Moscow, 1969).
13. A. P. Petrova, *Gluing Materials: A Handbook* (KiR, Moscow, 2002).
14. G. V. Motovilin, *Dictionary-Handbook on Gluing* (Voen. Akad. Tyla Transporta Min. Oborony RF, St. Petersburg, 1996).
15. A. I. Slutsker and Kh. Aĭdarov, Vysokomol. Soedin., Ser. A **26**, 1823 (1984).
16. R. L. Salganik, A. I. Slutsker, and Kh. Aĭdarov, Dokl. Akad. Nauk SSSR **274**, 1362 (1984) [Sov. Phys. Dokl. **29**, 136 (1984)].
17. S. V. Bronnikov, V. I. Vettegren', and L. N. Korzhavin, Mekh. Polim. **5**, 920 (1983).
18. A. E. Gal', V. I. Vettegren', and K. E. Perepelkin, Vysokomol. Soedin., Ser. B **27**, 615 (1985).
19. S. V. Bronnikov, V. I. Vettegren', and L. N. Korzhavin, Vysokomol. Soedin., Ser. A **26**, 2483 (1984).
20. S. V. Bronnikov, V. I. Vettegren, and S. Y. Frenkel, Polym. Eng. Sci. **32**, 1204 (1992).
21. V. I. Vettegren', S. V. Bronnikov, and I. I. Ibragimov, Vysokomol. Soedin. **36**, 1294 (1994).
22. S. V. Bronnikov, V. I. Vettegren, and S. Y. Frenkel, Adv. Polym. Sci. **125**, 103 (1998).
23. V. A. Stepanov, N. N. Peschanskaya, and V. V. Shpeĭzman, *Strength and Relaxation Phenomena in Solids* (Nauka, Leningrad, 1984).

Translated by P. Pozdeev